2019

The Molecular Basis For Rapid Ca2+ Transport Across The Inner Mitochondrial Membrane

Riley J. Payne
University of Pennsylvania

The Molecular Basis For Rapid Ca2+ Transport Across The Inner Mitochondrial Membrane

Abstract

Ca2+ uptake by energized mitochondria regulates bioenergetics, apoptosis, and global Ca2+ signaling. Ca2+ entry into mitochondria is mediated by the Ca2+ uniporter-channel complex containing MCU, the Ca2+-selective pore, and associated regulatory proteins. The precise roles of these regulatory proteins and their relative stoichiometry in the complex have yet to be elucidated. MICU1 was proposed to be necessary for MCU activity whereas subsequent studies suggested a role for MICU1 and its paralog MICU2 in channel inhibition in the low-cytoplasmic Ca2+ ([Ca2+]c) regime, a mechanism referred to as "gatekeeping". EMRE is required for MCU channel function and coupling of MICU1/2-mediated gatekeeping, but its stoichiometry relative to MCU in the native complex is unclear. We measured MCU activity over a wide range of quantitatively controlled and recorded [Ca2+]c to identify the regulatory function of the MICU1 and 2 and introduced mutations into Ca2+-binding sites in each protein to determine the mechanism by which [Ca2+]c controls channel activity. We then addressed the functional consequences of manipulating the relative stoichiometry of EMRE and MCU by introducing tagged MCU and EMRE in MCU/EMRE double-knockout cells to directly compare their expression and created a series of MCU-EMRE concatemers with multiple concatenated MCU subunits fused to EMRE, allowing us to "fix" their stoichiometry. MICU1 alone can mediate gatekeeping as well as highly cooperative activation of MCU activity, whereas the fundamental role of MICU2 is to regulate the threshold and gain of MICU1-mediated inhibition and activation of MCU. Our results provide a unifying model for the roles of the MICU1/2 heterodimer in MCU-channel regulation and suggest an evolutionary role for MICU2 in spatially restricting Ca2+ uptake to mitochondria localized to nanodomains of high (>2 μM) [Ca2+]c. Furthermore, while incorporation of a single EMRE reconstitutes channel activity, additional EMRE subunits increase the [Ca2+]c-threshold required for relief of gatekeeping. Endogenous channels most likely contain two EMRE subunits which tether two MICU1/2-dimers to the complex. These findings have important implications for developing new therapies to target diseases arising from dysregulation of mitochondrial Ca2+-transport.

Degree Type

Dissertation

Degree Name

Doctor of Philosophy (PhD)

Graduate Group

Cell & Molecular Biology

First Advisor

James K. Foskett

Keywords

calcium transport, gatekeeping, ion channel, mitochondria, stoichiometry, uniporter

Subject Categories

Biochemistry | Cell Biology | Physiology

THE MOLECULAR BASIS FOR RAPID CA^{2+} TRANSPORT ACROSS THE INNER MITOCHONDRIAL MEMBRANE

Riley J. Payne

A DISSERTATION

in

Cell and Molecular Biology

Presented to the Faculties of the University of Pennsylvania

in

Partial Fulfillment of the Requirements for the

Degree of Doctor of Philosophy

2019

Supervisor of Dissertation

_____

J. Kevin Foskett, Ph.D.

Isaac Ott Professor and Chair of Physiology

Graduate Group Chairperson

_____

Daniel S. Kessler, Ph.D.

Associate Professor of Cell and Developmental Biology

Dissertation Committee

Roberto Dominguez, Ph.D. - William Maul Measey Presidential Professor of Physiology

Joseph Baur, Ph.D. - Associate Professor of Physiology

Marni Falk, MD - Executive Director, Mitochondrial Medicine Frontier Program

Associate Professor of Pediatrics

Benjamin L. Prosser, Ph.D. - Assistant Professor of Physiology

THE MOLECULAR BASIS FOR RAPID CA^{2+} TRANSPORT ACROSS THE INNER MITOCHONDRIAL MEMBRANE

DEDICATION

For Brenda, who has been my support system, advocate and advisor throughout this journey and my grandmother, Marion, who taught me the value of persistence and patience.

ACKNOWLEDGMENT

I thank Dr. Vamsi Mootha for providing the MCU KO, MICU1 KO, MICU2 KO and EMRE KO cell lines. This work was supported by T32 HL 7954-16 (RP) and NIH R37 GM056238 (JKF). Special thanks to Dr. Horia Vais and Emily Fernandez Garcia for providing the unpublished data discussed in Chapter 4.

ABSTRACT

THE MOLECULAR BASIS FOR RAPID CA^{2+} TRANSPORT ACROSS THE INNER MITOCHONDRIAL MEMBRANE

Riley J. Payne

Prof. J. Kevin Foskett, Ph.D.

Ca^{2+} uptake by energized mitochondria regulates bioenergetics, apoptosis, and global Ca^{2+} signaling. Ca^{2+} entry into mitochondria is mediated by the Ca^{2+} uniporter-channel complex containing MCU, the Ca^{2+}-selective pore, and associated regulatory proteins. The precise roles of these regulatory proteins and their relative stoichiometry in the complex have yet to be elucidated. MICU1 was proposed to be necessary for MCU activity whereas subsequent studies suggested a role for MICU1 and its paralog MICU2 in channel inhibition in the low-cytoplasmic Ca^{2+} ($[Ca^{2+}]_c$) regime, a mechanism referred to as "gatekeeping". EMRE is required for MCU channel function and coupling of MICU1/2-mediated gatekeeping, but its stoichiometry relative to MCU in the native complex is unclear. We measured MCU activity over a wide range of quantitatively controlled and recorded $[Ca^{2+}]_c$ to identify the regulatory function of the MICU1 and 2 and introduced mutations into Ca^{2+}-binding sites in each protein to determine the mechanism by which $[Ca^{2+}]_c$ controls channel activity. We then addressed the functional consequences of manipulating the relative stoichiometry of EMRE and MCU by introducing tagged MCU and EMRE in *MCU*/*EMRE* double-knockout cells to directly compare their expression and created a series of MCU-EMRE concatemers with multiple concatenated MCU subunits fused to EMRE, allowing us to "fix" their stoichiometry. MICU1 alone can mediate gatekeeping as well as highly cooperative activation of MCU activity, whereas the fundamental role of MICU2 is to regulate the threshold and gain of MICU1-mediated inhibition and activation of MCU. Our results provide a unifying model for the roles of the MICU1/2 heterodimer in MCU-channel regulation and suggest an evolutionary role for MICU2 in spatially restricting Ca^{2+} uptake to mitochondria localized to nanodomains of high (>2 μM) $[Ca^{2+}]_c$. Furthermore, while incorporation of a single EMRE reconstitutes channel activity, additional EMRE subunits increase the $[Ca^{2+}]_c$-threshold required for relief of gatekeeping. Endogenous channels most likely contain two EMRE subunits which tether two MICU1/2-dimers to the complex. These findings have important implications for developing new therapies to target diseases arising from dysregulation of mitochondrial Ca^{2+}-transport.

TABLE OF CONTENTS

LIST OF TABLES

LIST OF ILLUSTRATIONS

CHAPTER 1: Introduction to Mitochondrial Ca^{2+} Transport

The physiological importance of mitochondrial Ca^{2+} uptake

In the early 1960's, pioneers in the field of mitochondrial bioenergetics discovered that organs such as the heart and kidney have the capacity to take up large amounts of calcium (Ca^{2+}) (DeLuca and Engstrom, 1961)(Vasington and Murphy, 1962). Subsequent work revealed that Ca^{2+}-uptake served to stimulate mitochondrial respiration to a similar extent as ADP and free-phosphate (P_i), both of which are substrates for the production of ATP (Chance, 1965). In fact, such large quantities of Ca^{2+} were taken up by mitochondria that it was initially proposed that they represented the primary intracellular Ca^{2+} storage organelles in the cell. Later it was discovered that this role was actually a specialized function of the sarco/endoplasmic reticulum (ER) (Streb et al., 1983). However, studies in the 1990's led to a renewed interest in mitochondrial Ca^{2+}-signaling when it was discovered that agonist-induced mobilization of Ca^{2+} into the cytoplasm stimulated rapid, transient increase in matrix free-Ca^{2+} ($[Ca^{2+}]_m$) (Rizzuto et al., 1992). Today, it is well known that mitochondrial Ca^{2+}-uptake plays important roles in regulating cell metabolism, cell death and global Ca^{2+} signals by buffering cytoplasmic $[Ca^{2+}]$ ($[Ca^{2+}]_c$). The inner mitochondrial membrane (IMM) voltage ($\Delta\Psi_m$) generated by the respiratory chain provides a tremendous thermodynamic driving force for Ca^{2+} uptake from the cytoplasm into the matrix. Nevertheless, mitochondrial-matrix Ca^{2+} concentration ($[Ca^{2+}]_m$) must be tightly controlled to maintain a balance between optimal energy production and toxic effects, including IMM depolarization and activation of the permeability transition pore.

Regulation of TCA cycle enzymes by Ca^{2+} ions

Ca^{2+}-ions that enter the matrix regulate the activity of three mitochondrial dehydrogenases: pyruvate dehydrogenase (PDH), isocitrate dehydrogenase (IDH), and α-ketoglutarate dehydrogenase (αKGDH) (Denton, 2009). First, the dehydrogenase activity of PDH is dependent on the activity of two regulatory enzymes also found in the matrix, pyruvate

dehydrogenase kinase (PDK) and pyruvate dehydrogenase phosphatase (PDP) (Kolobova et al., 2001). Phosphorylation by PDK at multiple sites inactivates PDH, reducing the flux of pyruvate into mitochondria and subsequently inhibiting mitochondrial respiration. Opposing this process is PDP, whose activity increases the activity of PDH by de-phosphorylation. Importantly, the catalytic subunit of PDP isoform 1 (PDPC1) is allosterically activated by free-Ca^{2+} in the matrix, which in turn stimulates PDH activity, and facilitates transfer of electrons from Coenzyme A to oxidized nicotinamide adenine dinucleotide (NAD^+) to form reduced nicotinamide adenine dinucleotide (NADH) and allows entry of pyruvate into the TCA cycle in the form of Acetyl-CoA. Prior work has shown that maximal activation of PDH activity requires a $[Ca^{2+}]_m$ of ~2 µM. However, in the presence of > 10 µM pyruvate as a substrate, PDH flux was unaffected by changes in $[Ca^{2+}]_m$, indicating that under some physiological conditions this mode of regulation may be irrelevant (Wan et al., 1989).

In contrast to PDH, IDH and αKGDH are directly allosterically regulated by Ca^{2+}-ions in the matrix (Denton, 2009). Binding of Ca^{2+} increases the affinity of both enzymes for their respective substrates, thus increasing flux through the TCA cycle. This is particularly interesting considering the fact that IDH is the rate-limiting step in the TCA cycle (Stueland et al., 1988). Like PDH, both IDH and αKGDH also require NAD^+ as a co-factor, which is reduced to NADH to serve as an electron carrier and substrate for NADH:ubiquinone oxidoreductase, also known as respiratory Complex I. Some of the energy from oxidation of NADH by Complex I is used to pump 4 protons (H^+) (for each electron pair) out of the matrix into the intermembrane space, contributing to the large negative membrane potential ($\Delta\Psi_m$) as well as a pH gradient (ΔpH) across the IMM. Together, these gradients comprise the proton-motive force that drives protons through the F_1/F_0 ATP synthase to produce ATP from ADP and P_i in the matrix (Jonckheere et al., 2012).

Physiological effects of mitochondrial Ca^{2+} overload

Despite the fundamental role of Ca^{2+} in promoting mitochondrial bioenergetics, excessive uptake into the matrix can have profound negative consequences for cell physiology. Transient or constitutive elevations in $[Ca^{2+}]_m$ can induce the formation of the mitochondrial permeability transition pore (mPTP) by interacting with the regulatory protein Cyclophilin D (Basso et al., 2005), allowing non-specific ion and solute transport across both the IMM and outer mitochondrial membrane (OMM). This in turn leads to mitochondrial depolarization and subsequent failure in ATP production (Hajnóczky et al., 2009). Referred to in the literature as "mitochondrial Ca^{2+}-overload", this toxic elevation in $[Ca^{2+}]_m$ can also promote the generation of reactive oxygen species (ROS) and free-fatty acids which further potentiate mPTP formation (Scorrano et al., 2001)(Starkov et al., 2004).

Mitochondrial depolarization has been linked to the initiation of mitophagy, the selective elimination of damaged mitochondria through lysosome-dependent degradation (Lemasters, 2014)(Galluzzi et al., 2017). Mitophagy occurs through a series of molecular mechanisms, the first of which is the PINK1/Parkin pathway (Yoo and Jung, 2018). PTEN-induced putative kinase 1 (PINK1) is normally targeted to the mitochondrial matrix through $\Delta\Psi_m$-dependent import processes and eventually degraded, but upon depolarization is translocated to the OMM where it accumulates on the surface of mitochondria (Matsuda et al., 2010). Autophosphorylation activates PINK1, which phosphorylates ubiquitin and leads to the recruitment of Parkin, an E3-ubiquitin ligase. On the OMM, Parkin is directly activated by PINK1 and polyubiquitinates several mitochondrial protein substrates (Nguyen et al., 2016). Interestingly, the K63-linked polyubiquitin chains on these targets have been shown to be involved in non-proteolytic pathways, in contrast to K48-linked chains that are known to target proteins for proteasomal degradation (Li and Ye, 2008). In mitophagy, K63-linked, polyubiquitinated substrates on the OMM recruit various microtubule-associated protein 1A/1B-light chain 3 (LC3) adapter proteins, the most important of these being optineurin (OPTN) (Moore and Holzbaur, 2016). These adapters then are recognized

by LC3 and target the damaged mitochondria to the autophagosome for degradation (Lazarou et al., 2015).

In addition to promoting $\Delta\Psi_m$ depolarization, mPTP opening plays a fundamental role in initiating apoptosis, a specific type of “controlled” cell death that occurs through two distinct pathways: the extrinsic pathway, which is induced by extracellular signal molecules acting through specific cell surface receptors, and the intrinsic pathway, which is initiated by the release of mitochondrial proteins into the cytoplasm through opening of the mPTP (D’Arcy, 2019). While a number of mitochondrial proteins that exit mitochondria through the mPTP, including Smac/Diablo and HtrA2/Omi, have been implicated in promoting apoptosis, the most well studied of these is cytochrome C (CytC) (Cain et al., 2002). Upon its release into the cytoplasm CytC binds to the monomeric form of apoptotic protease activating factor 1 (APAF1), leading to conformational changes that promote its oligomerization to form a complex known as the apoptosome (Acehan et al., 2002). Once assembled, the apoptosome directly activates procaspase 9, which itself activates procaspase 3 and commits the cell to apoptotic death.

Even under circumstances when enhanced mitochondrial Ca^{2+}-uptake is insufficient to induce mPTP formation, constitutive elevations in $[Ca^{2+}]_m$ can lead to a cellular energy deficiency. Bhosale et al., (2017) have proposed that this is through a “futile cycling” of Ca^{2+} ions across the IMM, in which the energy (in the form of adenosine triphosphate (ATP)) required to sustain mitochondrial Ca^{2+}-efflux mechanisms, and thus Ca^{2+} homeostasis, exceeds the Ca^{2+}-induced increase in ATP production.

Molecular identity of the uniporter: the primary pathway for Ca^{2+} across the IMM

The primary mechanism for rapid Ca^{2+} entry into the mitochondria is the mitochondrial calcium uniporter (MCU) (Gunter and Gunter, 1994), which was named for its ability to mediate unidirectional Ca^{2+}-transport from the cytoplasm into the matrix and characterized by its sensitivity to ruthenium red (RuR). The uniporter was later shown by mitoplast patch-clamp electrophysiology to be a highly selective Ca^{2+} channel with high carrying-capacity (Kirichok et al.,

2004). As such, mechanisms must be present to ensure that the rate of Ca^{2+} influx does not exceed extrusion capacity and cause Ca^{2+} overload. Previously, it was suggested that an intrinsically-low Ca^{2+}affinity of the channel prevented mitochondrial Ca^{2+} uptake unless the channel was exposed to high cytoplasmic [Ca^{2+}] ($[Ca^{2+}]_c$) that exist in nanodomains associated with activated Ca^{2+} channels in the plasma membrane or intracellular organelles, especially the endoplasmic reticulum (ER), the major Ca^{2+} storage organelle in cells. Nevertheless, the uniporter channel was shown to have a very-high Ca^{2+} affinity, $\leq$ 2 nM (Kirichok et al., 2004), suggesting that whereas mitochondrial Ca^{2+} uptake required high $[Ca^{2+}]_c$, it was unlikely to be due to an intrinsic low-Ca^{2+} affinity, but rather to regulatory mechanisms that keep the channel closed until $[Ca^{2+}]_c$ reaches sufficiently high levels.

MCU: the pore-forming subunit of the uniporter

In 2010 the first human gene involved in rapid mitochondrial Ca^{2+}-uptake (*CBARA1*), was discovered by Perocchi et al., and subsequently renamed mitochondrial calcium uptake Protein 1 (MICU1), ushering in the molecular era of the uniporter (Figure 1.1). One year later, two groups identified the gene *CCDC109A*, which encodes the pore-forming subunit of the uniporter, a two-transmembrane (TM1 & 2) protein also named MCU (Baughman et al., 2011)(De Stefani et al., 2011). The latter group later identified the related protein MCUb (encoded by the gene *CCDC109B*), which has been described as a dominant negative subunit that assembles with MCU and inhibits channel activity (Raffaello et al., 2013). Although it was originally believed that human MCU assembled as a pentamer (Oxenoid et al., 2016), recent cryo-EM structures of full-length fungal and metazoan

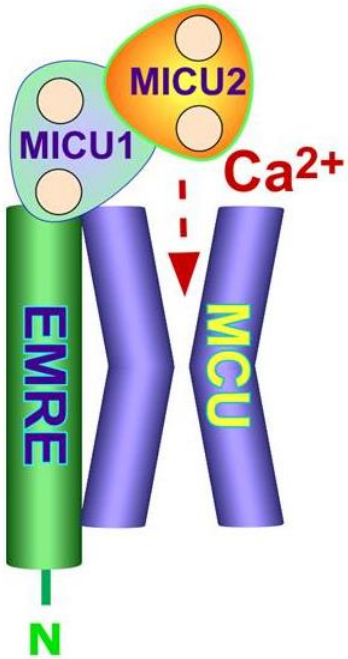

Figure 1.1. The protein subunits MCU, EMRE and MICU1/2 comprise the core of the functional uniporter complex

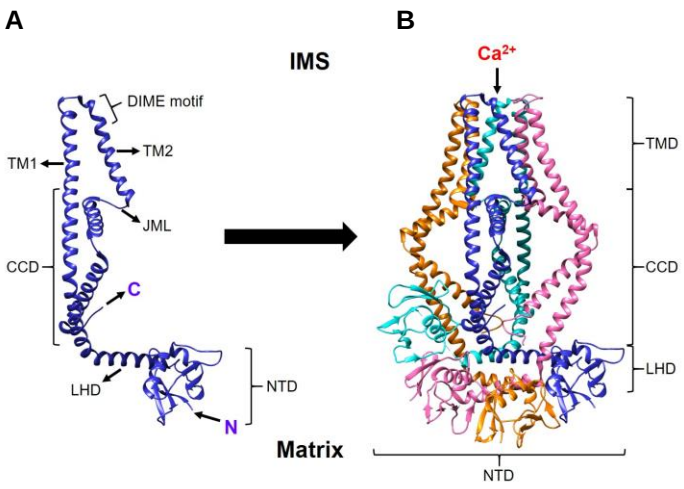

Figure 1.2. Molecular architecture of human MCU (adapted from Wang et al., 2019)

(**A**) MCU monomer with transmembrane domains (TM1 and TM2), DIME motif, juxtamembrane loop (JML) region, coiled-coil domain (CCD), linker-helix domain (LHD), and N-terminal domain (NTD) specified. (**B**) MCU tetramer with TMDs, CCDs, LHDs, and NTDs specified. Colors represent individual MCU monomers. The TMDs and CCDs assemble with 4-fold symmetry that is not preserved in the NTDs.

MCU channels revealed that the pore assembles as a homotetramer, in which the transmembrane domains (TMDs) adopt a 4-fold symmetry that stabilizes the selectivity filter (Baradaran et al., 2018)(Yoo et al., 2018)(Wang et al., 2019)(Fan et al., 2018)(Nguyen et al., 2018). In addition to the TMDs, human MCU contains a coiled-coil domain (CCD) that is linked to TM2 by a juxtamembrane loop (JML) region, and an N-terminal domain (NTD) connected to the CCD by a linker-helix domain (LHD), all of which are localized to the matrix (Wang et al., 2019). The conserved aspartate-isoleucine-methionine-glutamate (DIME) motif in the IMS between TM1 and TM2 contains two negatively charged residues (D261 and E264) that coordinate Ca^{2+} ions in the assembled tetramer (Figure 1.3) (Yoo et al., 2018)(Baradaran et al., 2018)(Wang et al., 2019), and mutation of either residue to alanine abolishes channel activity (Baughman et al., 2011)(De

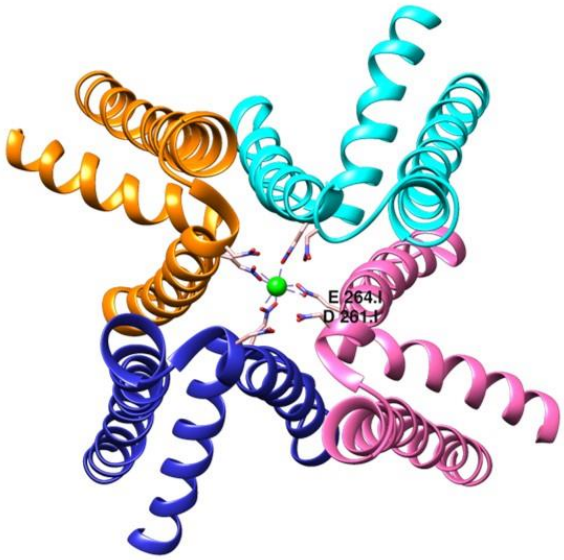

Figure 1.3. Ca^{2+} coordination in the selectivity filter of the MCU pore (adapted from Wang et al., 2019)

Top view of MCU tetramer showing the coordination of a Ca^{2+} ion (green) by residues D261 and E264 (atoms rendered by charge: red = (-1), blue = (+1)).

Stefani et al., 2011). Whole-mitoplast patch clamp experiments have shown that MCU can conduct monovalent (e.g. Na^+) ions *only* in the absence of external Ca^{2+} (Kirichok et al., 2004)(Fieni et al., 2012)(Vais et al., 2016), a phenomenon that is attributed to the high affinity of the D261 and E264 binding site for Ca^{2+} ions ($K_D \leq 2nM$) and the channel with high Ca^{2+} selectivity ($Ca^{2+} \cong Sr^{2+} >> Mn^{2+} \cong Ba^{2+}$).

Considering the pleiotropic nature of Ca^{2+} uptake in regulating mitochondrial physiology, it is surprising that mice with global ablation of *Mcu* ($MCU^{-/-}$) are essentially healthy and show no overt developmental or morphological defects (Pan et al., 2013)(Holmström et al., 2015). While mitochondria from these mice exhibit no uptake of Ca^{2+} in response to elevations in $[Ca^{2+}]_c$, measures of basal metabolism such as oxygen consumption rate (OCR) are largely unaffected, with only a small reduction in spare respiratory capacity and PDH activity relative to $MCU^{(+/+)}$ littermates. Likewise, increases in $[Ca^{2+}]_c$ fail to induce mPTP opening in $MCU^{-/-}$ mice, but this does not protect cells from ischemia-reperfusion injury or pharmacological agents that induce apoptosis. The only phenotypes reported were in skeletal muscle, characterized by an "impairment in their ability to perform strenuous work" (Pan et al., 2013), and cortical neurons, which displayed elevated levels of glycolysis in response energetic stress (Nichols et al., 2017). Interestingly, while whole-body $MCU^{-/-}$ mice exhibit no apparent cardiac phenotype (Holmström et al., 2015), cardiomyocyte-specific deletion of *Mcu* in adult mice has been shown to protect against Ca^{2+}-induced mPTP opening and acute ischemia reperfusion injury (Luongo et al., 2015)(Kwong et al., 2015). Moreover, mitochondria from these mice have reduced basal ATP production and a delayed increase in OCR upon stimulation with the β-adrenergic receptor agonist isoproterenol. These discrepancies are attributed to genetic compensation that allows normal mitochondrial development, which is further evidenced by the finding that $MCU^{-/-}$ mice are only viable when maintained on a mixed genetic background, in this case the outbred (CD1) strain. Global ablation of *Mcu* in inbred C57BL/6 mice is embryonic lethal, with death occurring between E11.5 and E13.5 (Murphy et al., 2014).

MICU1, 2 and 3: Accessory proteins that regulate uniporter activity

While MCU protein constitutes the pore-forming subunit of the channel, interactions with several auxiliary proteins are required to regulate its activity, including MICU1 (Perocchi et al., 2010), and its paralogs MICU2 and MICU3 (Plovanich et al., 2013). In humans, MICU1 and MICU2 are widely expressed, whereas MICU3 appears to be largely restricted to the central nervous system (Plovanich et al., 2013)(Patron et al., 2019). Although their cellular localization is still the subject of debate (Hoffman et al., 2013), MICU proteins are generally thought to reside in the IMS and associate with the outer leaflet of the IMM (Perocchi et al., 2010)(Csordás et al., 2013)(Patron et al., 2014). In the Apo (Ca^{2+}-free) state, MICU1 forms homodimers (Figure 1.4) as well as heterodimers with MICU2 (Patron et al., 2014)(Petrungaro et al., 2015) and MICU3 (Patron et al., 2019). However, once Ca^{2+} is bound, significant structural rearrangements occur that disrupt the dimer and are presumably coupled to modulation of channel activity. Two EF-hand domains in each MICU protein were identified by sequence homology (Perocchi et al., 2010)(Plovanich et al., 2013) and confirmed to bind Ca^{2+} ions in structures of MICU1 (Wang et al., 2014), MICU2 (Kamer et al., 2019)(Wu et al., 2019)(Xing et al., 2019) and MICU3 (Xing et al., 2019). Ion transport across the OMM is generally passive, while transport across the IMM is

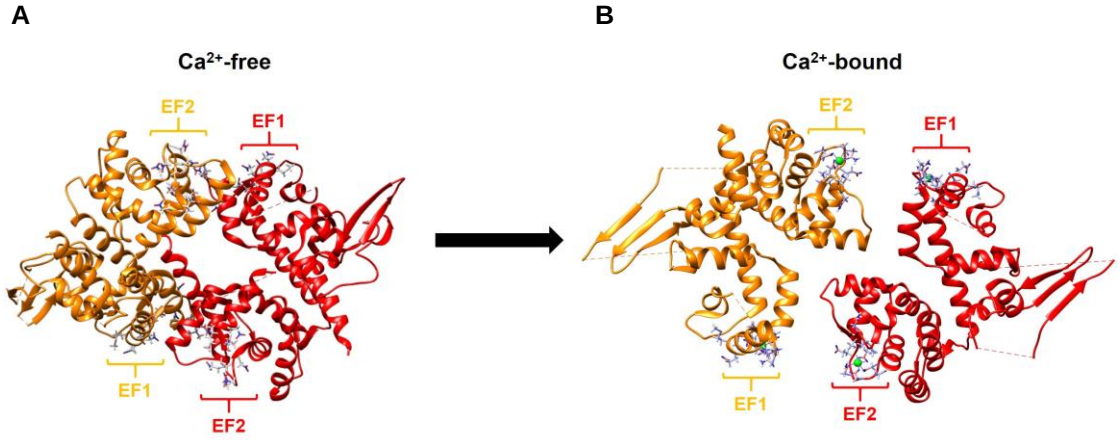

Figure 1.4. Crystal structure of the MICU1 homodimer in the Ca^{2+}-free and Ca^{2+}-bound states (adapted from Wang et al., 2014)

(**A**) MICU1 monomers (red and orange) dimerize when the EF hand domains (EF1 and EF2 – atoms rendered by charge: red = (-1), blue = (+1)) are in their Apo (Ca^{2+}-free) states. (**B**) Binding of Ca^{2+} ions (green) to EF1 and EF2 leads to conformational changes that disrupt the MICU1 dimer.

tightly regulated by channels and transporters (O'Rourke, 2007). As such, Ca^{2+}-binding EF-hand domains in MICU1, 2, and 3 have been proposed to sense $[Ca^{2+}]_c$ and modulate channel activity. It has been suggested that MICU1 associates with the channel complex in part by a direct interaction with MCU by an electrostatic mechanism that involves positively-charged residues in MICU1 and negatively-charged residues associated with the pore domain of MCU (Paillard et al., 2018)(Phillips et al., 2019). MICU2 lacks analogous basic residues, in agreement with previous findings that MICU2 requires dimerization with MICU1 for its association with the complex. The number of MICU1/2 dimers that associate with one MCU channel is unknown.

The importance of understanding regulation of MCU-channel activity by MICU proteins is underscored by human loss-of-function mutations in *MICU1* that result in apparent mitochondrial-Ca^{2+} overload and cause early-onset muscle weakness and CNS defects (Logan et al., 2013)(Lewis-Smith et al., 2016). Similar pathology and effects on mitochondrial Ca^{2+} observed in surviving MICU1 knockout mice suggested that constitutive MCU-activity *in vivo* caused disease (Liu et al., 2016), but the etiology of pathogenesis is still the subject of debate (see Chapter 4). Likewise, human loss-of-function mutations in MICU2 have been linked to severe neurological defects in development (Shamseldin et al., 2017), and genetic knockdown of MICU3 expression in primary cortical neurons leads to dysregulation of neuronal function (Patron et al., 2019). The specific roles of MICU1 and 2 in MCU channel regulation are addressed in Chapter 2.

EMRE: A small transmembrane subunit with a dual role in MCU regulation

The small (~100 a.a.) transmembrane protein essential MCU regulator (EMRE) is aptly named; it is required for both uniporter function and coupling of MICU1/2-mediated gatekeeping (Sancak et al., 2013)(Kovács-Bogdán et al., 2014)(Yamamoto et al., 2016)(Vais et al., 2016)(Tsai et al., 2016)(Figure 1.5A). A conserved polyacidic C-terminus of EMRE faces into the IMS where it interacts with a polybasic region in the N-terminus of MICU1 (but not MICU2) (Sancak et al., 2013)(Hoffman et al., 2013)(Yamamoto et al., 2016)(Tsai et al., 2016)(Vais et al., 2016). This

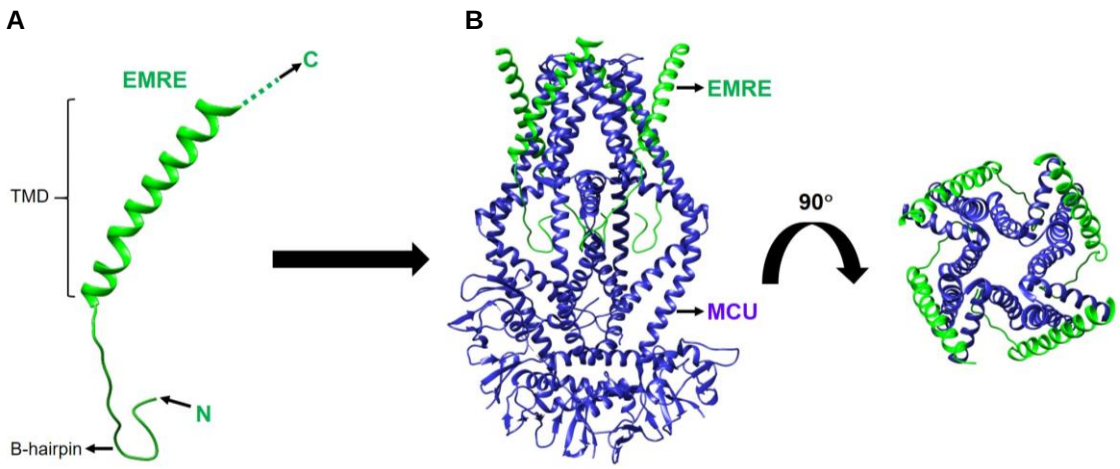

Figure 1.5. Cryo-EM structure of human EMRE in complex with MCU (adapted from Wang et al., 2019)

(**A**) EMRE is a single-TM protein with an N-terminal β-hairpin motif in the matrix and the C-terminus in the IMS. The polyacidic region in the C-terminus was not resolved (dashed line). (**B**) Four EMRE proteins associate with the assembled MCU tetramer.

interaction is required for the gatekeeping function of MICU1/2 since deletion of the polyacidic region or neutralization of its charge abolishes normal gatekeeping, causing mitochondrial Ca^{2+} overload (Tsai et al., 2016)(Vais et al., 2016). In addition, binding of EMRE to MCU is necessary for channel activity. In the absence of EMRE, MCU is expressed normally but it lacks function.

The association of EMRE with the channel complex is mediated in part by transmembrane interactions with MCU (Tsai et al., 2016). A recent cryo-electron microscopy structure of human MCU in complex with EMRE (Wang et al., 2019) revealed a 4 EMRE:1 channel stoichiometry (Figure 1.5 B), with hydrophobic interactions between the transmembrane domain (TMD) of EMRE and TM1 in MCU (Figure 1.6A). Two additional interactions were also observed: one between the N-terminal end of the EMRE TMD and TM2 (Figure 1.6A), and the second between the N-terminal β-hairpin of EMRE and the CCD domain of an adjacent second MCU subunit (Figure 1.6B), the latter proposed to enable gating of the channel. This structure revealed an asymmetric distribution of NTDs among subunits, a structure quite dissimilar from a dimer-of-NTD-dimers observed in the fungal MCU channels (Baradaran et al., 2018)(Yoo et al., 2018)(Wang et al., 2019)(Lee et al., 2016). In addition, dimerization between the NTDs of two assembled MCU tetramers was observed (Figure 1.7), suggesting that metazoan MCU channels may form dimers *in situ*. It is unclear, however, whether this dimerization of MCU channels is

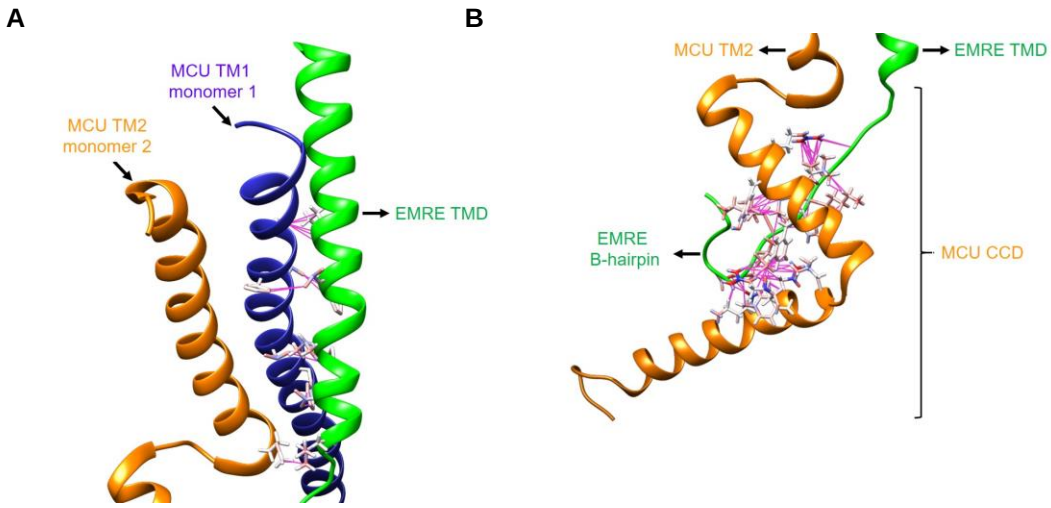

Figure 1.6. Interactions between MCU and EMRE in the assembled channel complex (adapted from Wang et al., 2019)

(**A**) The TMD of EMRE forms multiple contacts with TM1 of one MCU subunit (blue) and TM2 of an adjacent MCU subunit (orange) to stabilize its association with the channel (atoms rendered by charge: red = (-1), blue = (+1); pink lines show atomic contacts between MCU and EMRE). (**B**) The β-hairpin motif in the N-terminus of EMRE are proposed to mediate channel gating my affecting conformational changes in the CCD domain of MCU.

related to the presence of EMRE since a high-resolution structure of a metazoan MCU in the absence of EMRE has not been determined. The relative stoichiometry of MCU and EMRE in the assembled uniporter complex *in vivo* and the consequences of altering this stoichiometry on channel activity and regulation are addressed in Chapter 3.

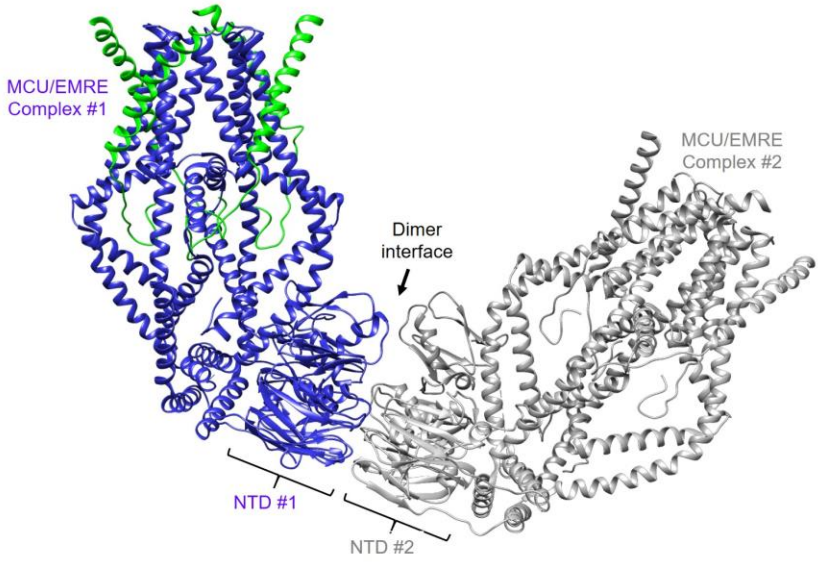

Figure 1.7. The human MCU-EMRE complex forms a dimer (adapted from Wang et al., 2019).

MCUR1: An assembly factor that regulates uniporter activity

First identified in 2012 by Mallilankaraman et al., mitochondrial calcium uniporter regulator 1 (MCUR1) is a protein integral to the IMM that was shown to be required for MCU function. ShRNA-mediated knockdown of MCUR1 (MCUR1 KD) abolished mitochondrial Ca^{2+} uptake and decreased oxidative phosphorylation in HEK-293T and HeLa cells, with no apparent effect on $\Delta\Psi_m$ or MCU localization. Subsequent studies in human immortalized fibroblasts conflicted with these findings, attributing a lack of Ca^{2+} uptake and impaired respiration to a reduction in $\Delta\Psi_m$ caused by defective cytochrome c oxidase (COX) assembly (Paupe et al., 2015). Nevertheless, reduced MCU-mediated Ca^{2+} currents in mitoplast patch-clamp experiments from MCUR1 KD (HEK-293T) cells provided further evidence for direct regulation of channel activity (Vais et al., 2015). Furthering the debate, Tomar et al. (2016) showed that genetic ablation of MCUR1 in HEK-293T cells disrupted proper formation of the channel complex, serving as an assembly factor through interactions with both MCU and EMRE. To date, the precise role of MCUR1 in regulating mitochondrial Ca^{2+} uptake and bioenergetics remains unclear.

Other mechanisms for Ca^{2+} transport in mitochondria

In addition to the uniporter, several alternative pathways for Ca^{2+} transport across the IMM have been described. First, the “rapid mode of uptake” (RaM) has been described as a mechanism to rapidly take up Ca^{2+} from the cytoplasm in response to transient increases in $[Ca^{2+}]_c$ with characteristics distinct from the uniporter; the RaM appears to function at low (~200 nM) $[Ca^{2+}]_c$, is capable of sustaining only small Ca^{2+} fluxes, and is less sensitive to inhibition by RuR by an order of magnitude (Sparagna et al., 1995). Single-channel recordings of inward Ca^{2+} currents in mitoplasts isolated from HeLa cells revealed the presence of two distinct conductances: “intermediate mitochondrial Ca^{2+} currents” (i-MCC), and ”extra-large mitochondrial Ca^{2+} currents” (xl-MCC) (Bondarenko et al., 2013). Knockdown of MCU in these cells lead to a decrease in i-MCC and increase in xl-MCC, leading to the conclusion that i-MCC was mediated by the uniporter and xl-MCC by a second, unidentified molecular mechanism (Bondarenko et al.,

2014). However, the lack of genetic evidence for the existence of the RaM as a distinct molecular entity and technical concerns regarding the methods used in these studies have led many to hypothesize that both modes of Ca^{2+} uptake are mediated by the MCU complex. Nevertheless, it is also possible that the RaM is attributable to other Ca^{2+} channels in the IMM such as mitochondrial ryanodine receptors, which are also inhibited by RuR (Ryu et al., 2010).

The primary efflux pathway for Ca^{2+} that enters the matrix through MCU is the mitochondrial Na^+/Ca^{2+} exchanger (NCLX), which mediates Na^+-driven antiport of Ca^{2+} ions across the IMM (Palty et al., 2010). NCLX is distinct from the plasma membrane Na^+/Ca^{2+} exchanger (NCX) in its ability to transport Li^+ ions in the absence of Na^+. Genetic knockdown of NCLX reduces mitochondrial Ca^{2+} efflux in cells (Palty et al., 2010)(Luongo et al., 2017), and conditional, cardiomyocyte-specific deletion of *Slc8b1* (the gene encoding NCLX) in adult mice leads to sudden death from severe myocardial dysfunction (Luongo et al., 2017), a phenotype attributed to $[Ca^{2+}]_m$ driven ROS generation and subsequent necrotic cell death. Additionally, pharmacological inhibition of NCLX activity by the small molecule CGP37157 (Cox et al., 1993), has been shown to be protective in neuronal models of excitotoxic injury (Ruiz et al., 2014). The role of NCLX in extrusion of Ca^{2+} from the matrix also demonstrates its fundamental importance in balancing Ca^{2+} influx through MCU to prevent matrix Ca^{2+} overload (De Marchi et al., 2014). Interestingly, when mitochondria are depolarized and $[Ca^{2+}]_m$ is low, NCLX has been proposed to function in reverse, mediating a coupled influx of cytoplasmic Ca^{2+} and efflux of Na^+ ions from the matrix (Samanta et al., 2018). This is compelling considering the normal basal $[Ca^{2+}]_m$ observed in $MCU^{-/-}$ mice, suggesting that NCLX may be responsible for supplying enough influx of Ca^{2+} into the matrix under resting conditions to sustain respiration in the absence MCU. However, it is unclear whether the antiport activity of NCLX is electroneutral (i.e. 1 Ca^{2+} for 2 Na^+) or, like its counterpart in the plasma membrane, electrogenic (i.e. 1 Ca^{2+} for 3 Na^+) (Boyman et al., 2013).

The gene encoding leucine zipper, EF-hand containing transmembrane protein 1 (*LETM1*) was first identified as a homolog of the *YOL027* gene in yeast, both of which encode proteins with a single predicted transmembrane domain that localize to mitochondria (Nowikovsky

et al., 2004). Deletion of *YOL027* leads to mitochondrial swelling, an increase in matrix [K^+], and reduced $\Delta\Psi_m$. These phenotypes are rescued by expression of human *LETM1*, suggesting a conserved function between the yeast and human homologs. Moreover, loss of function mutations in *LETM1* have been associated with Wolf-Hirschhorn syndrome in humans, a disease characterized by seizures and other related neuromuscular pathologies. Later worked showed that the human LETM1 protein is integral to the IMM and its downregulation causes fragmentation of the mitochondrial network in HeLa cells (Dimmer et al., 2008). Treatment with nigericin, a pharmacological catalyst of K^+/H^+ exchange, restores normal mitochondrial morphology, leading to the conclusion that LETM1 functions as a K^+/H^+ antiporter. However, work from other groups identified *LETM1* as a mitochondrial Ca^{2+}/H^+ exchanger in a genome-wide RNAi screen (Jiang et al., 2009) that plays a role in mitochondria Ca^{2+} transport (Jiang et al., 2009)(Waldeck-Weiermair et al., 2011)(Waldeck-Weiermair et al., 2011) and influences mitochondrial bioenergetics and cell proliferation (Doonan et al., 2014). Functional reconstitution of LETM1 in liposomes confirmed that it is necessary and sufficient to mediate electroneutral antiport of Ca^{2+} and H^+ (Jiang et al., 2009)(Tsai et al., 2014) independently of K^+ (Tsai et al., 2014). Interestingly, these studies also revealed that LETM1 activity is abolished by the known MCU inhibitor RuR (and its derivatives), and partially reduced by the NCLX inhibitor CGP37157. Moreover, recent studies have shown that, unlike NCLX, LETM1 does not mediate Ca^{2+} efflux from the mitochondria (De Marchi et al., 2014). Nevertheless, stable genetic knockdown of LETM1 in HeLa cells impedes both K^+/H^+, Na^+/H^+, and NCLX-mediated Na^+/Ca^{2+} exchange across the IMM (Austin et al., 2017), suggesting a fundamental role in mitochondrial ion homeostasis.

CHAPTER 2: Regulation of MCU Channel Activity by MICU1 and 2

The roles of MICU proteins in MCU regulation are controversial. MICU1 was originally proposed to be necessary for MCU-channel activity (Perocchi et al., 2010). Subsequent studies suggested that it instead plays a critical role in inhibiting MCU activity in the low-$[Ca^{2+}]_c$ regime, a mechanism referred to as "gatekeeping", that imposed a $[Ca^{2+}]_c$ threshold for channel activation at ~1-3 μM (Mallilankaraman et al., 2012b)(Csordás et al., 2013)(Patron et al., 2014)(Bhosale et al., 2015).

Other studies suggested that MICU1 is necessary to promote mitochondrial Ca^{2+} uptake in response to $[Ca^{2+}]_c$ elevations (Perocchi et al., 2010)(Csordás et al., 2013)(Patron et al., 2014)(Kamer and Mootha, 2014)(Antony et al., 2016), with some suggesting that it plays dual roles in gatekeeping and cooperative channel-activation (Csordás et al., 2013)(Antony et al., 2016). It is debated whether the EF-hand domains play a role in MICU1-mediated channel inhibition in low $[Ca^{2+}]_c$ (Mallilankaraman et al., 2012b)(Hoffman et al., 2013)(Kamer and Mootha, 2014). Early studies of MICU1 were complicated by the discovery that its knockdown affected expression of MICU2 (Plovanich et al., 2013)(Patron et al., 2014)(Kamer and Mootha, 2014). Under physiological conditions, MICU1 forms an obligate heterodimer with MICU2, stabilizing MICU2 expression (Patron et al., 2014)(Petrungaro et al., 2015). On the other hand, overexpression of MICU1, or knockdown of MICU2, generates MICU1 homodimers (Patron et al., 2014)(Petrungaro et al., 2015). Conversely, MICU2 does not form homodimers in cells, nor can it associate with MCU in the absence of MICU1 (Patron et al., 2014)(Kamer and Mootha, 2014). It has been suggested that loss of gatekeeping in MICU1 knock-down cells is due to loss of MICU2 (Patron et al., 2014). In this model, MICU2 is the "true gatekeeper", inhibiting the channel in its Ca^{2+}-free form, whereas cooperative channel activation requires Ca^{2+} binding to MICU1, as well as to MICU2, to relieve channel inhibition. Alternatively, it has been suggested that both MICU1 and MICU2 play roles in gatekeeping, with MICU2 having no role in channel activation (Matesanz-Isabel et al., 2016). Finally, it has been suggested that both MICU1 and MICU2

contribute to setting the threshold for MCU activation (Kamer and Mootha, 2014). The functions of both proteins are controversial in part because overexpression strategies have been used with channel-component stoichiometries not well known, and because MCU-specific Ca^{2+}-uptake rates were not rigorously quantitated over a wide range of quantitatively-controlled and recorded $[Ca^{2+}]_c$.

We employed cells with MICU1 or MICU2 genetically deleted to address the molecular mechanisms by which MICU1 and MICU2 regulate MCU function, particularly in the previously uncharacterized $[Ca^{2+}]_c$ regime below 500 nM. Our results suggest that MICU1 alone can mediate gatekeeping as well as highly cooperative activation of MCU channel activity, whereas the fundamental role of MICU2 is to regulate the threshold and gain of MICU1-mediated inhibition and activation of MCU. Our results provide a unifying model for the role of the MICU1/2 heterodimer in MCU channel regulation and suggest an evolutionary role for MICU2 in spatially restricting Ca^{2+} crosstalk between single $InsP_3R$ and MCU channels.

Materials and methods:

Cell lines and cDNA expression constructs

All HEK-293T cell lines were grown in DMEM containing 10% fetal bovine serum (FBS) and 1x anti-biotic/anti-mycotic (complete medium) at 37˚C and 5% CO_2. MCU knockout (KO), MICU1 KO and MICU2 KO HEK-293T cells were a generous gift from Dr. Vamsi Mootha. Plasmids of full-length Flag-tagged MICU1 and MICU2 cDNAs in pCMV6-A-BSD vectors were obtained from Origene. Plasmids of mito-CAR-GECO1 cDNA in pCDNA3.1 vector; and MCU-V5-His cDNA in pDEST40 vector were purchased from Addgene. Plasmids of MICU1ΔEF1-Flag, MICU1ΔEF2-Flag and MICU1ΔEF1/2-Flag cDNA in pCMV6-A-BSD vector, together with MICU2ΔEF1-Flag, MICU2ΔEF2-Flag, MICU1ΔEF1/2-Flag and untagged MICU2 cDNA in pCMV6-A-Puro vector were generated using a PCR-based cloning strategy (see Appendix A). MICU1-rescue, [MICU1 KO + MICU1ΔEF1 + MICU2], [MICU1 KO + MICU1ΔEF2 + MICU2], and [MICU1 KO + MICU1ΔEF1/2 + MICU2] cell lines were created by stable transfection using Transit LT1 (Mirus) as per manufacturer's protocol. Transfected cells were maintained in complete medium with 5 µg/mL Blasticidin and 2 µg/mL Puromycin until stable expression of each plasmid was achieved. [MICU2 KO + MICU2-Flag] (rescue), [MICU2 KO + MICU2ΔEF1-Flag], [MICU2 KO + MICU2ΔEF2-Flag] and [MICU2 KO + MICU2ΔEF1/2-Flag] cells were created by stable transfection and maintained in complete medium with 5 µg/mL Blasticidin. Clones were isolated by limiting dilution for each condition and maintained in complete medium with antibiotics. Expression levels of each protein were evaluated by Western blot, and clones with uniform cell expression of MICU1 and MICU2 as assessed by immunofluorescence microscopy were used for experiments.

Simultaneous determination of mitochondrial Ca^{2+} uptake and $\Delta\Psi_m$ in permeabilized cells

Simultaneous measurement of mitochondrial Ca^{2+} uptake and IMM potential ($\Delta\Psi_m$) in permeabilized HEK-293T cells was performed as described (Mallilankaraman et al., 2012a), with

fluorescence measurements calibrated to represent bath [Ca^{2+}] ($[Ca^{2+}]_c$). Cells were grown in 10 cm tissue-culture coated dishes for 48 hr prior to each experiment. 6-8×10^6 cells were trypsinized, counted, and washed in a Ca^{2+}-free extracellular-like medium, centrifuged, suspended in 1.5 mL of intracellular-like medium (ICM - in mM: 120 KCl, 10 NaCl, 1 KH_2PO_4, 20 HEPES, and 5 succinate [pH 7.2]) that had been treated with BT Chelex® 100 resin (Bio-Rad, 143-2832) prior to use to attain an initial free [Ca^{2+}] of ~20 nM, and transferred to a cuvette. The cuvette was placed in a temperature-controlled (37°C) experimental compartment of a multi-wavelength-excitation dual wavelength-emission high-speed spectrofluorometer (Delta RAM, Photon Technology International). Membrane-impermeable Fura-2 K^+ salt (K_D = 140 nM) or Fura-FF K^+ salt (K_D = 5.5 µM) (final concentration 1 µM) and JC-1 (final concentration 800 nM) or Tetramethylrhodamine, Ethyl Ester, Perchlorate (TMRE - final concentration 1 µM) were added at 25 sec to measure $[Ca^{2+}]_c$ and $\Delta\Psi_m$ concurrently. Fluorescence at 490-nm excitation/535-nm emission for the monomer and 570-nm excitation/595-nm emission for the J-aggregate of JC1 or 560-nm excitation/595-nm emission for TMRE, along with 340 nm excitation/535 nm emission and 380 nm excitation/535 nm emission for the Ca^{2+}-bound and Ca^{2+}-free Fura-2/Fura-FF species, respectively was measured at 2-5 Hz. 40 µg/mL digitonin was added at 50 sec to permeabilize cells and allow the cytoplasm to equilibrate with the bath solution such that the JC-1 fluorescence ratio (570 nm/490 nm) or TMRE fluorescence reports the relative $\Delta\Psi_m$. Fura-2/Fura-FF fluorescence under these conditions is related to the cytoplasmic [Ca^{2+}] ($[Ca^{2+}]_c$) per the equation below, where R is the measured fluorescence ratio (340/380 nm) and Sf_2 and Sb_2 are the absolute 380 nm excitation/535 nm emission fluorescence under 0-[Ca^{2+}] and saturating [Ca^{2+}], respectively.

$$[Ca^{2+}] = \left(\frac{R - R_{min}}{R_{max} - R}\right)\left(\frac{Sf_2}{Sb_2}\right) * K_D$$

Thapsigargin (2 µM) was added at 100 sec to inhibit Ca^{2+} uptake into the endoplasmic reticulum (ER) and CGP37157 was added at 400 sec to inhibit NCLX-mediated mitochondrial-Ca^{2+} extrusion. After $[Ca^{2+}]_c$ reached a steady state at 700 sec, MCU-mediated Ca^{2+} uptake was

initiated by adding boluses of 1-7.5 µL of either 0.5 or 5 mM $CaCl_2$ to the cuvette to achieve increases in $[Ca^{2+}]_c$ between ~100 nM and 10 µM. The volume of $CaCl_2$ required to achieve the desired increase in $[Ca^{2+}]_c$ for each addition was calculated based on the activity coefficient for Ca^{2+} in ICM. Differences between the target $[Ca^{2+}]_c$ and the observed value recorded immediately after addition were due to unavoidable sources of experimental variability, including K_D limitations of Fura-2 and pipetting errors. After $[Ca^{2+}]_c$ was monitored for 300 sec following addition of each Ca^{2+} bolus, 2 µM CCCP was added to uncouple $\Delta\Psi_m$ and allow unimpeded Ca^{2+} efflux from mitochondria as a measure of the total extent of uptake. Under our conditions, the magnitude of the Ca^{2+} boluses added to initiate mitochondrial Ca^{2+} uptake did not significantly affect steady state $\Delta\Psi_m$ as measured with JC-1, while additions > 1µM caused a transient depolarization as measured with TMRE that recovered after ~50-60 sec.

Quantitative measurement of basal $[Ca^{2+}]_m$

HEK-293T cells grown in 25-mm glass-bottom tissue-culture dishes coated with 0.2% gelatin (~5×10^5 cells/dish) were transfected with a plasmid encoding a mitochondria-targeted version of the fluorescent calcium-indicator protein CAR-GECO1 (mito-CAR-GECO1) using TransIT-LT1 transfection reagent (Mirus). CAR-GECO1 exhibits an increase in fluorescence emission at ~610 nm upon Ca^{2+} binding with a K_D of ~490 nM. To verify localization of the probe in mitochondria, cells were imaged 48-hr post-transfection using confocal microscopy with a 40x-oil objective at 37°C. Fluorescence images of mito-CAR-GECO1 (560-nm excitation/600-750-nm emission) and MitoTracker Green (488 nm excitation/510-550 nm emission), and a transmitted-light image of each individual field, were collected within 30 sec. To qualitatively estimate basal $[Ca^{2+}]_m$, cells grown in 10-cm tissue-culture dishes were transfected with mito-CAR-GECO1 and imaged 24-hr post-transfection using an epifluorescence microscope with a 20x objective at RT. Images of live cells in complete medium in resting conditions were obtained at 545-nm excitation/620-nm emission with identical gain- and exposure-settings among experiments. Calibrated measurements of $[Ca^{2+}]_m$ were determined at 48-hr post-transfection by suspending

cells in a high Na^+/low K^+ extracellular-like medium with 2 mM $CaCl_2$. Mito-CAR-GECO1 fluorescence was monitored continuously in a high-speed spectrofluorometer until a stable intensity was achieved. Ionomycin was added to promote Ca^{2+} influx into mitochondria to saturate the probe (F_{max}), which was followed by the addition of EGTA to chelate Ca^{2+} to determine F_{min}. Fluorescence measurements were transformed to $[Ca^{2+}]_m$ using the equation

$$[Ca^{2+}] = \left(\frac{F - F_{min}}{F_{max} - F}\right) * K_D$$

where F represents the fluorescence at steady state prior to ionomycin addition.

Simultaneous measurement of $[Ca^{2+}]_c$ and $[Ca^{2+}]_m$ in response to ATP stimulation

WT and MICU2 KO (HEK-293T) cells were transiently transfected with mito-CAR-GECO1 48 hrs prior to loading with 1 µM Fura-2 AM, in HBS dye-loading solution (in mM: 135 NaCl, 5.9 KCl, 1.2 $MgCl_2$, 1.5 $CaCl_2$, 11.6 HEPES-NaOH, [pH 7.4] with 0.01% (wt/vol) pluronic F127) for 15 min at RT. After loading, ~$3x10^6$ cells were transferred to a cuvette in the temperature-controlled (37°C) experimental compartment of a multi-wavelength-excitation dual-wavelength-emission high-speed spectrofluorometer (Delta RAM, Photon Technology International). Fluorescence at 560-nm excitation/610-nm (long-pass) emission for mito-CAR-GECO1, along with 340 nm excitation/535 nm emission and 380 nm excitation/535 nm emission for the Ca^{2+}-bound and Ca^{2+}-free Fura-2 species, respectively was measured at 5 Hz. 500 µM Na_2ATP was added at 100 sec to stimulate purinergic receptors and induce $InsP_3R$-mediated ER-Ca^{2+} release. Mito-CAR-GECO1 fluorescence was calibrated as described above.

Western blotting and co-immunoprecipitation

Cells grown in in 100 mm plates were washed with PBS and lysed with RIPA buffer supplemented with protease inhibitors (cOmplete, Roche), and protein concentrations were calculated using Pierce BCA Protein Assay kit. NuPAGE© gels (4-12%) were transferred to Immobilon© P PVDF membranes and probed with various antibodies. Antibodies used were anti-

MICU1 (Cell Signaling, 12524), anti-MICU2 (Abcam, ab101465), anti-MCU (Sigma, HPA016480), anti-β-Actin (Cell Signaling, 3700S). Membranes were blocked in 5% fat-free milk for 1 hr at RT, incubated overnight at 4°C with primary antibody, and then for 2 hrs at RT with anti-rabbit IgG-HRP (Cell Signaling, 7074S) or anti-mouse IgG-HRP (Cell Signaling, 7076S) secondary antibodies conjugated to horseradish peroxidase (HRP). Chemiluminescence detection was carried out using SuperSignal West Chemiluminescent Substrate (Thermo). For co-immunoprecipitation experiments, HEK-293T cells transfected with various constructs were grown to semi-confluency at 37°C, 5% CO_2 in DMEM + 10% FBS + antibiotic/antimycotic in 150 mm plates. Cells were washed with PBS and lysed with 1 ml cold lysis buffer (50 mM HEPES-KOH pH 7.4, 150 mM NaCl, 0.2% n-dodecyl-β-D-maltoside, 0.5 mM EGTA) supplemented with protease inhibitors (cOmplete, Roche). Cells were lysed at 4°C for 30 min and centrifuged at 16,000 x g. Protein concentrations were determined, and 1 mg protein was added to anti-Flag agarose- or anti-V5 agarose-beads. Lysates and beads were rocked at 4°C for 2 hr, washed 3x with PBS before 100 µL of 2x Laemmli Sample buffer was added. Samples were boiled for 5 min, loaded into NuPAGE© 4-12% gels for electrophoresis, transferred to PVDF membranes, and probed with antibodies as described previously. All experiments were done at least in triplicate. The mean pixel density of bands for Figure 2.4E was quantified using ImageJ (NIH).

Statistical analyses

Initial Ca^{2+} uptake rates in permeabilized cells were determined for each experiment using single-exponential fits from the time of CGP37157 or Ca^{2+} addition (t = 0 sec) to achievement of a new steady state (t = 300 sec) to obtain parameters A (extent of uptake) and τ (time constant) (Igor 6 Pro). The instantaneous rate of uptake (R) at t = 0 is equal to the first derivative of the fit, and error bars (R+SD and R-SD) were calculated from standard deviations of A (SD_A) and τ (SD_τ) as follows:

$$R = A/\tau$$

$$R+SD = (A+SD_A)/(\tau-SD_\tau)$$

$$R\text{-}SD = (A\text{-}SD_A)/(\tau+SD_\tau)$$

Independent, normally distributed rate measurements and mean resting $[Ca^{2+}]_m$ from bulk-cell assays were analyzed using one-way ANOVA and Bonferroni's multiple comparisons t-test. Only pairwise comparisons between WT and each cell line are shown for clarity. Whereas unequal variances between populations are evident, assumption of equal variances rendered it less likely to find significant differences. Western blot quantification of band intensity from n = 3 independent experiments and quantification of the increase in $[Ca^{2+}]_m$ divided by the increase in $[Ca^{2+}]_c$ ($\Delta[Ca^{2+}]_m/\Delta[Ca^{2+}]_c$) in agonist-stimulated intact cells display normal distributions and approximately equal variances, and were analyzed using Student's t-test. All statistical tests were performed using GraphPad Prism 7.0. P-values < 0.05 (*) and < 0.01 (**) were considered statistically significant.

Results:

MICU1 is required to suppress MCU activity in low $[Ca^{2+}]_c$

We first examined the role of MICU1 in the previously unexplored $[Ca^{2+}]_c$ range between 100 nM and 300 nM. To measure MCU activity in this low-$[Ca^{2+}]_c$ regime, we studied permeabilized cells (Mallilankaraman et al., 2012a) in an intracellular-like medium (ICM) lacking Ca^{2+} buffers (free $[Ca^{2+}]$ ~20 nM), using the high-affinity indicator Fura-2 to measure $[Ca^{2+}]_c$, and JC-1 or TMRE to simultaneously monitor $\Delta\Psi_m$. In order to avoid changes in $\Delta\Psi_m$ due to an increase in $[Ca^{2+}]_m$, the contribution of Ca^{2+}-dependent complex I activity to proton pumping by the respiratory chain must be minimized. To achieve this, cells are permeabilized in an intracellular-like medium (ICM – see Materials and methods) containing ~20 nM free $[Ca^{2+}]$ and devoid of substrates (e.g. pyruvate) that could promote complex I enzymatic activity. Instead, 5 mM (K^+) succinate is added directly to the cell suspension as a substrate for succinate dehydrogenase, known as respiratory complex II, that oxidizes succinate to fumarate and transfers electrons to respiratory complexes III and IV, which then pump a total of 6 protons (for each electron pair) out of the matrix and allow $\Delta\Psi_m$ to be sustained independently of $[Ca^{2+}]_m$.

To verify that $\Delta\Psi_m$ under these conditions is dependent exclusively on complex II activity, we used a pharmacological approach to selectively inhibit either complex I or complex II activity and measured $\Delta\Psi_m$ in real-time using TMRE in quench mode (1 µM) as previously described (Payne et al., 2017). As shown in Figure 2.1, as soon as HEK-293T cells suspended in ICM with 5 mM succinate are permeabilized by addition of digitonin (Dg), TMRE fluorescence is quenched as the cationic dye is sequestered by mitochondria due to the large negative $\Delta\Psi_m$ and reaches a steady state within 30-50 sec. Subsequent addition of 2 µM thapsigargin (Tg) to prevent Ca^{2+}-reuptake by the ER at t = 100 sec has minimal effect of on the steady-state $\Delta\Psi_m$. Similarly, a series of five bolus additions of 500 nM rotenone, which has been shown previously to inhibit complex I at concentrations between 100 nM and 1 µM (Han et al., 2014)(Passmore et al., 2017), has no effect on the steady-state TMRE fluorescence, providing strong evidence that $\Delta\Psi_m$ is

independent of complex I activity under these conditions. The mitochondrial uncoupler CCCP (2 µM) is then added at the end of each experiment (t = 400 sec) to measure the TMRE fluorescence in the absence of $\Delta\Psi_m$.

Antimycin A has been shown previously to specifically inhibit the activity of complex III at concentrations of ~10 µM (Wang et al., 2015). Because complex II does not itself pump protons out of the matrix, but rather transfers electrons to complex II to provide energy to power its proton transport activity, antimycin A should fully inhibit all complex II-dependent respiration. Unlike rotenone, addition of 500 nM antimycin A to permeabilized cells with 2 µM Tg causes a rapid increase in TMRE fluorescence. Subsequent additions of 500 nM antimycin A or 2 µM CCCP cause no additional increase in TMRE fluorescence. This result indicates that, even at low concentrations, antimycin A completely inhibits complex III and in turn prevents activity of complex II from maintaining $\Delta\Psi_m$. Thus, under these assay conditions mitochondria establish and maintain their large negative $\Delta\Psi_m$ exclusively through succinate dehydrogenase activity in the presence of excess (5 mM) substrate, allowing them to remain energized independently of $[Ca^{2+}]_m$.

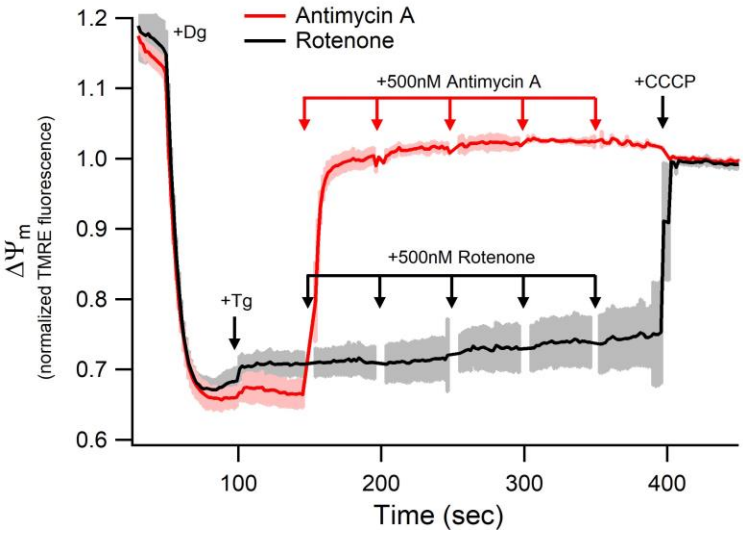

Figure 2.1. Inner mitochondrial membrane potential is maintained exclusively through complex II activity in permeabilzed cells

$\Delta\Psi_m$ measured with TMRE for permeabilized HEK-293T cells suspended in ICM with 5 mM succinate. Cells were treated with 0.004% digitonin (Dg) to permeabilize plasma membrane and 2 µM thapsigargin (Tg) to block ER Ca^{2+} uptake at t = 50 and 100 sec respectively, as indicated. Addition of 500 nM Antimycin A (red trace) inhibits proton pumping by complexes III and IV leading to a complete depolarization of $\Delta\Psi_m$. 0.5-2.5 µM Rotenone to inhibit complex I activity (black trace) has minimal effect on $\Delta\Psi_m$. CCCP (2 µM) was added at t = 400 sec to dissipate $\Delta\Psi_m$ and induce efflux of accumulated mitochondrial Ca^{2+}.TMRE fluorescence is normalized to the steady-state after addition of CCCP. Traces are the mean of n = 3 independent experiments (dark traces) +/- SEM (light shading) for each condition.

Under these conditions, the MCU plays a dominant role in determining $[Ca^{2+}]_c$ since, addition of a Ca^{2+} bolus to rapidly raise $[Ca^{2+}]_c$ to 5 µM was followed by clearance of Ca^{2+} over

100-200 seconds in wild-type (WT) cells but not in cells with *MCU* genetically-deleted (MCU KO) (Figure 2.2). Subsequent dissipation of $\Delta\Psi_m$ by CCCP caused a rapid $[Ca^{2+}]_c$ increase in WT cells, providing further evidence that mitochondria were responsible for Ca^{2+} uptake in response to a rise of $[Ca^{2+}]_c$ (Figure 2.2).

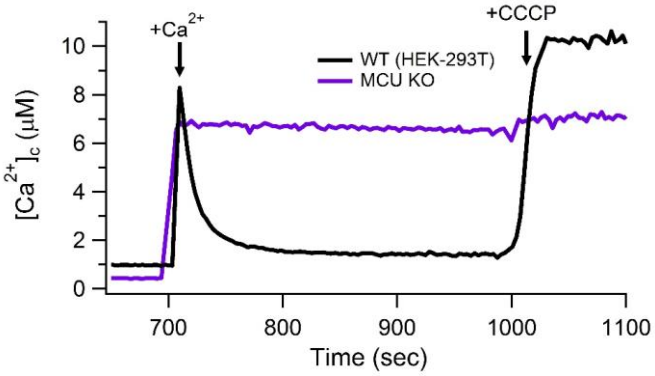

Figure 2.2. Rapid Ca^{2+} uptake is mediated by MCU

Mitochondrial clearance of bath $[Ca^{2+}]$ ($[Ca^{2+}]_c$) in response to acute increase of $[Ca^{2+}]_c$ by 5 μM in permeabilized MCU KO and WT (HEK-293T) cells. Cells were treated with Dg, Tg, and 20 μM CGP37157 to inhibit mitochondrial Ca^{2+} efflux at t = 50, 100 and 400 sec, respectively. CCCP was added at t = 1000 sec to dissipate $\Delta\Psi_m$ and induce efflux of mitochondrial Ca^{2+}.

Upon attainment of a quasi-steady state $[Ca^{2+}]_c$ ~300 sec following thapsigargin (Tg) treatment to eliminate confounding influences of the ER, addition of CGP37157 to inhibit NCLX caused no change in $[Ca^{2+}]_c$ in WT or MCU KO cells (Figure 2.4A-B), indicating that mitochondrial Ca^{2+} uptake and extrusion were inactive. In contrast, it resulted in a prompt decrease in $[Ca^{2+}]_c$ in cells lacking MICU1 (Figure 2.3B; Figure 2.4A-B: red), indicating that Ca^{2+} uptake was ongoing, balanced by NCLX-mediated extrusion (Figure 2.3A).

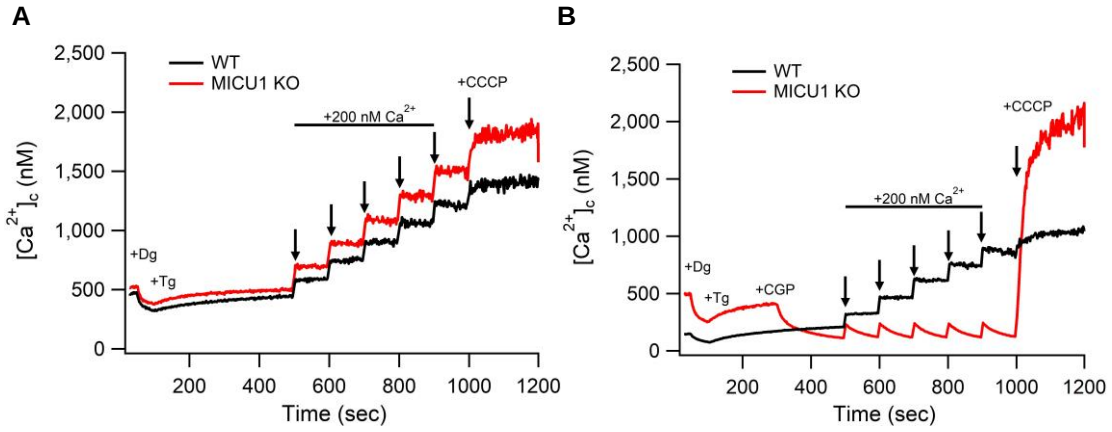

Figure 2.3. Ca^{2+} efflux through NCLX compensates for constitutive MCU activity in MICU1 KO cells

(**A**) $[Ca^{2+}]_c$ in WT or MICU1 KO cells measured with the high-affinity indicator Fura-2. A series of bolus addition of 200 nM free-$Ca^{2+}$are added beginning at t = 500 sec. 2 μM CCCP was added at t = 1000 sec. Representative traces from n > 3 independent replicates for each cell line shown. No Ca^{2+}-uptake is observed in either cell line. (**B**) $[Ca^{2+}]_c$ measurements as described in (A) with 20 μM CGP37157 (CGP) added t = 300 sec to inhibit NCLX activity. Representative traces from n > 3 independent replicates for each cell line shown. Inhibition of mitochondrial Ca^{2+} efflux through NCLX reveals constitutive MCU-mediated Ca^{2+} uptake at low $[Ca^{2+}]_c$ in MICU1 KO cells (red trace) whereas minimal uptake is observed in WT cells (black trace).

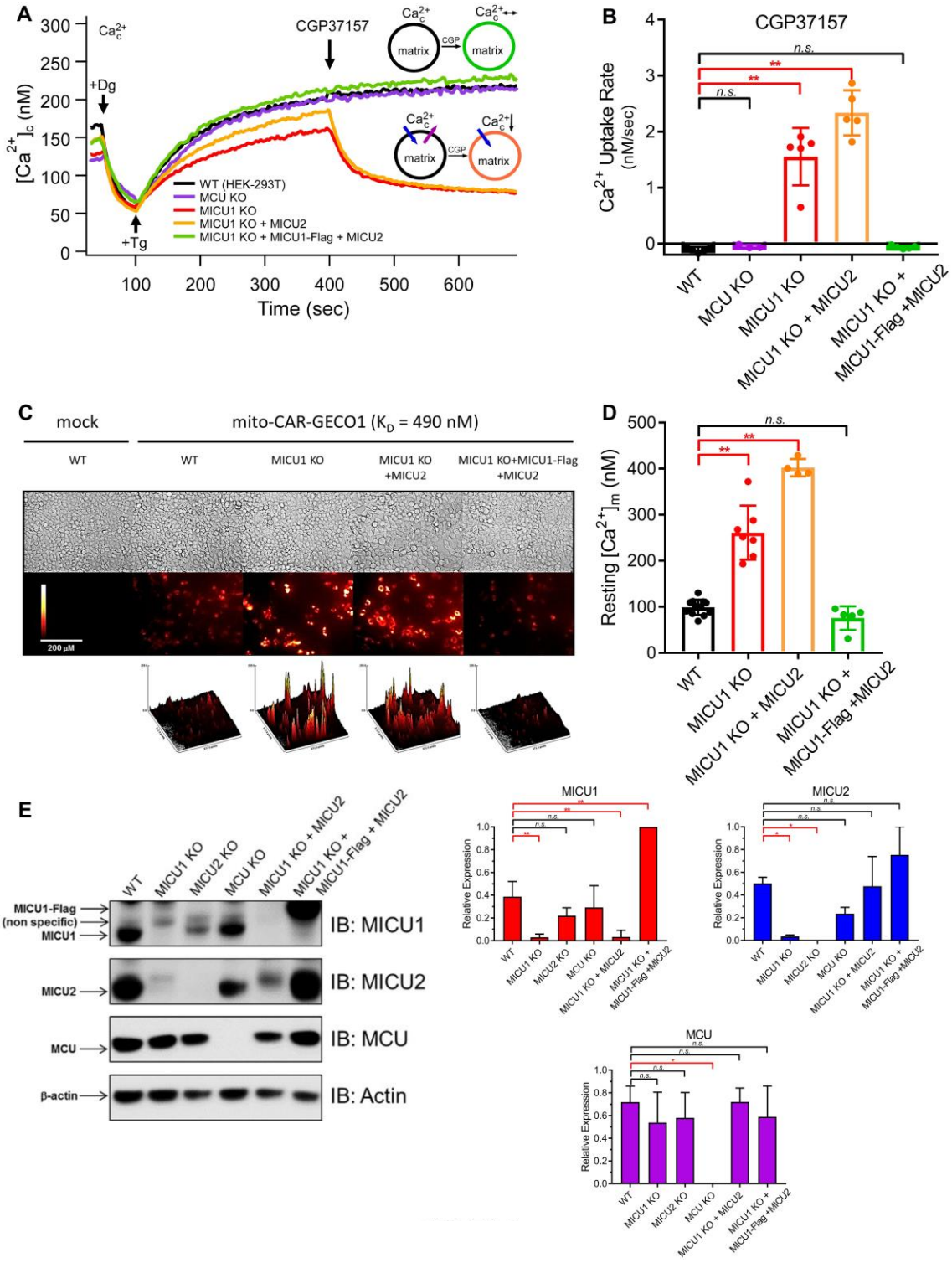
A
B
C
D
E
CGP37157
+Dg
+Tg
Time (sec)
WT (HEK-293T)
MCU KO
MICU1 KO
MICU1 KO + MICU2
MICU1 KO + MICU1-Flag + MICU2
matrix
CGP
Ca2+ Uptake Rate (nM/sec)
n.s.
WT
MCU KO
MICU1 KO
MICU1 KO + MICU2
MICU1 KO + MICU1-Flag +MICU2
mock
mito-CAR-GECO1 (KD = 490 nM)
MICU1 KO +MICU2
MICU1 KO+MICU1-Flag +MICU2
200 μM
Resting [Ca2+]m (nM)
MICU1-Flag
(non specific)
MICU1
MICU2
MCU
β-actin
IB: MICU1
IB: MICU2
IB: MCU
IB: Actin
Relative Expression

Figure 2.4

Figure 2.4. MICU1, but not MICU2, is required to suppress MCU activity in low $[Ca^{2+}]_c$

(**A**) $[Ca^{2+}]_c$ in WT, MCU KO, MICU1 KO, MICU1 KO cells with MICU2 re-expressed, and MICU1 KO cells with MICU2 and MICU1-Flag expressed (rescue) measured with the high-affinity indicator Fura-2. Cells were treated with Dg, Tg, and CGP at t = 50, 100 and 400 sec, respectively, as indicated. Representative traces from n ≥ 5 independent replicates for each cell line shown. As shown in schematic inset, rates of MCU-mediated Ca^{2+} uptake and NCLX-mediated Ca^{2+} extrusion are equal in the steady-state. Inhibition of extrusion by CGP reveals ongoing MCU-mediated Ca^{2+} uptake in MICU1 KO and [MICU1 KO+MICU2] cells, whereas no effect is observed in the other cell types, indicating that MCU was not active. (**B**) Quantification of initial mitochondrial Ca^{2+}-uptake rate in response to inhibition of NCLX-mediated Ca^{2+} efflux for cell lines in (A). Each point represents initial Ca^{2+} uptake rate from an independent experiment (n = 5 for each condition) determined by single-exponential fit to reduction of $[Ca^{2+}]_c$. Bars: mean +/- SEM (*P < 0.05; **P < 0.01; n.s, not different; Bonferroni's multiple comparisons test). (**C**) Basal mito-CAR-GECO1 fluorescence in WT or MICU1 KO HEK-293T cells stably expressing MICU1 and/or MICU2, imaged at 20x magnification. Surface plots: relative fluorescence intensity histograms. (**D**) $[Ca^{2+}]_m$ for cell lines in (C), calibrated from mito-CAR-GECO1 fluorescence. Each point represents an independent experiment. (WT: n = 12; MICU1 KO: n = 7; [MICU1 KO+MICU2]: n = 4; MICU1-rescue: n = 5) Bars: mean $[Ca^{2+}]_m$ +/- SEM. (*P < 0.05; **P < 0.01; n.s, not different; Bonferroni's multiple comparisons test). (**E**) Western blots of MICU1, MICU2, MCU and β-actin from cells as labeled. Quantification from n = 3 independent experiments normalized for b-actin intensity shown at right. (* P < 0.05; ** P < 0.01; n.s, not different; Student's t-test).

Clearance of cytoplasmic Ca^{2+} in MICU1 KO cells was blocked by Ru360 (1 μM – not shown), indicating that it was mediated by MCU. These results recapitulate previous observations that MCU-mediated Ca^{2+} uptake in low $[Ca^{2+}]_c$ is strongly enhanced in the absence of MICU1 (Mallilankaraman et al., 2012b)(Csordás et al., 2013)(Patron et al., 2014) (Liu et al., 2016). Using a genetically-encoded Ca^{2+} indicator targeted to the mitochondrial matrix (mito-CAR-GECO1; K_D = 490 nM; Figure 2.4C) (Wu et al., 2013), $[Ca^{2+}]_m$ in WT cells was ~100 nM whereas it was increased over 3-fold to ~300-400 nM in MICU1 KO cells (Figure 2.4D). Thus, MICU1 is required to inhibit MCU activity in the low-$[Ca^{2+}]_c$ regime, and in its absence the rate of Ca^{2+} influx is sufficient to raise resting $[Ca^{2+}]_m$.

MICU2 expression was substantially reduced in cells lacking MICU1 (Figure 2.4E). Accordingly, loss of MCU gatekeeping and constitutively elevated $[Ca^{2+}]_m$ observed in MICU1 KO cells here and other studies could be caused or modified by loss of MICU2. Expression of MICU1-Flag alone in MICU1 KO cells rescued MICU2 expression to endogenous levels only when MICU1-Flag was expressed at greater than endogenous levels (Figure 2.5A-B). In contrast, stable expression of both MICU1-Flag and MICU2 (Figure 2.4E & 2.5B) in MICU1 KO cells (hereafter defined as MICU1-rescue cells) completely rescued gatekeeping (Figure 2.4A-B) and restored $[Ca^{2+}]_m$ to WT levels (Figure 2.4C-D). Together, these results demonstrate that MICU1 is required for MCU gatekeeping in the low-$[Ca^{2+}]_c$ regime.

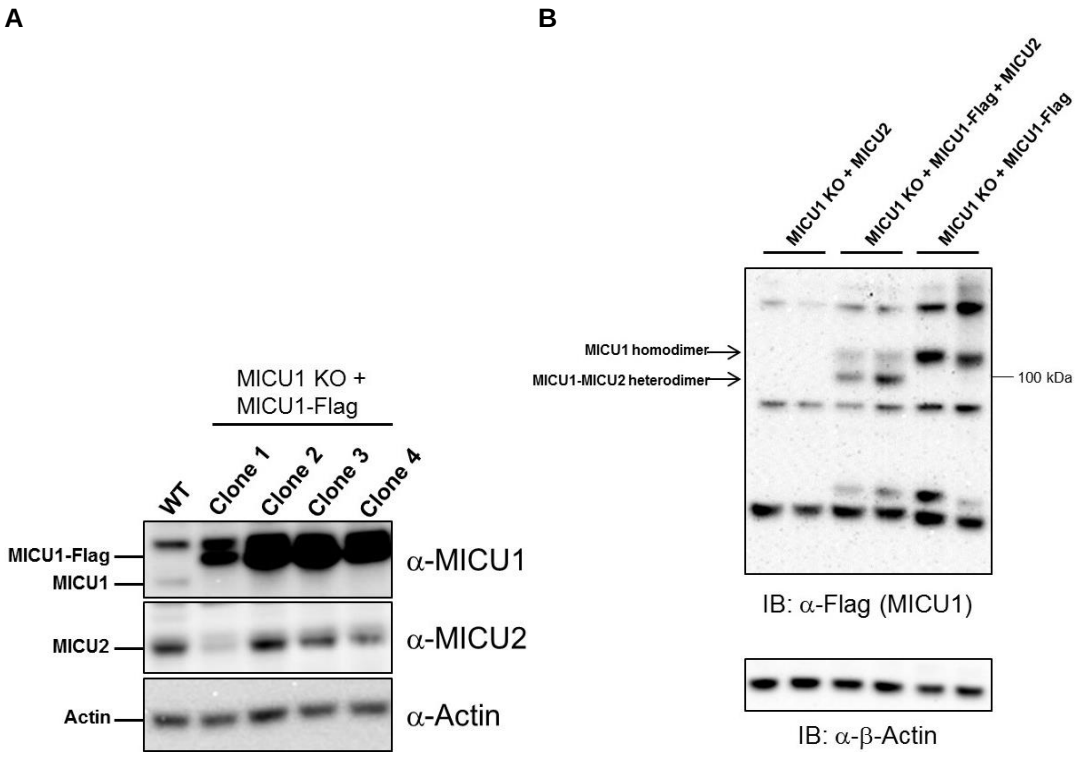

Figure 2.5. Expression of MICU1-Flag in MICU1 KO cells does not rescue MICU2 expression

(**A**) Western blots of MICU1, MICU2, and β-actin from WT and four clonal MICU1 KO cell lines with stable expression of MICU1-Flag. Endogenous MICU2 expression is rescued when MICU1-Flag is overexpressed. (**B**) Western blots of anti-Flag (MICU1) in MICU1 KO cell lines with stable expression of MICU1-Flag with or without expression of MICU2. MICU1-MICU2 heterodimers are observed only when both MICU1-Flag and MICU2 are overexpressed.

Gatekeeping of MCU is cooperatively relieved when $[Ca^{2+}]_c$ exceeds ~1.3 μM

Physiological $[Ca^{2+}]_c$ signals can generate increases in $[Ca^{2+}]_m$, indicating that MCU gatekeeping is relieved when $[Ca^{2+}]_c$ is elevated. Nevertheless, quantitative measurements of the precise $[Ca^{2+}]_c$ that govern this process are limited. We therefore evaluated the $[Ca^{2+}]_c$-dependence of MCU-mediated Ca^{2+}-uptake over a range of $[Ca^{2+}]_c$ in WT and MICU1 KO cells. In each experiment, cells were challenged with a calibrated bolus of $CaCl_2$ to increase $[Ca^{2+}]_c$ to between 100 nM and 10 μM, and $[Ca^{2+}]_c$ was monitored until a steady state was reached (Figure 2.7A-B). $\Delta\Psi_m$ remained essentially unchanged when measured with JC-1. TMRE, a $\Delta\Psi_m$ probe with faster kinetics, revealed only small transient depolarizations (Figure 2.6).

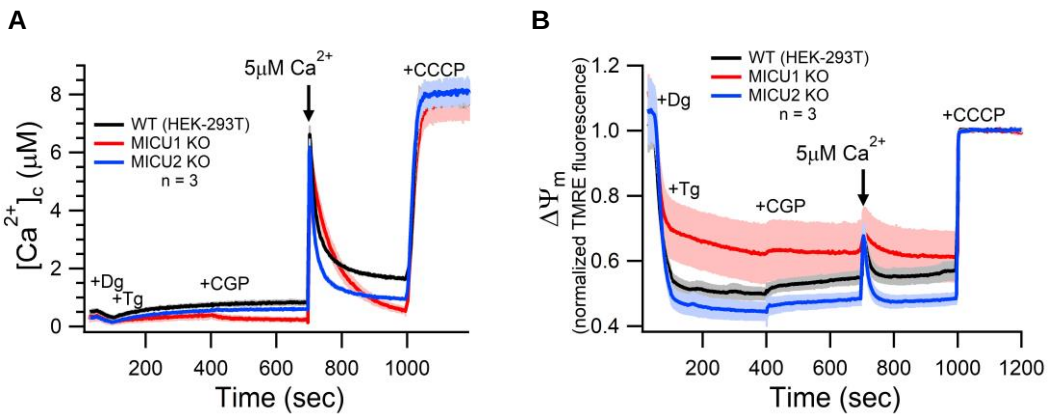

Figure 2.6. $\Delta\Psi_m$ during Ca^{2+} uptake in WT, MICU1 KO, and MICU2 KO cells measured with TMRE

(**A**) $[Ca^{2+}]_c$ responses to acute increase of $[Ca^{2+}]_c$ by 5 μM in low-$[Ca^{2+}]$ intracellular-like medium of WT (black), MICU1 KO (red), and MICU2 KO (blue) cells treated with digitonin (Dg), thapsigargin (Tg) and CGP37157 (CGP). Mean (dark traces; n = 3 replicates) +/- SEM (light shading). (**B**) TMRE fluorescence during experiments in (A). Transient increase in TMRE fluorescence in response to addition of 5 μM Ca^{2+} represents IMM depolarization followed by a repolarization after ~50-60 sec.

In WT cells in the presence of CGP37157, mitochondrial Ca^{2+} uptake was negligible in response to Ca^{2+} additions that raised $[Ca^{2+}]_c$ to 800 nM, such that the measured $[Ca^{2+}]_c$ was approximately equal to that which had been added. Thus, gatekeeping was fully intact up to 800 nM $[Ca^{2+}]_c$ (Figure 2.7C – black traces). Between 800 nM and 1.5 μM $[Ca^{2+}]_c$, very slow Ca^{2+} uptake reduced $[Ca^{2+}]_c$ < 20% over the subsequent 300 sec. To quantify the $[Ca^{2+}]_c$ threshold above which gatekeeping is relieved, the final $[Ca^{2+}]_c$ at steady state was plotted as a function of the initial $[Ca^{2+}]_c$ after bolus addition. This relationship was approximately linear with a slope of ~1 for MCU KO cells, as expected (Figure 2.7D & F). A plot for WT cells also yielded a slope of ~1 in the $[Ca^{2+}]_c$ regime up to ~1 μM (Figure 2.7D), reflecting strong inhibition of MCU channel activity. In contrast, Ca^{2+} uptake in MICU1 KO cells was robust (Figure 2.7C – red traces), reflecting lack of gatekeeping, which reduced the steady state post-pulse $[Ca^{2+}]_c$ to below 150 nM (Figure 2.7C & D). Plots of final steady state $[Ca^{2+}]_c$ as a function of the initial $[Ca^{2+}]_c$ had slopes of ~0 for both MICU1 KO and [MICU1 KO+MICU2] cells, demonstrating loss of gatekeeping in the absence of MICU1 (Figure 2.7D). In contrast, WT behavior was recapitulated in MICU1-rescue cells.

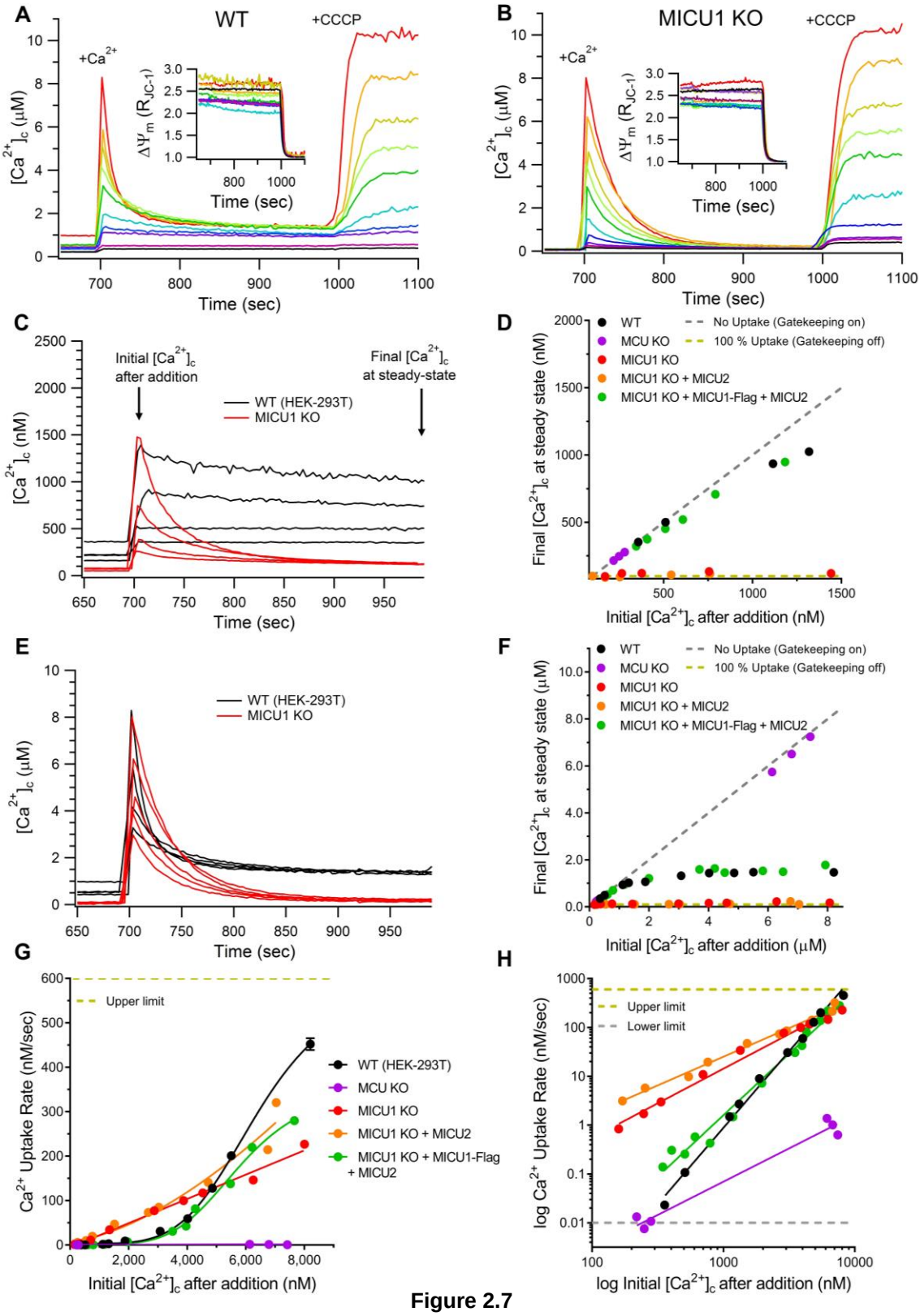
A
WT
+CCCP
+Ca2+
[Ca2+]c (μM)
ΔΨm (RJC-1)
Time (sec)
B
MICU1 KO
+CCCP
+Ca2+
[Ca2+]c (μM)
ΔΨm (RJC-1)
Time (sec)
C
Initial [Ca2+]c after addition
Final [Ca2+]c at steady-state
WT (HEK-293T)
MICU1 KO
[Ca2+]c (nM)
Time (sec)
D
WT
MCU KO
MICU1 KO
MICU1 KO + MICU2
MICU1 KO + MICU1-Flag + MICU2
No Uptake (Gatekeeping on)
100 % Uptake (Gatekeeping off)
Final [Ca2+]c at steady state (nM)
Initial [Ca2+]c after addition (nM)
E
WT (HEK-293T)
MICU1 KO
[Ca2+]c (μM)
Time (sec)
F
WT
MCU KO
MICU1 KO
MICU1 KO + MICU2
MICU1 KO + MICU1-Flag + MICU2
No Uptake (Gatekeeping on)
100 % Uptake (Gatekeeping off)
Final [Ca2+]c at steady state (μM)
Initial [Ca2+]c after addition (μM)
G
Upper limit
WT (HEK-293T)
MCU KO
MICU1 KO
MICU1 KO + MICU2
MICU1 KO + MICU1-Flag + MICU2
Ca2+ Uptake Rate (nM/sec)
Initial [Ca2+]c after addition (nM)
H
Upper limit
Lower limit
log Ca2+ Uptake Rate (nM/sec)
log Initial [Ca2+]c after addition (nM)

Figure 2.7

Figure 2.7. Gatekeeping of MCU is relieved above ~1.3 μM $[Ca^{2+}]_c$

(**A-B**) Mitochondrial Ca^{2+} uptake in suspensions of permeabilized WT (A) and MICU1 KO (B) cells in response to acute increases of $[Ca^{2+}]_c$ to between ~0.1 and 10 μM. Individual traces from independent experiments with different bolus additions shown. Insets show relative $\Delta\Psi_m$ over the same period. After monitoring uptake for 300 sec, CCCP uncoupled $\Delta\Psi_m$ and released matrix Ca^{2+} content. (**C**) Mitochondrial Ca^{2+}-uptake in WT (black traces) and MICU1 KO (red) in response to Ca^{2+} additions that elevated $[Ca^{2+}]_c$ to 0.3-1.5 μM. (**D**) Steady state $[Ca^{2+}]_c$ 300 sec after initiation of uptake, plotted as function of initial $[Ca^{2+}]_c$ between 0-1.5 μM. Each point represents an independent experiment. Dashed lines: theoretical fits representing no uptake (gray, slope = 1) or 100% uptake (yellow, slope = 0). WT and MICU1-rescue cells demonstrated negligible uptake at $[Ca^{2+}]_c$ < 1 μM. (**E**) Mitochondrial Ca^{2+} uptake in WT (black traces) and MICU1 KO (red traces) cells in response to Ca^{2+} additions that elevated $[Ca^{2+}]_c$ to 3-8 μM. (**F**) Same as in (D) for $[Ca^{2+}]_c$ between 0-8 μM. Above 2 μM $[Ca^{2+}]_c$, uptake proceeds until $[Ca^{2+}]_c$ reaches ~1.5 μM. (**G**) Ca^{2+}-uptake rates in response to acute challenge with $[Ca^{2+}]_c$ between 0.1-9 μM. Each point represents an independent experiment. Solid lines: Hill-Equation fits of Ca^{2+}-uptake rate vs. $[Ca^{2+}]_c$ plotted on linear scale. Dashed yellow line: upper limit of Ca^{2+}-uptake rate determinations. Error bars: standard deviation in fit parameters A (extent) and τ (time constant). Error bars for some points are too small to be visible. (**H**) Linear fits of $\log_{10}$ transformed values in (G) that demonstrate cooperativity of MCU activation and highlight differences in Ca^{2+}-uptake rates at low (< 1 μM) $[Ca^{2+}]_c$. Dashed lines represent upper (yellow) or lower (gray) limits of Ca^{2+}-uptake rate determinations.

Ca^{2+} boluses that elevated $[Ca^{2+}]_c$ to between 2-10 μM activated Ca^{2+} uptake in WT cells, which rapidly reduced post-pulse $[Ca^{2+}]_c$ to near the gatekeeping threshold of 1.2-1.5 μM within 2-3 minutes (Figure 2.7E – black traces). Plots of final steady state $[Ca^{2+}]_c$ as a function of the initial $[Ca^{2+}]_c$ exhibited a slope of ~0 (no gatekeeping) above this $[Ca^{2+}]_c$ threshold (Figure 2.7F). In contrast, in MICU1 KO cells (Figure 2.7E – red traces) as well as in MICU1 KO cells with MICU2 re-expressed, Ca^{2+} uptake reduced steady state $[Ca^{2+}]_c$ to below 150 nM. MICU1-rescue cells recapitulated WT behavior (Figure 2.7F – green). These results suggest that MICU1-dependent MCU gatekeeping is relieved when $[Ca^{2+}]_c$ exceeds a threshold of ~1 μM, but then becomes re-engaged following MCU activation when uptake reduces $[Ca^{2+}]_c$ to 1-1.5 μM. Moreover, the transition of MCU from inactive to active states in WT cells is $[Ca^{2+}]_c$ dependent, with MCU activity in WT cells surpassing the activity observed in MICU1 KO cells at $[Ca^{2+}]_c$ > 5 μM (Figure 2.7E).

To gain insights into the mechanisms that underlie $[Ca^{2+}]_c$-dependent MCU activation, we measured uptake rates over a wide range of imposed $[Ca^{2+}]_c$. There was a non-zero Ca^{2+} uptake in MCU KO cells that increased linearly with $[Ca^{2+}]_c$, mediated by an unknown MCU-independent mechanism. MCU was active in cells lacking MICU1 up to ~5 μM $[Ca^{2+}]_c$, with the uptake rate a linear function of initial $[Ca^{2+}]_c$ (Figure 2.7G), suggesting that uptake in these cells is driven solely by the imposed $[Ca^{2+}]$ gradient across the IMM at constant $\Delta\Psi_m$. In contrast, Ca^{2+} uptake in WT and MICU1-rescue cells was suppressed relative to MICU1 KO cells until $[Ca^{2+}]_c$ exceeded ~5 μM, but then increased with higher $[Ca^{2+}]_c$ to rates exceeding those observed in MICU1 KO cells

(Figure 2.7E & G - red). Accordingly, the relationship between the initial $[Ca^{2+}]_c$ and rate of MCU-mediated Ca^{2+} uptake was non-linear (Figure 2.7G), indicating cooperativity in the transition from "gatekeeping on" to "gatekeeping off" states. This suggests that MICU1 contributes to cooperative activation of MCU, as suggested in some studies, although the cooperativity here did not require Mg^{2+} (Csordás et al., 2013).

The role of MICU1 in gatekeeping at low (< 1 μM) $[Ca^{2+}]_c$ and activation at higher $[Ca^{2+}]_c$ is more clearly seen in a logarithmic plot (Figure 2.7H). A slope of 1.4 was observed for cells lacking MICU1, whereas slopes of 3.1 and 2.5 were observed for WT and MICU1-rescue cells, respectively (Table 2.1). These findings demonstrate that, in addition to establishing a $[Ca^{2+}]_c$ threshold below which MCU activity is suppressed, MICU1 is necessary for the cooperative $[Ca^{2+}]_c$-dependent activation of mitochondrial Ca^{2+} uptake once the threshold is exceeded.

MICU2 interacts with MICU1 to increase the $[Ca^{2+}]_c$ threshold and reduce the gain of cooperative activation of MCU activity

MICU1 and MICU2 exist as a disulfide-linked heterodimer (Patron et al., 2014) (Petrungaro et al., 2015). In non-reducing western blots, a single band with reactivity to both MICU1 and MICU2 antibodies was observed at ~95 kDa in WT cells, representing a MICU1/2 heterodimer (Figure 2.8A). MICU1 was detected as a homodimer at ~100 kDa in MICU2 KO cells (Figure 2.8A). MICU1 was also detected as a ~100 kDa band by co-immunoprecipitation with MCU (Figure 2.8B), suggesting that the MICU1-homodimer can interact with the MCU complex. In WT cells expressing V5-tagged MCU, MICU2 was co-immunoprecipitated with MCU, whereas MCU failed to pull down MICU2 in the absence of MICU1 (Figure 2.9). Thus, MICU1 is required for interaction of MICU2 with the MCU complex, in agreement with previous studies (Patron et al., 2014)(Kamer and Mootha, 2014)(Petrungaro et al., 2015).

It has been proposed that MICU2 rather than MICU1 is responsible for inhibition of MCU activity in the low-$[Ca^{2+}]_c$ regime (Patron et al., 2014). Two results argue against this: First, genetic deletion of MICU2, which did not reduce MICU1 expression (Figure 2.4E) or abolish interaction of MICU1 with MCU (Figure 2.8B), had no effect on gatekeeping in the 100-300 nM

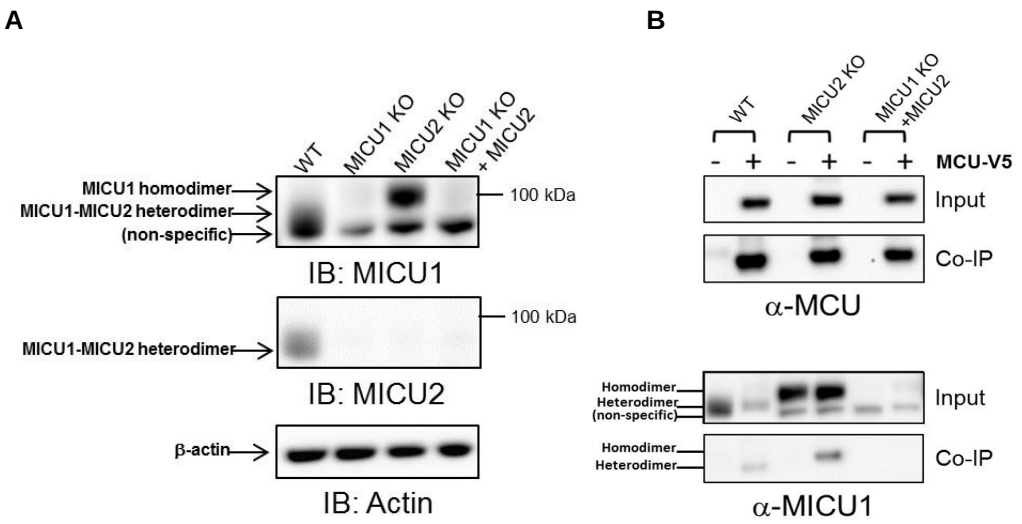

Figure 2.8. MICU1 homodimers interact with MCU

(**A**) Western blots of whole-cell lysates for MICU1 (top row), MICU2 (middle) or β-actin (bottom) from WT, MICU1 KO, MICU2 KO or [MICU1 KO+MICU2] HEK-293T cells under non-reducing conditions. Bands at ~95 kDa represent disulfide-linked MICU1-MICU2 heterodimers in WT cells and MICU1-MICU1 homodimers in MICU2 KO cells. Bands near 90 kDa observed in MICU1 KO, MICU2 KO and [MICU1 KO+MICU2] cells are due to non-specific antibody binding. (**B**) Immunoblots of whole-cell lysates with anti -MCU and anti-MICU1 antibodies shown. A homodimer of MICU1 (~100 kDa) is immunoprecipitated with MCU-V5 (bottom/lane 4) in MICU2 KO cells while a smaller molecular weight band (~95 kDa) corresponding to the size of the MICU1-MICU2 heterodimer is immunoprecipitated with MCU-V5 in WT cells (bottom/lane 2).

$[Ca^{2+}]_c$ regime (Figure 2.10A) or on resting $[Ca^{2+}]_m$ (Figure 2.10B-C). Second, re-expression of MICU2 in MICU1 KO cells (Figure 2.4E) failed to rescue loss of gatekeeping (Figure 2.4A-B & 2.11A - orange) or restore $[Ca^{2+}]_m$ (Figure 2.4C-D and 2.11B-C - orange). Thus, MICU2 does not mediate MCU gatekeeping in the low-$[Ca^{2+}]_c$ regime, and gatekeeping in MICU2 KO cells was mediated by MICU1 monomers or homodimers.

To further examine the role of MICU2, we measured Ca^{2+} uptake and $\Delta\Psi_m$ in cells challenged with boluses of Ca^{2+}

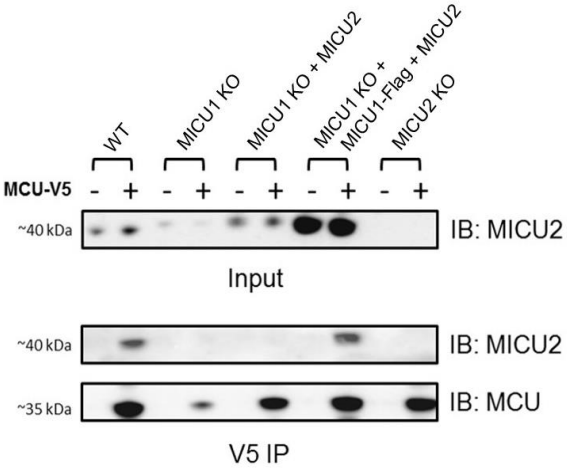

Figure 2.9. MICU2 cannot interact with MCU in MICU1 KO cells

anti-V5 immunoprecipitation in WT, MICU1 KO (with or without stable expression of MICU2, or with MICU1-Flag and MICU2 expressed together (MICU1-rescue)), or MICU2 KO HEK-293T cells with (+) or without (-) transient-transfection of MCU-V5-His. MCU immunoprecipitation failed to co-precipitate MICU2 in the absence of MICU1.

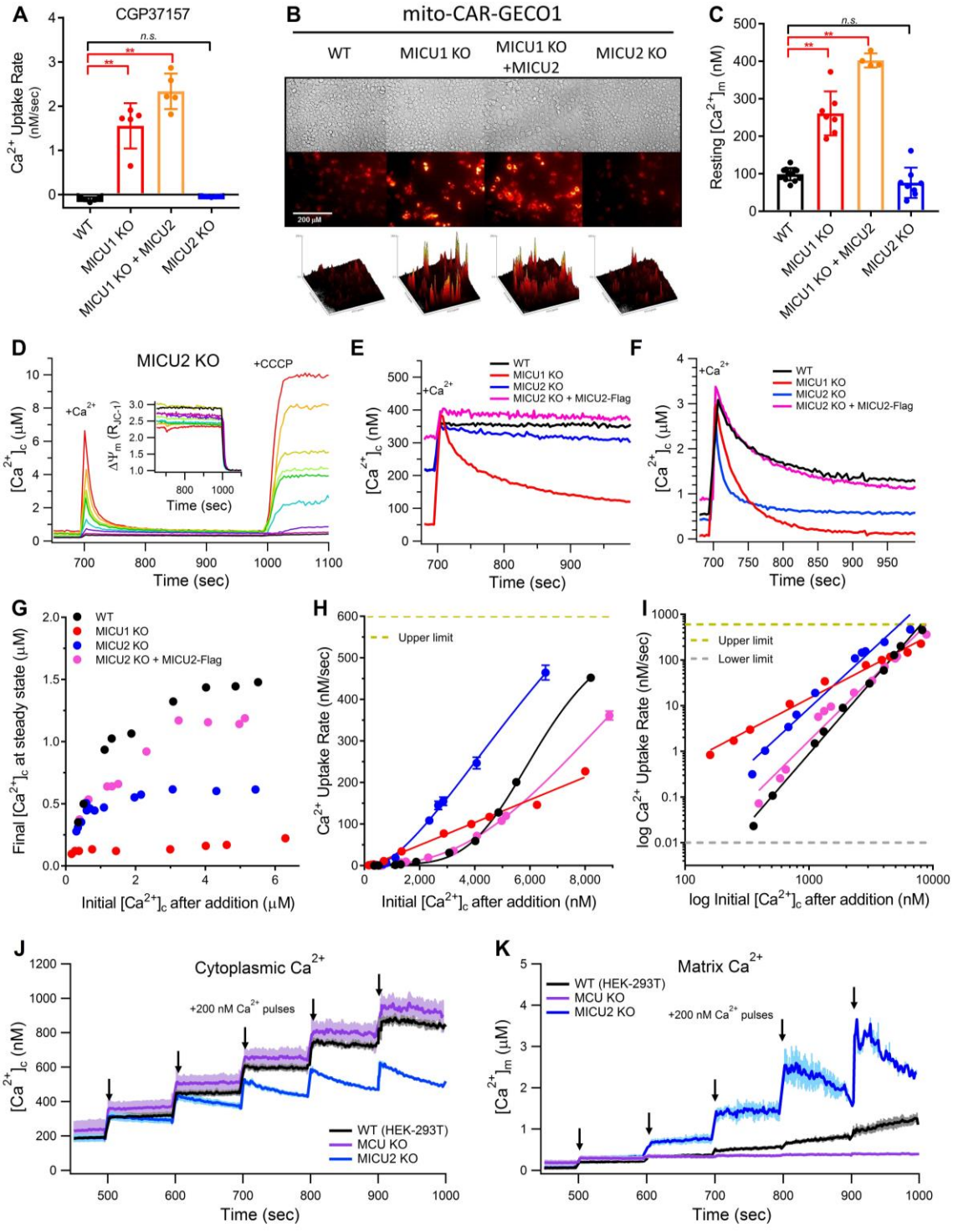

Figure 2.10

between 100 nM and 10 µM (Figure 2.10D). MICU2 KO cells exhibited strong gatekeeping at $[Ca^{2+}]_c$ < 500 nM (Figure 2.10E). Remarkably, the Ca^{2+}-uptake rate increased dramatically when

Figure 2.10. MICU1-MICU2 heterodimers increase the $[Ca^{2+}]_c$ threshold for MCU activation

(**A**) Initial rates of mitochondrial Ca^{2+} uptake in low $[Ca^{2+}]_c$ (100-300 nM) revealed by inhibition of NCLX. Each point represents an independent experiment (n = 5 for each condition). Bars: mean +/- SEM (* $P < 0.05$; ** $P < 0.01$; n.s, not different; Bonferroni's multiple comparisons test). (**B**) Basal mito-CAR-GECO1 fluorescence at 20x magnification. Surface plots: fluorescence intensity histograms. (**C**) $[Ca^{2+}]_m$ calibrated from mito-CAR-GECO1 fluorescence (MICU2 KO: n = 8). Bars: mean $[Ca^{2+}]_m$ +/- SEM. (*$P < 0.05$; **$P < 0.01$; n.s, not different; Bonferroni's multiple comparisons test). (**D**) Mitochondrial Ca^{2+} uptake in MICU2 KO cells in response to Ca^{2+} additions that elevated $[Ca^{2+}]_c$ to 0.2-7 µM. Each color represents an independent experiment with a single Ca^{2+} bolus. Relative $\Delta\Psi_m$ for each corresponding trace shown (inset). (**E-F**) $[Ca^{2+}]_c$ responses to bolus additions of Ca^{2+} to increase $[Ca^{2+}]_c$ to 300-400 nM (E) or 2.5-3.5 µM (F). Representative traces shown from n $\geq$ 2 independent replicates for each cell line. (**G**) Steady-state $[Ca^{2+}]_c$ 300 s after initiation of uptake, plotted as function of initial $[Ca^{2+}]_c$ between 0.1 – 7 µM. $[Ca^{2+}]_c$ achieves steady-state at ~500 nM in MICU2 KO cells compared with 1-1.5 µM in WT cells. (**H-I**) Ca^{2+}-uptake rates in response to acute challenge with $[Ca^{2+}]_c$ between 0.1-9 µM. Each point represents an independent experiment. Solid lines: Hill-Equation (H) or linear (I) fits of Ca^{2+}-uptake rate vs. $[Ca^{2+}]_c$ plotted on linear (H) or $\log_{10}$ (I) scales. Activation of Ca^{2+} uptake in MICU2 KO cells exhibits similar cooperativity to WT cells, but the entire curve is left-shifted. (**J-K**) Simultaneous measurements of $[Ca^{2+}]_c$ (J) and $[Ca^{2+}]_m$ (K) in permeabilized cells in response to successive bolus additions of Ca^{2+} each increasing $[Ca^{2+}]_c$ by 200 nM. Lines (dark colors) represent mean of n = 3 independent experiments with error bars (light colors) representing SEM. Concurrent decrease in $[Ca^{2+}]_c$ and increase in $[Ca^{2+}]_m$ is observed in MICU2 KO cells above ~400 nM $[Ca^{2+}]_c$.

$[Ca^{2+}]_c$ was elevated to ~3 µM, exceeding that in WT and MICU1 KO cells (Figure 2.10F). This behavior was rescued by re-expression of MICU2-Flag. When final steady state $[Ca^{2+}]_c$ was plotted against initial $[Ca^{2+}]_c$, the slope of the line at $[Ca^{2+}]_c$ < 500 nM was ~1 (gatekeeping on), but it decreased to a slope of ~0 at higher initial $[Ca^{2+}]_c$ (gatekeeping off), to a final steady state ~500 nM, a level between that observed in WT cells and MICU1 KO cells (Figure 2.10G). This suggests that MICU2 plays a role in tuning the MICU1-regulated MCU-gatekeeping threshold. To verify that the normal MCU-activation threshold of ~1.3 µM $[Ca^{2+}]_c$ was indeed reduced to ~500 nM in MICU2 KO cells, we simultaneously measured Ca^{2+} clearance from the cytoplasm and uptake into the matrix in permeabilized cells. Below ~1 µM $[Ca^{2+}]_c$, small (~200 nM) Ca^{2+} pulses produced step-changes in $[Ca^{2+}]_c$ and small or negligible changes in $[Ca^{2+}]_m$ in WT and MCU KO cells, respectively, whereas Ca^{2+} uptake (i.e. reduction in $[Ca^{2+}]_c$, Figure 2.10J), and concurrent increase in $[Ca^{2+}]_m$ (Figure 2.10K) were observed in the MICU2 KO cells when $[Ca^{2+}]_c$ reached ~500 nM.

Importantly, MCU-mediated Ca^{2+} uptake was greater in cells lacking MICU2 not only between 500 nM – 3 µM, but over the entire range of imposed $[Ca^{2+}]_c$, resulting in a markedly left-shifted curve of the $[Ca^{2+}]_c$-dependence of Ca^{2+} uptake (Figure 2.10H). Notably, however, the slope of the logarithmic plot was similar: 3.1 and 2.5 for WT and MICU2 KO cells, respectively (Figure 2.10I & Table 2.1). Both effects were rescued by re-expression of MICU2 (Figure 2.10H-I

& Table 2.1). These results suggest that MICU2 plays two roles: First, it tunes the threshold for relief of MICU1-mediated gatekeeping in the low-$[Ca^{2+}]_c$ regime. Second, it affects the gain of MCU activation, imposing a brake on the MICU1-mediated increase of MCU activity at higher $[Ca^{2+}]_c$ by decreasing the apparent Ca^{2+} affinity of the activation mechanism without strongly affecting its cooperativity.

Cooperative relief of gatekeeping requires Ca^{2+}-binding to EF-hands of MICU1 and MICU2

The ability of MICU1 and MICU2 to sense $[Ca^{2+}]_c$ and regulate MCU activity has been attributed to the presence of two Ca^{2+}-binding EF-hand domains in each protein. We investigated the roles of each EF hand in gatekeeping and cooperative activation, using expression constructs in which the EF hands were mutated to disrupt Ca^{2+} binding (Perocchi et al., 2010)(Kamer and Mootha, 2014). MICU2 was stably expressed with each MICU1 EF-hand mutant in MICU1 KO cells to ensure similar expression of each protein. MICU1-Flag immunofluorescence confirmed that all cells in clonal populations uniformly expressed the mutant proteins (not shown) and total expression levels were verified by western blotting (Figure 2.11A). Whereas Ca^{2+} stabilizes MICU1-MICU2 heterodimers *in vitro* (Kamer et al., 2017), in our clonal lines each EF-hand mutant formed proper MICU1/2 heterodimers (Figure 2.11A) that remained associated with MCU (Figure 2.11B). Upon inhibition of NCLX-mediated Ca^{2+} extrusion at low $[Ca^{2+}]_c$ (< 300 nM), mitochondrial Ca^{2+} uptake was absent in MICU1-ΔEF1 and MICU1-ΔEF2 cells and very low (< 0.1 ΔnM/sec) in ΔEF1/2 cells (Figure 2.12A-B), indicating that Ca^{2+}-binding to MICU1 EF-hands is not required for gatekeeping. In agreement, resting $[Ca^{2+}]_m$ was unchanged in MICU1-ΔEF1, -ΔEF2 or -ΔEF1/2 cells (Figure 2.11E-F).

When $[Ca^{2+}]_c$ was elevated to levels that overcame gatekeeping in WT cells, Ca^{2+} uptake was remarkably suppressed in all three MICU1 EF-hand mutant-cell lines across the full range of $[Ca^{2+}]_c$ tested, to an extent that no $[Ca^{2+}]_c$ steady state was reached during the subsequent 300 seconds (Figures 2.12C-F). Logarithmic plots showed loss of cooperativity in both individual EF-hand mutants as well as in the double mutant, with linear-fit slopes of 1.8, 1.8 and 1.4

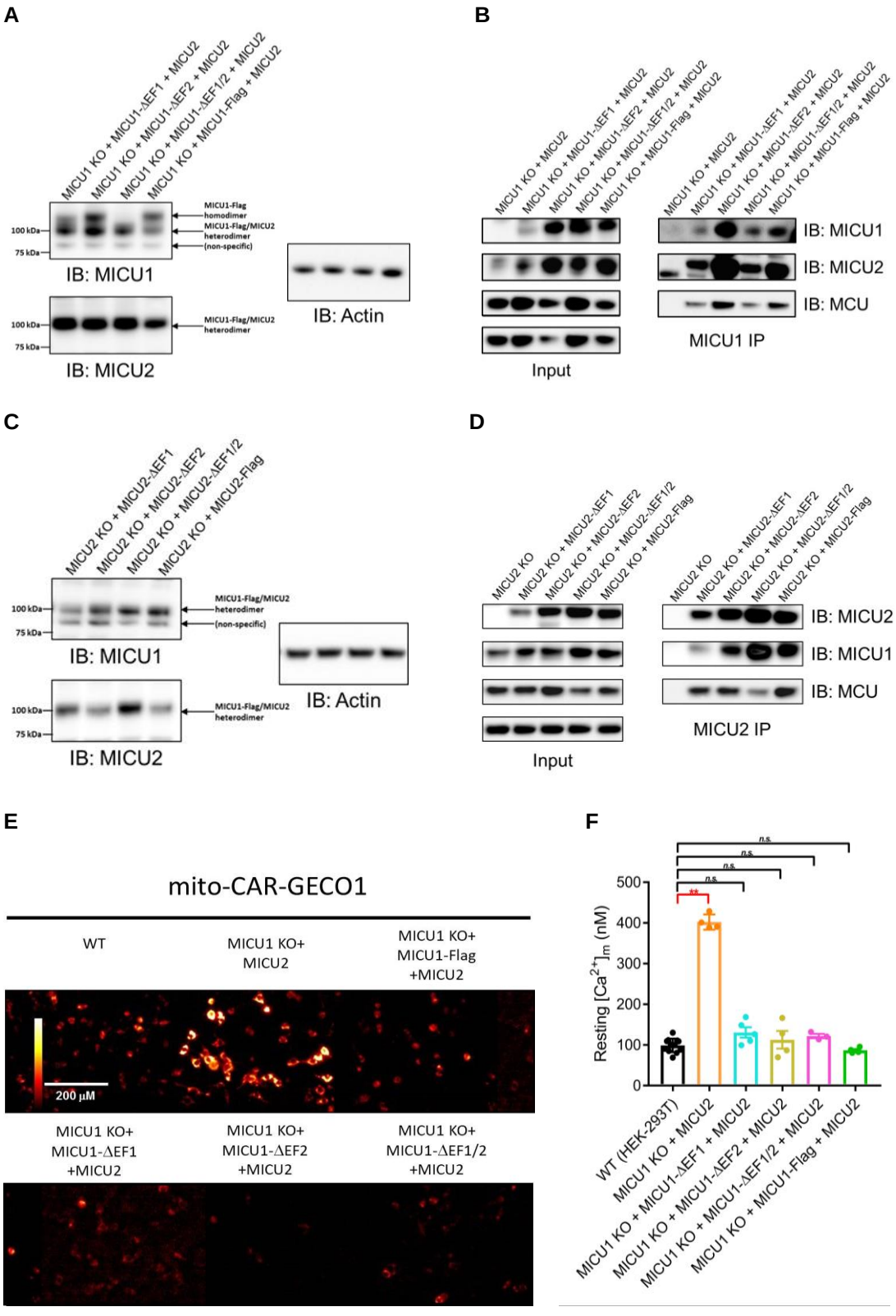
A
MICU1 KO + MICU1-ΔEF1 + MICU2
MICU1 KO + MICU1-ΔEF2 + MICU2
MICU1 KO + MICU1-ΔEF1/2 + MICU2
MICU1 KO + MICU1-Flag + MICU2
MICU1-Flag homodimer
MICU1-Flag/MICU2 heterodimer
(non-specific)
100 kDa
75 kDa
IB: MICU1
IB: Actin
MICU1-Flag/MICU2 heterodimer
IB: MICU2
B
MICU1 KO + MICU2
MICU1 KO + MICU1-ΔEF1 + MICU2
MICU1 KO + MICU1-ΔEF2 + MICU2
MICU1 KO + MICU1-ΔEF1/2 + MICU2
MICU1 KO + MICU1-Flag + MICU2
IB: MICU1
IB: MICU2
IB: MCU
Input
MICU1 IP
C
MICU2 KO + MICU2-ΔEF1
MICU2 KO + MICU2-ΔEF2
MICU2 KO + MICU2-ΔEF1/2
MICU2 KO + MICU2-Flag
MICU1-Flag/MICU2 heterodimer
(non-specific)
100 kDa
75 kDa
IB: MICU1
IB: Actin
MICU1-Flag/MICU2 heterodimer
IB: MICU2
D
MICU2 KO
MICU2 KO + MICU2-ΔEF1
MICU2 KO + MICU2-ΔEF2
MICU2 KO + MICU2-ΔEF1/2
MICU2 KO + MICU2-Flag
IB: MICU2
IB: MICU1
IB: MCU
Input
MICU2 IP
E
mito-CAR-GECO1
WT
MICU1 KO+ MICU2
MICU1 KO+ MICU1-Flag +MICU2
200 μM
MICU1 KO+ MICU1-ΔEF1 +MICU2
MICU1 KO+ MICU1-ΔEF2 +MICU2
MICU1 KO+ MICU1-ΔEF1/2 +MICU2
F
n.s.
n.s.
n.s.
n.s.
**
Resting [Ca2+]m (nM)
500
400
300
200
100
0
WT (HEK-293T)
MICU1 KO + MICU2
MICU1 KO + MICU1-ΔEF1 + MICU2
MICU1 KO + MICU1-ΔEF2 + MICU2
MICU1 KO + MICU1-ΔEF1/2 + MICU2
MICU1 KO + MICU1-Flag + MICU2

Figure 2.11

Figure 2.11. EF-hand mutations in MICU1 or MICU2 do not impair MCU complex assembly or elevate resting $[Ca^{2+}]_m$

(**A**) Western blot of whole-cell lysates for MICU1 (top left) or MICU2 (bottom left) and α-actin (right) from MICU1_KO cells with stable overexpression of [MICU1-ΔEF1+MICU2], [MICU1-ΔEF2+MICU2], [MICU1-ΔEF1/2+MICU2], or [MICU1-Flag+MICU2] (MICU1-rescue) under non-reducing conditions. Bands at ~100 kDa represent disulfide-linked MICU1-Flag/MICU2 heterodimers and bands at >100 kDa represent MICU1-Flag homodimers. Bands at ~90 kDa are due to non-specific binding. (**B**) α-Flag immunoprecipitation from MICU1_KO cells stably-expressing MICU2 and Flag-tagged MICU1, MICU1-ΔEF1, MICU1-ΔEF2, or MICU1-ΔEF1/2. Immunoblots of whole-cell lysates with α-MCU, α-MICU1, and α-MICU2 antibodies shown. Mutations of MICU1 EF hands do not prevent interactions with MICU2 or MCU. (**C**) Non-reducing western blots of MICU2 (top), MICU1 (middle) and actin (bottom) in whole-cell lysates from MICU2_KO cells stably over-expressing MICU2-ΔEF1, MICU2-ΔEF2, MICU2-ΔEF1/2, or MICU2-Flag (MICU2 rescue). Bands at ~100 kDa represent disulfide-linked MICU1-Flag/MICU2 heterodimers. (**D**) α-Flag immunoprecipitation from MICU2_KO cells stably expressing Flag-tagged MICU2, MICU2-ΔEF1, MICU2-ΔEF2, or MICU2-ΔEF1/2. Immunoblots of whole-cell lysates with α-MCU, α-MICU1, and α-MICU2 antibodies shown. Mutations of MICU2 EF hands do not prevent interactions with MICU1 or MCU. (**E**) Basal mito-CAR-GECO1 fluorescence in WT and MICU1_KO HEK-293T cells stably expressing MICU2 alone, MICU1-ΔEF1+MICU2, MICU1-ΔEF2+MICU2, MICU1-ΔEF1/2+MICU2, or MICU1-Flag+MICU2, imaged at 20x magnification. (**F**) Mitochondrial matrix $[Ca^{2+}]$ ($[Ca^{2+}]_m$) in WT (n = 12) and MICU1_KO cells stably expressing MICU2 alone (n =4), MICU1-ΔEF1+MICU2 (n = 5), MICU1-ΔEF2+MICU2 (n =4), MICU1-ΔEF1/2+MICU2 (n = 3), or MICU1-Flag+MICU2 (n = 4), calibrated from mito-CAR-GECO1 fluorescence. Bars represent mean $[Ca^{2+}]_m$ +/- SEM. (*P < 0.05; **P < 0.01; Bonferroni's multiple comparisons test).

respectively (Figure 2.12G & Table 2.1). These results indicate that Ca^{2+}-binding to both EF hands of MICU1 is necessary for full cooperative-activation of MCU in response to elevated $[Ca^{2+}]_c$.

Similar experiments were performed using MICU2 KO cells in which MICU2 expression was rescued with -ΔEF1, -ΔEF2, or -ΔEF1/2 mutants. Expression of each mutant protein was uniform across the cell population, and western blotting showed formation of MICU1/2 heterodimers (Figure 2.11C), and each EF-hand mutant associated with MCU (Figure 2.11D). MCU activity below 300 nM $[Ca^{2+}]_c$ was negligible in MICU2-ΔEF1, -ΔEF2, and -ΔEF1/2 cells (Figure 2.13A-C), indicating that MICU2 EF hands play no role in gatekeeping, consistent with the lack of effect of MICU2 KO on MCU activity in low (< 500 nM) $[Ca^{2+}]_c$. In contrast, mutation of either MICU2 EF hand had striking effects on Ca^{2+} uptake in the higher-$[Ca^{2+}]_c$ regime. Nearly complete inhibition of MCU activity was observed in MICU2-ΔEF1 and -ΔEF1/2 cells even at $[Ca^{2+}]_c$ up to 9 μM (Figure 2.13D-E), and to a lesser extent in cells expressing MICU2-ΔEF2. This implicates MICU2 EF1 as a critical Ca^{2+}-binding site required for relief of gatekeeping. Notably, cooperativity of MCU activation was completely lost in MICU2-ΔEF1 (slope = 1.6) and -ΔEF1/2 (slope = 1.2) cells, and to a lesser but significant extent in MICU2-ΔEF2 cells (slope = 2.0) (Figure 2.13F-G, Table 2.1). Thus, within the context of the physiological MICU1/2 heterodimer, Ca^{2+}

binding to EF hands in both MICU1 and MICU2 is required for cooperative activation of MCU by $[Ca^{2+}]_c$ above the gatekeeping threshold.

	Slope +/- 95% CI (decade/decade)	Uptake rate at 1 μM $[Ca^{2+}]_c$ (nM/sec)	R^2
WT (HEK-293T)	3.1 ± 0.08	0.9	0.99
MICU1 KO	1.4 ± 0.06	14.3	0.99
MICU1 KO+MICU2	1.4 ± 0.04	20.4	0.99
MICU1 KO+MICU1-Flag	2.1 ± 0.07	2.0	0.99
MICU1 KO+MICU1-Flag+MICU2	2.5 ± 0.10	1.6	0.98
MICU2 KO	2.5 ± 0.15	8.7	0.97
MICU2 KO+MICU2-Flag	2.7 ± 0.16	1.7	0.97
MICU1 KO+MICU1-ΔEF1+MICU2	1.8 ± 0.12	0.5	0.97
MICU1_KO+MICU1-ΔEF2+MICU2	1.8 ± 0.09	1.1	0.98
MICU1_KO+MICU1-ΔEF1/2+MICU2	1.4 ± 0.09	1.3	0.95
MICU2 KO+MICU2-ΔEF1	1.6 ± 0.07	0.7	0.99
MICU2 KO+MICU2-ΔEF2	2.0 ± 0.12	2.0	0.98
MICU2 KO+MICU2-ΔEF1/2	1.2 ± 0.09	0.8	0.97
MCU KO	1.4 ± 0.11	0.1	0.97

Table 2.1. Linear regression of $\log_{10}[Ca^{2+}]_c$ vs. $\log_{10} Ca^{2+}$ uptake rate

Slope, uptake rate at 1 μM $[Ca^{2+}]_c$, and R^2 values for linear regression analyses of $\log_{10} Ca^{2+}$-uptake rate vs. $\log_{10}[Ca^{2+}]_c$. Slope ~1 indicates non-cooperative increase in uptake rate while slope > 1 indicates cooperativity in the $[Ca^{2+}]_c$ -dependent relief of MCU gatekeeping.

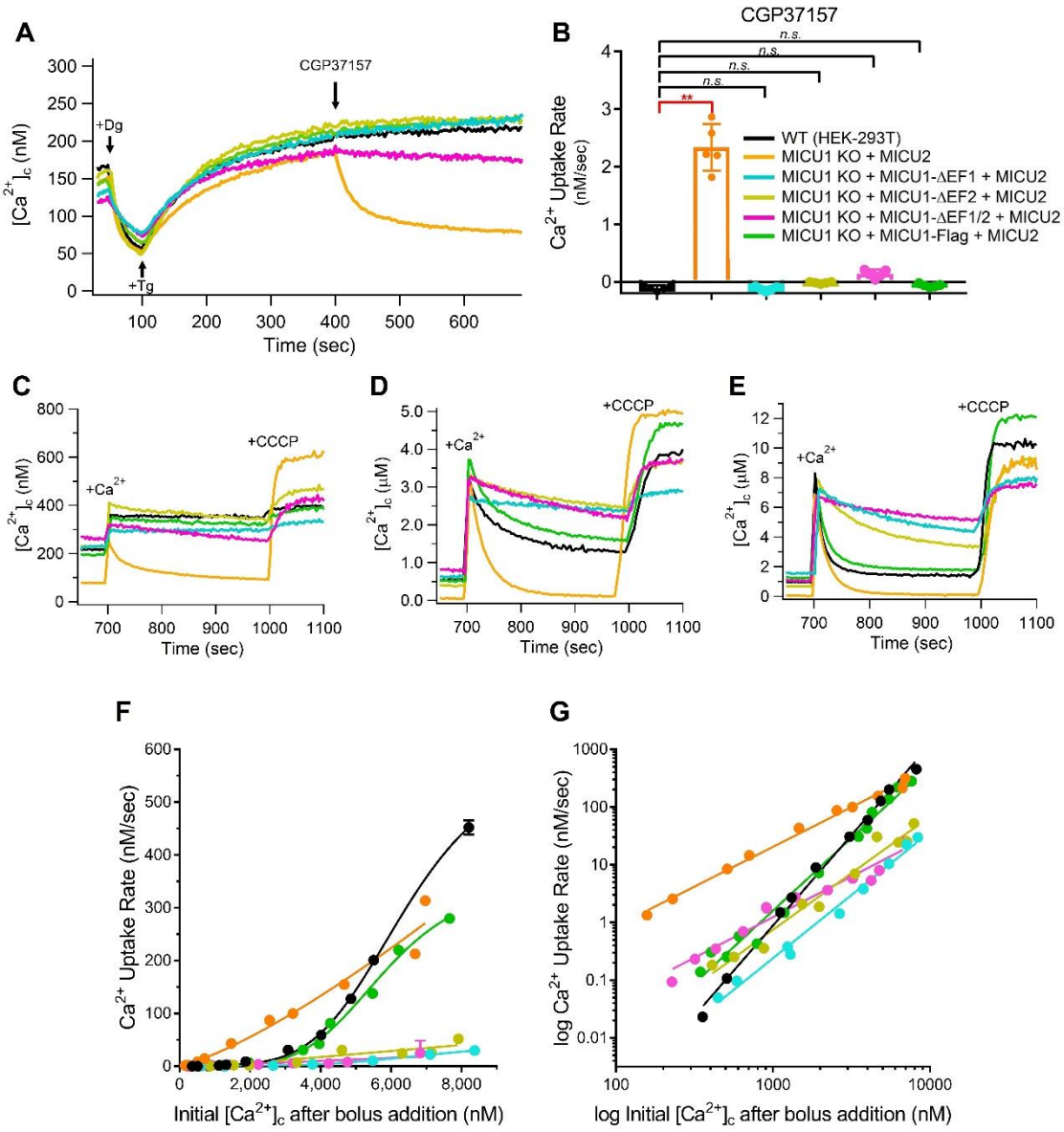

Figure 2.12. Ca^{2+} binding to MICU1 EF hands promotes cooperative activation of MCU

(**A**) Responses to CGP37157 in the low-$[Ca^{2+}]$ regime. Representative traces for each cell line (color coding in B) for n ≥ 5 independent replicates. Like WT, MICU1 EF-hand mutants show negligible Ca^{2+} uptake. (**B**) Quantification of Ca^{2+} uptake rates after inhibition of NCLX-mediated efflux for cells in (A). Each point represents an independent experiment (n = 5 for each condition). Bars: mean +/- SEM. (*P < 0.05; **P < 0.01; n.s, not different; Bonferroni's multiple comparisons test). Mutation of MICU1 EF hands does not affect gatekeeping at $[Ca^{2+}]_c$ < 300 nM. (**C-E**) $[Ca^{2+}]_c$ for cells in (A, B) after bolus additions of Ca^{2+} to increase $[Ca^{2+}]_c$ to 300-400 nM (C), 2.5-4 μM (D), or 7-9 μM (E). Representative traces shown from n ≥ 2 independent replicates for each cell line with similar peak $[Ca^{2+}]_c$ after $CaCl_2$ addition. (**F-G**) Ca^{2+} uptake rate as a function of the peak $[Ca^{2+}]_c$ after acute Ca^{2+} additions. Each point represents an independent experiment. Solid lines: Hill-Equation (F) or linear (G) fits of Ca^{2+}-uptake rate vs. $[Ca^{2+}]_c$

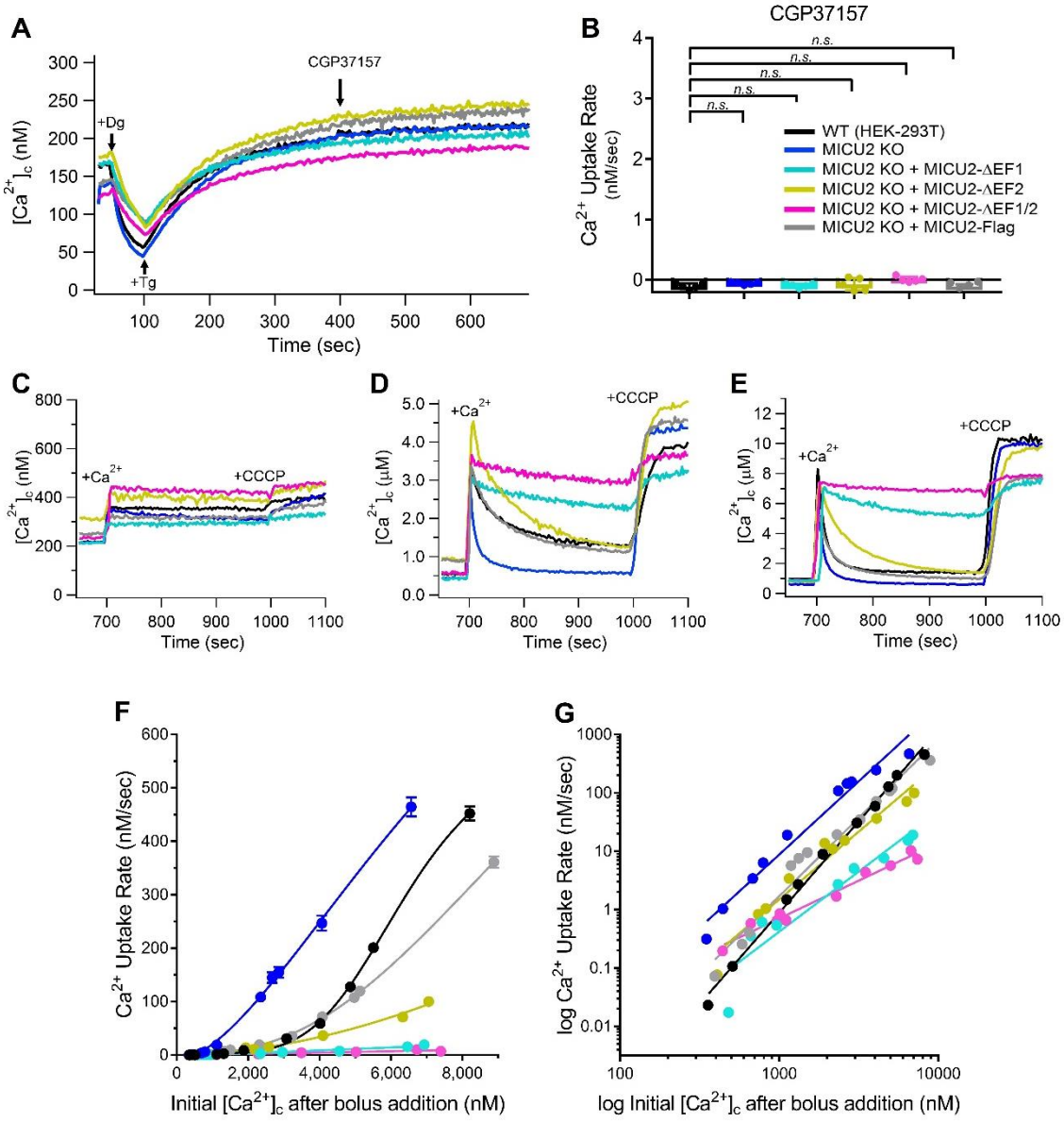

Figure 2.13. Ca^{2+} binding to MICU2 EF hands tunes MICU1-mediated cooperative activation of MCU

(**A**) Responses to CGP37157 in the low-$[Ca^{2+}]$ regime. Representative traces for each cell line (color coding in B) from n ≥ 5 independent replicates. (**B**) Quantification of Ca^{2+}-uptake rates in response to CGP37157 for cells in (A). Each point represents an independent experiment (n = 5 for each condition). Bars: mean +/- SEM. (*P < 0.05; **P < 0.01; n.s, not different; Bonferroni's multiple comparisons test). Absence of MICU2 or mutation of its EF hands does not affect gatekeeping at $[Ca^{2+}]_c$ < 300 nM. (**C-E**) $[Ca^{2+}]_c$ for cells in (A, B) after bolus additions of Ca^{2+} to increase $[Ca^{2+}]_c$ to 300-500 nM (C), 3-4.5 μM (D), or 7-9 μM (E). Representative traces shown from n ≥ 2 independent replicates for each cell line with similar peak $[Ca^{2+}]_c$. (**F-G**) Ca^{2+} uptake rate as function of peak $[Ca^{2+}]_c$ after acute Ca^{2+} additions. Each data point represents an independent experiment. Solid lines: Hill-Equation (F) or linear (G) fits of Ca^{2+}-uptake rate vs. $[Ca^{2+}]_c$ plotted on linear (F) or $\log_{10}$ (G) scales. MICU2 elevates the threshold for MICU1-mediated MCU activation, and Ca^{2+} binding to its EF hands is required for cooperative MCU activation.

CHAPTER 3: The Relative Stoichiometry Between MCU and EMRE *In Vivo*

An important question is whether the cryo-EM MCU-EMRE structure recapitulates the stoichiometry of MCU and EMRE in the functional channel complex *in vivo*. Furthermore, it is unknown whether the same or different numbers of EMRE subunits are required for MCU activity on the one hand, and normal MICU1/2-mediated gatekeeping and cooperative activation on the other. It has been demonstrated that EMRE (but not MCU) is rapidly turned-over by degradation through the activity of IMM-associated matrix-AAA (mAAA) proteases (Tsai et al., 2017)(König et al., 2016). Such rapid turnover could result in variable relative steady-state expression levels of EMRE and MCU that could alter the stoichiometry in cells. If MCU requires four EMRE for its activity, then absence of a single EMRE subunit from the complex would lead to complete loss of channel activity. On the other hand, if fewer than four EMRE subunits per MCU tetramer are sufficient for activity but fail to properly tether MICU1/2 dimers to the complex, such channels may be functional but exhibit altered gatekeeping and cooperative-activation profiles.

We have devised a two-pronged approach to address these questions and to determine the consequences of altering the number of EMRE subunits in each complex on both channel activity and regulation by MICU1/2. First, we engineered model systems to manipulate the relative MCU and EMRE protein expression ratios in cells and correlate them with functional features. Second, we created a series of MCU-EMRE concatemers with multiple concatenated MCU subunits fused to EMRE in order to “fix” the relative stoichiometry between EMRE and MCU in each channel complex. These approaches enabled functional and biochemical comparison of channels with a range of EMRE:MCU stoichiometries to endogenous channel complexes. Our results suggest that MCU largely exists in association with fewer than 4 and more than 1 EMRE subunit.

Materials and methods:

Generation of the MCU/EMRE double-knockout (MEKO) cell line

HEK-293T cells with genetic deletion of *EMRE* (EMRE KO cells) were a generous gift from Dr. Vamsi Mootha. Both genomic copies of *MCU* were inactivated in EMRE KO cells using CRISPR/Cas9-mediated gene editing. sgRNAs targeting the 5' end of the *MCU* coding sequence were chosen using MIT CRISPR design tool (http://crispr.mit.edu). Two guides were chosen to target Exon 1 (guides 1 and 2) and two for Exon 2 (guides 3 and 4).

Guide 1 (5'-3'):

(Forward) CAGGAGCGATCTACCTGCGG

(Reverse) CCGCAGGTAGATCGCTCCTG

Guide 2 (5'-3'):

(Forward) CAGCAGGAGCGATCTACCTG

(Reverse) CAGGTAGATCGCTCCTGCTG

Guide 3 (5'-3'):

(Forward) TGACAGCGTTCACGCCGGGA

(Reverse) TCCCGGCGTGAACGCTGTCA

Guide 4 (5'-3'):

(Forward) TGAACTGACAGCGTTCACGC

(Reverse) GCGTGAACGCTGTCAGTTCA

Oligonucleotides were annealed, treated with T4 polynucleotide kinase at 37°C for 30 min, 95°C for 5 min, and ramped from 95-25°C (5°C/min), and ligated into the pSPCas92A-GFP vector (Addgene, 48138) that had been digested with BbsI (NEB) and treated with Calf Alkaline Phosphatase (NEB). Ligation reactions were used to transform Turbo Competent *E. coli* (NEB), individual clones were isolated and the presence of each sgRNA was verified by sequencing. Maxi prep DNA for each sgRNA pair was used to transfect EMRE KO (HEK-293T) cells growing in DMEM containing 10% fetal bovine serum (HyClone) and 1x anti-biotic/anti-mycotic (Gibco) at 37˚C and 5% CO_2. One week after transfection GFP-positive cells were isolated at the expression

using flow cytometry (Wistar Institute) and clones were grown to confluence in 10 cm dishes. Loss of MCU expression in each clone was verified by western blot and genomic sequencing.

Cell lines and cDNA expression constructs

All HEK-293T cell lines were grown in DMEM containing 5-10% fetal bovine serum (HyClone) and 1x anti-biotic/anti-mycotic (complete medium) at 37˚C and 5% CO_2. EMRE KO (HEK-293T) cells were a generous gift from Dr. Vamsi Mootha. cDNAs of full-length V5-tagged EMRE and Flag-tagged MICU1 in pCMV6-A-BSD and pCMV6-A-Puro vectors were obtained from Origene. MCU-V5-(6x)His cDNA in pDEST40 was purchased from Addgene and subcloned into pCMV6-A-BSD and pCMV6-A-Puro using standard molecular biology techniques. EMRE [P76I] cDNA in pCMV6-A-BSD and pCMV6-A-Puro was generated using a PCR-based site-directed mutagenesis strategy. The MCU-EMRE concatemer described by Tsai et al. (2016) (+/- the EMRE [P76I]) mutation in pCMV6-A-BSD and pCMV6-A-Puro were created using a PCR-based cloning strategy. Fusion proteins with additional MCU subunits fused to EMRE were synthesized and sequence-verified by Bio Basic Inc. and subcloned into pCMV6-A-Puro. Each additional MCU subunit added to the MCU-EMRE concatemer was encoded by a unique cDNA sequence to ensure stability of the construct and facilitate full-length sequencing (see Supplementary Experimental Procedures). Stable cell lines were created by transfection with Transit LT1 (Mirus) as per manufacturer's protocol and maintained in complete medium with 5 µg/mL blasticidin and/or 2 µg/mL puromycin until stable expression of each plasmid was achieved. Clones were isolated by limiting dilution for each condition and maintained in complete medium with antibiotics.

Simultaneous determination of mitochondrial Ca^{2+} uptake and $\Delta\Psi_m$ in permeabilized cells

Concurrent measurement of mitochondrial Ca^{2+} uptake and IMM potential ($\Delta\Psi_m$) in permeabilized HEK-293T cells was performed as described in Chapter 2 (Payne et al., 2017), with fluorescence measurements calibrated to represent bath (cytoplasmic) [Ca^{2+}] and relative

$\Delta\Psi_m$ (normalized to response in the presence of CCCP). For determination of the gatekeeping $[Ca^{2+}]_c$ threshold, the calculated $[Ca^{2+}]_c$ 300 sec after challenge with 0.1 - 10 µM Ca^{2+} (Y) was plotted as a function of the (peak) initial $[Ca^{2+}]_c$ achieved after bolus Ca^{2+} addition (X). Data were fitted using a one-phase association model where (Y_0) is the Y value when X is zero, (P) is the plateau, or Y value at infinite X, and (K) is the rate constant, expressed in reciprocal of the X axis.

$$Y = Y_0 + (P - Y_0)\left(1 - e^{(-KX)}\right)$$

The value of (P) represents to the steady-state $[Ca^{2+}]_c$ at which gatekeeping is re-established +/- the standard error of (P) determined from the fit.

SDS-PAGE western blotting

For western blotting of whole-cell lysates, cells grown in in 150 mm plates were washed with DPBS, detached with Versene solution (0.48 mM EDTA in DPBS) and lysed with buffer containing (in mM): 50 Tris-HCl (pH 7.4), 150 NaCl, 0.05 EGTA, and 0.3 $CaCl_2$ with 0.2% (w/v) n-Dodecyl β-D-maltoside. Immediately prior to use, lysis buffer was supplemented with 1 mM PMSF and protease inhibitor cocktail (cOmplete, Roche). For western blots of mitochondrial proteins, mitochondria were isolated as previously described (Sancak et al., 2013). Total protein concentrations were calculated using BCA Protein Assay kit (Pierce), and samples for PAGE were prepared in 2x Laemmli sample buffer (Bio-Rad, 1610737) +/- 2-Mercaptoethanol (βME) (Bio-Rad, 1610710). NuPAGE© gels (4-12%) were transferred to Immobilon© P PVDF membranes and probed with various antibodies. Antibodies used were anti-MCU (Cell Signaling Technologies, 14997S), anti-V5 tag (Cell Signaling Technologies, 13202S), anti-MICU2 (Abcam, ab101465), anti-DYKDDDDK (Flag tag) (Cell Signaling Technologies, 14793S), anti-β-Tubulin (Invitrogen, 32-2600), and anti-Hsp60 (Abcam, ab46798). Membranes were blocked in 5% fat-free milk for 1 hr at RT, incubated overnight at 4°C with primary antibody, and then for 1 hr at RT with anti-rabbit IgG-HRP (Cell Signaling Technologies, 7074S) or anti-mouse IgG-HRP (Cell Signaling Technologies, 7076S) secondary antibodies conjugated to horseradish peroxidase

(HRP). Chemiluminescence detection was carried out using SuperSignal West Chemiluminescent Substrate (Thermo). The mean pixel density of bands was quantified using ImageJ (NIH), corrected for the intensity of the loading-control band (β-tubulin for whole-cell lysates or Hsp60 for isolated mitochondria), and normalized to the response in WT cells. For EMRE:MCU ratio calculations, the mean pixel density of the EMRE-V5 band was divided by the mean pixel density of the MCU-V5 band for each independent experiment. Predicted stoichiometry histograms were derived from the binomial probability equation where (n) is the number of possible combinations of EMRE and MCU that can assemble, (r) is the EMRE:MCU expression ratio determined from V5 western blot band intensities, and (x) is the number of EMRE subunits per channel.

$$P(x) = \frac{(n!)(r^x)((1-r)^{(n-x)})}{(x!)((n-x)!)}$$

P(x) is the probability of obtaining (x) EMRE subunits per channel based on the EMRE:MCU expression ratio given random association of the two proteins.

Immunofluorescence microscopy of mitochondrial proteins

Clear, 12-well tissue culture-treated plates (CytoOne, CC7682-7524) were seeded with 2×10^5 cells/well on 12 mm glass coverslips in 500 µL/well of complete medium. Cells were grown for 24 hr prior to fixation in 1 mL of 4% (v/v) paraformaldehyde (Electron Microscopy Sciences, 15713-S) in complete medium. Cells were fixed for 15 min at 37°C, washed with DPBS, and permeabilized in 1 mL/well of 0.1% (v/v) Triton X-100 detergent (Sigma-Aldrich) for 30 min at RT. Permeabilization solution was decanted and 2 mL of (2x) casein blocking buffer (Sigma-Aldrich, B6429) was added to each well and incubated for 30 min at RT. Blocking solution was removed and replaced with 1 mL/well of rabbit anti-V5 antibody (Cell Signaling Technology, 13202S) and mouse anti-Flag M2 (Sigma-Aldrich, F3165) primary antibodies each diluted 1:2,000 in (1x) blocking buffer and incubated overnight at 4°C with gentle agitation. The following day plates were removed from 4°C, washed with 0.05% (v/v) Tween-20 (Bio-Rad, 1706531) in DPBS, and 1 mL/well of anti-rabbit IgG Alexa Fluor 568-conjugated (Invitrogen, A-11011) and anti-mouse IgG

Alexa Fluor 488-conjugated (Invitrogen, A-11001) secondary antibodies each diluted 1:2,000 in (1x) blocking buffer was added to each well and incubated in the dark for 1 hr at RT. Coverslips from each well were mounted on standard glass slides using VECTASHIELD® Antifade Mounting Medium with DAPI (Vector Laboratories, H-1200) and images were collected on a Leica TCS SP8 X system using a 100x/1.4 NA PL APO CS2 objective. Labeled V5-tagged proteins (MCU-EMRE concatemers) were excited using a continuously tunable white light laser set to 568 nm to detect fluorescence emission between 600-700 nm. Labeled Flag-tagged proteins (MICU1-Flag) were excited at 488 nm to detect fluorescence emission between 510-550 nm. DAPI was excited at 408 nm to detect fluorescence emission between 430-470 nm.

In-cell ELISA to quantify V5 expression

Clear, 96-well tissue culture-treated plates (Corning, 3603) were seeded with 2.5×10^4 cells/well in 100 µL of complete medium. Each cell line was seeded in eight replicate wells across three replicate plates. Cells were grown for 24 hr then fixed, permeabilized and blocked as described above (200 µL/well). Blocking solution was removed and replaced with 100 µL/well of mouse anti-V5 antibody (Invitrogen, R960-25) diluted in (1x) blocking buffer and incubated overnight at 4°C with gentle agitation. The following primary antibody dilutions were tested in triplicate wells: 1:1,000; 1:5,000, 1:25,000; 1:125,000; 1:250,000. One well for each cell line was reserved for the no primary antibody control. The following day plates were removed from 4°C, washed as described above, and 100 µL/well of anti-mouse IgG HRP-linked secondary antibody (Cell Signaling Technology, 7076S) diluted 1:2,000 in (1x) blocking buffer was added to each well and incubated for 1 hr at RT with gentle agitation. Secondary antibody was decanted, plates were washed as previously described, and 100 µL/well of 1-Step™ Ultra TMB - ELISA Substrate solution (Thermo, 34028B) was added to each well and incubated for 10 min at RT. Absorbance at 650 nm of each well was measured in a Cytation 5 plate reader; three sequential measurements of each plate were made to ensure that the HRP reaction has reached completion. After reading, the substrate was removed and 50 µL of 0.3% (w/v) Janus Green B

(Sigma-Aldrich, 201677) dye solution was added to each well as a control for cell density and plates were incubated for 5 min at RT. The dye was decanted, plates were washed with diH_2O to remove excess solution and 200 µL of 0.5 N HCl solution was added to each well. Absorbance at 595 nm was measured in the Cytation 5 plate reader as previously described. The ELISA signal (Abs @ 650 nm) for each well was normalized for cell density (Abs @ 595 nm) the mean normalized response for cell line was plotted as a function of the primary antibody dilution. Data were fitted using a one site-total binding model where (Y) is the mean normalized ELISA response, (B_{max}) is the relative total number of V5-binding sites, (X) is the primary antibody dilution factor, (K_D) is the dissociation constant, (NS) represents the contribution of non-specific binding of the secondary antibody, and (Y_0) is the background signal of the detector.

$$Y = \left[\frac{(B_{max})(X)}{K_D + X}\right] + (NS)(X) + Y_0$$

BN-PAGE western blotting

Total protein concentrations of isolated mitochondrial preparations were determined using BCA Protein Assay kit (Pierce). 5 µg total protein of each sample for PAGE were prepared in 4x NativePage sample buffer (Invitrogen, BN2003) supplemented with 5% Digitonin. NativePAGE© gels (4-12%) were either stained with Coomassie blue protein stain (as a loading control and to detect NativeMark™ Unstained Protein Standard (Invitrogen)) or transferred to Immobilon© P PVDF membranes, fixed in 8% acetic acid, and probed with anti-MCU (Cell Signaling Technologies, 14997S) and anti-DYKDDDDK (Flag tag) (Cell Signaling Technologies, 14793S) antibodies. Membranes were blocked in 5% fat-free milk for 1 hr at RT, incubated overnight at 4°C with primary antibody, and then for 1 hr at RT with anti-rabbit IgG-HRP (Cell Signaling Technologies, 7074S) secondary antibody conjugated to horseradish peroxidase. Chemiluminescence detection was carried out as described above.

Determination of molecular weights for MCU-EMRE concatemers and native channels

Calibration of molecular weight was performed by plotting the peak intensity of each band of known molecular weight (X) from the marker as a function of the relative vertical position (Y) of each band on gels stained with Coomassie blue, and data were fitted using an exponential growth equation where (Y_0) is the Y value when X is zero and (K) is the rate constant, expressed in reciprocal of the X axis :

$$Y = Y_0 \times e^{kX}$$

Pixel intensity for each lane in the MCU western blots sample was determined as previously described using ImageJ, and molecular weights from n = 3 independent experiments were interpolated from the fit above.

Statistical analyses

Independent, normally-distributed rate measurements and steady states after uptake were analyzed using ordinary one-way ANOVA and Tukey's multiple comparisons t-test to identify significant differences between all each cell line and all others. Normalized western blot band intensities were analyzed using ordinary one-way ANOVA and Dunnett's multiple comparisons t-test to identify differences in expression relative to WT cells, or Welch's unpaired t-test for pairwise comparisons between cell types other than WT. Molecular weight measurements from BN-PAGE western blots were analyzed using repeated measures one-way ANOVA and Dunnett's multiple comparisons t-test to identify differences relative to WT channel complexes. All statistical tests were performed using GraphPad Prism 7.0. P-values < 0.05(*); < 0.01(**); < 0.001(***); and < 0.0001(****) were considered statistically significant.

Results:

Restoration of EMRE and MCU expression in MCU/EMRE double-KO cells

To create a system in which relative MCU and EMRE protein expression levels could be directly measured and correlated with functional outcomes, we first created a cell line in which all genomic copies of both *MCU* and *EMRE* were inactivated. This was accomplished by CRISPR/Cas9-mediated genetic knockout of *MCU* in HEK-293T cells in which all *EMRE* genes had already been inactivated (provided by Vamsi Mootha), hereafter referred to as MEKO cells. Inactivating mutations in the *EMRE* and *MCU* genes were verified by genomic sequencing. Western blotting revealed a complete loss of MCU protein expression (Figure 3.1A-B: red). We previously showed that MICU2 dimerizes with MICU1 under non-reducing conditions, but does not form homodimers when overexpressed in MICU1 KO cells (Payne et al., 2017). Thus, bands

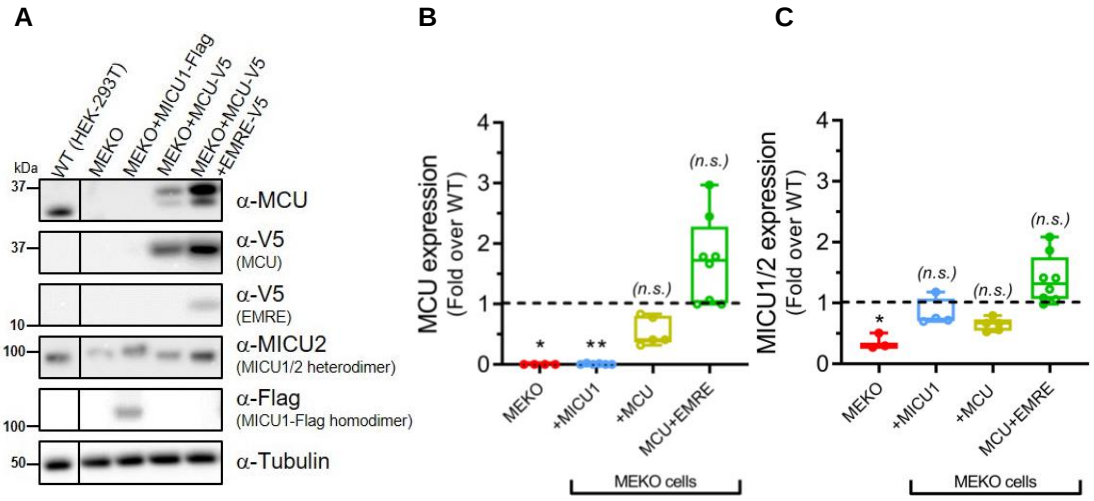

Figure 3.1. MCU and MICU1/2-dimer expression in stable cell lines relative to WT

(A) Western blots of MCU, V5-tag, MICU2, Flag-tag, and β-tubulin from whole-cell lysates of WT (HEK-293T) cells, or MCU/EMRE KO (MEKO) cells +/- stable expression of MICU1-Flag, MCU-V5, or MCU-V5 and EMRE-V5. Two bands for MCU-V5 protein are due to low-level degradation of the V5-tag. MICU2- and Flag-blots performed under non-reducing conditions, such that MICU2 bands represent MICU1/2 heterodimers and Flag bands represent MICU1-Flag homo-dimers. **(B)** Quantification of MCU western blot band intensity for cell lines in (A) from $n \geq 4$ independent experiments. Mean pixel density corrected for β-tubulin intensity and normalized to endogenous MCU band intensity in WT cells for each experiment. Replicate measurements shown as hollow circles, boxes denote the 25^{th}-75^{th} percentile with line at median, error bars represent range of all measurements. P-values: pairwise comparisons of each cell line with WT cells (*P < 0.05; **P < 0.01; ***P < 0.001; ****P < 0.0001; n.s., not different; Dunnett's multiple comparisons test). **(C)** Quantification of MICU2 western blot band intensity for cell lines in (A) from $n \geq 4$ independent experiments under non-reducing conditions to preserve MICU1/2 heterodimers, quantified as described in (B). Replicate measurements shown as hollow circles, boxes denote the 25^{th}-75^{th} percentile with line at median, error bars represent range of all measurements. P-values: pairwise comparisons of each cell line with WT cells (*P < 0.05; **P < 0.01; ***P < 0.001; ****P < 0.0001; n.s., not different; Dunnett's multiple comparisons test).

at ~100 kDa observed in non-reducing western blots for MICU2 correspond to MICU1/2 heterodimers. MEKO cells exhibited reduced expression of MICU1/2 dimers relative to WT cells (Figure 3.1A&C: red), which increased upon stable overexpression of MICU1-Flag (MEKO+MICU1 cells) to levels equivalent to those in WT cells (Figure 3.1A&C: blue). Similarly, stable transfection of MEKO cells with MCU-V5 (MEKO+MCU cells) restored both MCU and MICU1/2 dimer expression to WT levels (Figure 3.1A-C: yellow). Stable expression of EMRE-V5 in MEKO+MCU cells (MCU+EMRE cells) did not change MCU or MICU1/2-dimer expression relative to WT cells (Figure 3.1A-C: green). All EMRE expressed in these stable lines was fully processed to its mature form (Figure 3.2A). Notably, EMRE expression was ~10-fold lower than MCU in MCU+EMRE cells (Figure 3.2B). Given this EMRE:MCU ratio, binomial probability predicts that > 98% of MCU tetramers would associate with zero, one, or two EMRE proteins (Figure 3.2C). The lack of available antibodies specific to the processed form of endogenous EMRE in the IMM prevented a comparison of EMRE levels between the WT and MCU+EMRE

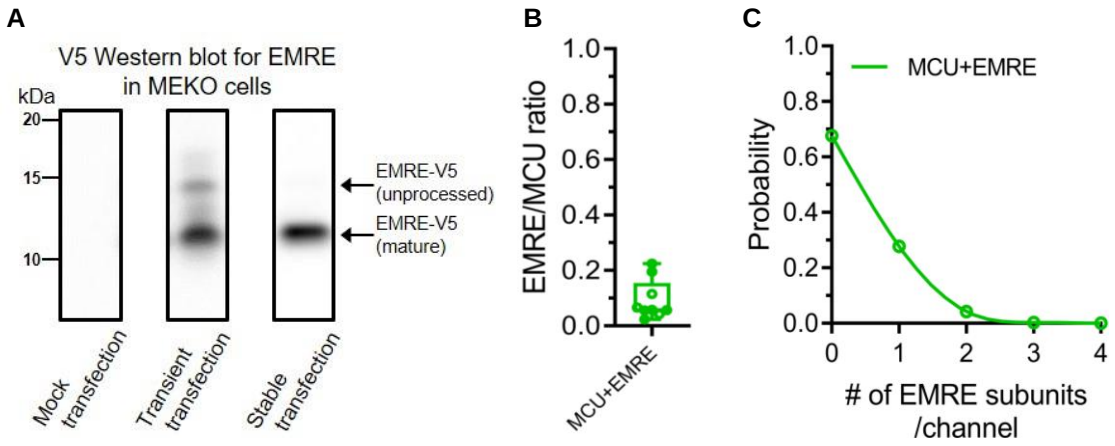

Figure 3.2. The low EMRE:MCU ratio in MCU+EMRE cells predicts formation of channels with 1 or 2 EMRE subunits

(**A**) V5 western blots from whole-cell lysates of MEKO cells with no transfection, transient transfection, or stable transfection of EMRE-V5. Bands shown are from different blots; each result is representative of n $\geq$ 4 biological replicates and n $\geq$ 3 technical replicates for each condition. Transient expression of EMRE-V5 results in bands corresponding to both the unprocessed (~14 kDa) and mature (~11 kDa) forms of EMRE while cells with stable expression show only the mature form of EMRE. (**B**) Quantification of the EMRE:MCU expression ratio in MCU+EMRE cells from V5 western-blot band intensity (n = 9 independent experiments). Ratio calculated by dividing the mean pixel density of EMRE-V5 band by that of the MCU-V5 band for each experiment. Replicate measurements shown as hollow circles, boxes denote 25th-75th percentile with line at median, and error bars represent range of all measurements. The EMRE:MCU expression ratio in MCU+EMRE cells is 0.09 +/- 0.07 (mean +/- SD). (**C**) Probability-distribution histogram of number of EMRE subunits per MCU channel in MCU+EMRE cells based on mean EMRE:MCU expression ratio calculated in (B). Points represent mean probability of obtaining 0, 1, 2, 3, or 4 EMRE subunits per channel based on binomial distribution. Solid lines: spline fits of all data points. At this EMRE:MCU expression ratio, > 98% of channels are predicted to associate with 0, 1 or 2 EMRE subunits.

cells. Consequently, whereas expression levels of MCU and MICU1/2 in MCU+EMRE cells were similar to those observed in WT cells, we do not know if the relative expression of MCU to EMRE in the MCU+EMRE cells was similar to that in WT cells.

To evaluate MCU function, we simultaneously measured MCU-mediated Ca^{2+} uptake and relative mitochondrial membrane potential ($\Delta\Psi_m$) in permeabilized cells as previously described using the cell-impermeant Ca^{2+}-indicator dye Fura-FF (K_D = 5.5 µM) (Mallilankaraman et al., 2012b)(Payne et al., 2017) and tetramethylrhodamine ethyl ester (TMRE), respectively (9). Digitonin (Dg) was added to a suspension of cells to permeabilize the plasma membrane but leave the IMM intact (Figure 3.3A: t = 50 sec). Sequestration of TMRE by energized mitochondria quenches its fluorescence, which reached a steady state following cell permeabilization (Figure 3.3B). Thapsigargin (Tg) was added to inhibit the Sarco/Endoplasmic Reticular Calcium ATPase (SERCA), preventing Ca^{2+} uptake into the ER and releasing the ER Ca^{2+} stores into the bath solution (Figure 3.3A: t = 100 – 400 sec). Next, CGP37157 (CGP), an inhibitor of mitochondrial Na^+/Ca^{2+}-antiporter (NCLX)-mediated Ca^{2+} efflux, was added to isolate MCU as the only pathway for transport of Ca^{2+} between mitochondria and cytoplasm (Figure 3.3A: t = 400 – 700 sec). Upon

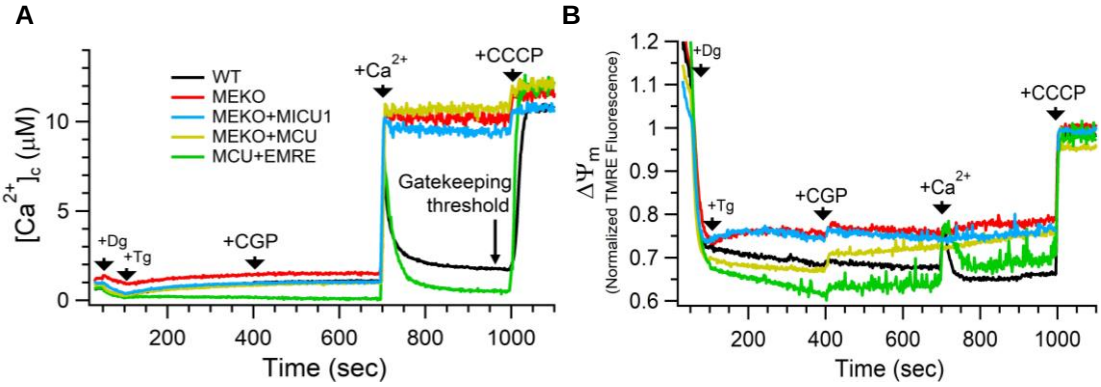

Figure 3.3. MCU channel activity requires expression of both MCU and EMRE

(**A**) Cytoplasmic (bath) $[Ca^{2+}]$ ($[Ca^{2+}]_c$) of cell lines in (A) measured with Fura-FF (K_D = 5.5 µM). Cells were treated with 0.004% digitonin (Dg) to permeabilize plasma membrane, 2 µM thapsigargin (Tg) to inhibit SERCA and prevent ER Ca^{2+} uptake, and 20 µM CGP37157 (CGP) to block mitochondrial Ca^{2+} efflux through NCLX, added at t = 50, 100 and 400 sec, respectively, as indicated. A bolus addition of free-Ca^{2+} sufficient to raise $[Ca^{2+}]_c$ to 8-10 µM added at t = 700 sec to stimulate Ca^{2+}-uptake through MCU, and 2 µM CCCP added at t = 1000 sec to uncouple $\Delta\Psi_m$ and release mitochondrial Ca^{2+} content. Representative traces from n $\geq$ 3 independent replicates for each cell line shown. Both MCU and EMRE are required for Ca^{2+} uptake activity. (**B**) Relative $\Delta\Psi_m$ for experiments shown in (A) measured using 1 µM TMRE. Sequestration of the dye by energized mitochondria leads to quenching of its fluorescence, which increases upon depolarization. Transient depolarization is observed in response to Ca^{2+} uptake, while addition of 2 µM CCCP led to a sustained loss of $\Delta\Psi_m$.

reaching a steady-state $[Ca^{2+}]_c$ following CGP treatment, acute addition of a Ca^{2+} bolus to the bath solution (i.e. cytoplasm) immediately elevated the $[Ca^{2+}]_c$ to 8-10 µM, which was followed by clearance of Ca^{2+} in WT cells that reduced $[Ca^{2+}]_c$ to a steady-state level between 1-2 µM over the subsequent 300 seconds (Figure 3.3A: t = 700 – 1000 sec; black trace). A transient increase in TMRE fluorescence was observed (Figure 3.3B) as Ca^{2+} influx into the matrix depolarized $\Delta\Psi_m$, which then recovered within 50-100 seconds as $[Ca^{2+}]_c$ approached a steady state due to closure of MCU. This steady state represents the $[Ca^{2+}]_c$ threshold at which uptake ceases, one of the hallmarks of MICU1/2-mediated MCU gatekeeping. Finally, the mitochondrial uncoupler carbonyl cyanide m-chlorophenyl hydrazone (CCCP) was added to dissipate $\Delta\Psi_m$ (Figure 3.3B), leading to a rapid increase in $[Ca^{2+}]_c$ as the total mitochondrial matrix Ca^{2+} content was released (Figure 3.3A: t = 1000 – 1100 sec). The TMRE fluorescence in CCCP was used to determine the relative $\Delta\Psi_m$ between experiments.

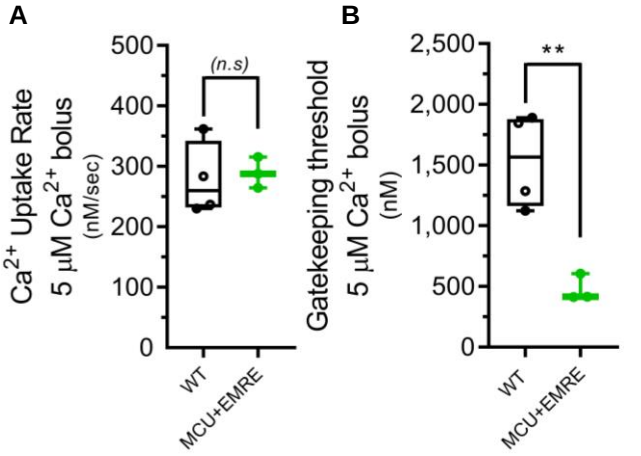

Figure 3.4. MCU+EMRE cells show similar uptake rates to WT cells but a reduced steady-state $[Ca^{2+}]_c$ at which uptake ceases

(**A**) Ca^{2+}-uptake rates for WT and MCU+EMRE cells in response to bolus additions of $CaCl_2$ that increase $[Ca^{2+}]_c$ by ~5 µM from n ≥ 3 independent experiments. Replicate measurements shown as hollow circles, boxes denote the 25th-75th percentile with line at median, error bars represent range of all measurements. P-values: pairwise comparison of MCU+EMRE with WT cells (n.s., not different; Welch's unpaired t-test). Ca^{2+} uptake rates were not different between WT and MCU+EMRE cells. (**B**) Steady-state $[Ca^{2+}]_c$ for cell lines in (A) measured 300 sec after bolus addition of ~5 µM free-Ca^{2+}. Each point (hollow circle) represents an independent experiment (n ≥ 3 for each condition). P-values: comparison of MCU+EMRE with WT cells (**P < 0.01; Welch's unpaired t-test). The gatekeeping ($[Ca^{2+}]_c$) threshold after uptake in MCU+EMRE cells was reduced (~500 nM) relative to WT levels (1.5-2 µM).

Upon challenge with boluses of free Ca^{2+} that increased $[Ca^{2+}]_c$ to ~10 µM, permeabilized MEKO cells exhibited no reduction in $[Ca^{2+}]_c$ (Figure 3.3A: red trace) or change in $\Delta\Psi_m$ (Figure 3.3B: red trace), reflecting a lack of mitochondrial Ca^{2+} uptake, as expected. MEKO+MICU1 cells (Figure 3.3A-B: blue traces) or MEKO+MCU cells (Figure 3.3A-B: yellow traces) also exhibited no MCU activity, in agreement with previous findings that EMRE is required for MCU channel activity (Sancak et al.,

2013)(Kovács-Bogdán et al., 2014)(Yamamoto et al., 2016). In contrast, MCU+EMRE cells (Figure 3.3A-B; Figure 3.4A: green) exhibited mitochondrial Ca^{2+} uptake rates and transient depolarizations at $[Ca^{2+}]_c$ of 8-10 µM similar to WT cells (Figure 3.3A-B; Figure 3.4A: black). Surprisingly, whereas the steady-state $[Ca^{2+}]_c$ achieved 200-300 sec after uptake ceased was ~1.5-2 µM in WT cells (Figure 3.4B: black), it was reduced to ~500 nM in MCU+EMRE cells (Figure 3.4B: green). Reduction to levels lower than those achieved in WT cells is a feature of impaired gatekeeping (Mallilankaraman et al., 2012b)(Csordás et al., 2013)(Kamer and Mootha, 2014)(Payne et al., 2017)(Patron et al., 2014)(Kamer et al., 2017). To test this further, we measured MCU activity at low (100-600 nM) $[Ca^{2+}]_c$ using the high-affinity indicator Fura-2 (K_D = 140 nM) following CGP addition. As discussed in Chapter 2, CGP was required because NCLX-mediated mitochondrial Ca^{2+} efflux can mask MCU-mediated influx even in the absence of MICU1/2-mediated gatekeeping (Figure 2.3). Acute CGP addition (t = 400 sec) was without effect on $[Ca^{2+}]_c$ in WT cells (Figure 3.5A-B: black) due to MICU1/2 gatekeeping. A reduction in $[Ca^{2+}]_c$

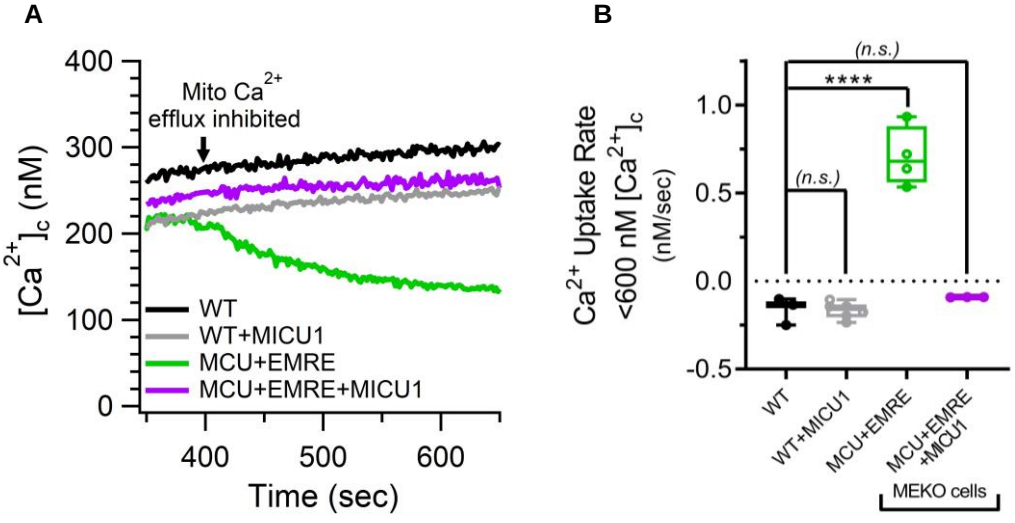

Figure 3.5. MCU+EMRE cells exhibit constitutive Ca^{2+} uptake in the low $[Ca^{2+}]_c$ regime

(**A**) $[Ca^{2+}]_c$ response to acute inhibition of NCLX-mediated Ca^{2+}-efflux for WT (black), WT+MICU1 (gray), MCU+EMRE (green), and MCU+EMRE+MICU1 (purple) cells measured with the high-affinity indicator Fura-2. Representative traces from n ≥ 3 independent replicates for each cell line shown. Overexpression of MICU1-Flag in MCU+EMRE cells rescued gatekeeping at low (< 300 nM) $[Ca^{2+}]_c$. (**B**) Quantification of mitochondrial Ca^{2+}-uptake rate below 600 nM $[Ca^{2+}]_c$ in response to inhibition of NCLX-mediated Ca^{2+} efflux for cell lines in (A). Each point represents initial Ca^{2+}-uptake rate from an independent experiment (n ≥ 3 for each condition) determined by single-exponential fit to reduction of $[Ca^{2+}]_c$. Replicate measurements shown as hollow circles, boxes: the 25th-75th percentile with line at median, error bars: range of all measurements. P-values: pairwise comparisons of each cell line with WT cells (*P < 0.05; **P < 0.01; ***P < 0.001; ****P < 0.0001; n.s., not different; Tukey's multiple comparisons test).

following acute addition of CGP, reflecting constitutive MCU activity, was observed in MICU1 KO cells (Figure 2.3B: red trace), as expected due to lack of gatekeeping (Mallilankaraman et al., 2012b)(Csordás et al., 2013)(Kamer and Mootha, 2014)(Payne et al., 2017)(Patron et al., 2014). Notably, MCU+EMRE cells exhibited significant constitutive Ca^{2+} uptake (Figure 3.5A-B: green), confirming a lack of fully-functional MICU1/2-mediated gatekeeping. MICU1/2 also mediate cooperative activation of MCU in response to higher $[Ca^{2+}]_c$ (Csordás et al., 2013)(Payne et al., 2017). Determination of the Ca^{2+}-uptake rates in response to acute additions of Ca^{2+} between 0.1 - 10 µM, plotted on a log/log scale, yielded a slope of ~2.8 in WT cells (Figure 3.6A&C: black), as previously observed (Payne et al., 2017). In contrast, the slope was ~1.6 in MCU+EMRE

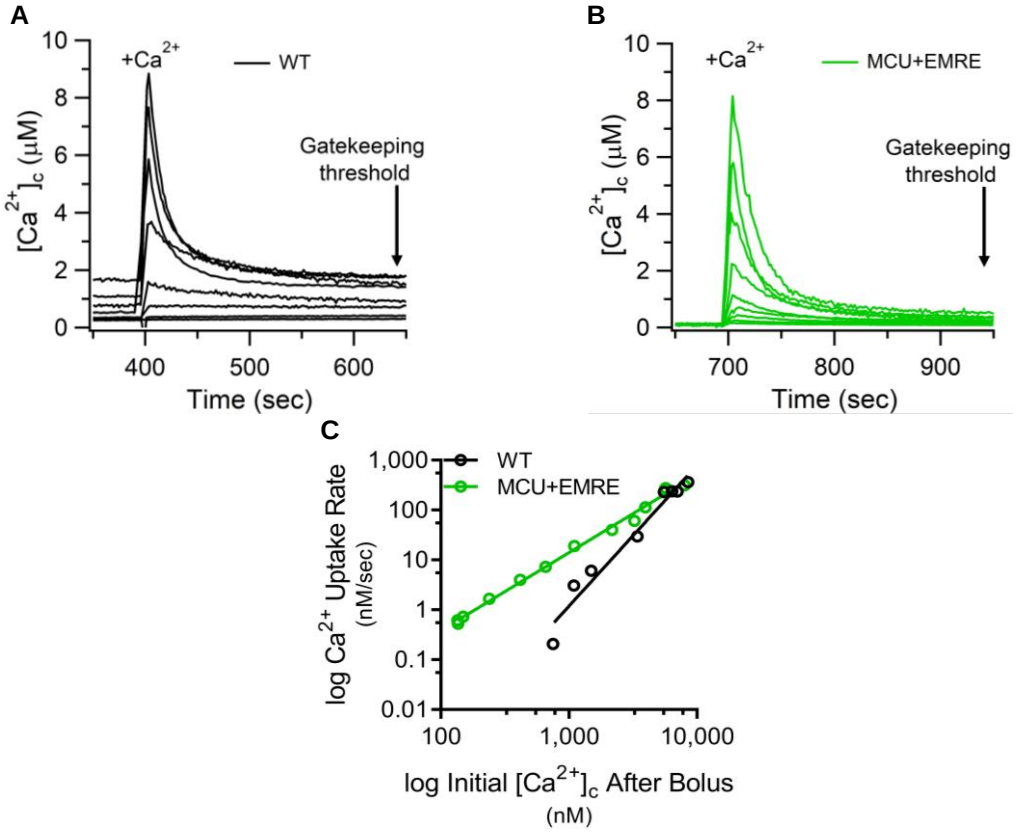

Figure 3.6. MCU+EMRE cells show an apparent loss of cooperative activation due to lack of gatekeeping

(**A-B**) Mitochondrial Ca^{2+}-uptake in suspensions of permeabilized WT (A) and MCU+EMRE (B) cells in response to acute increases of $[Ca^{2+}]_c$ to between 0.1 - 10 µM. Individual representative traces from independent experiments with different bolus additions shown. (**C**) Ca^{2+}-uptake rates for WT and MCU+EMRE cells in response to acute challenge with $[Ca^{2+}]_c$ between 0.1 - 10 µM as a function of the $[Ca^{2+}]_c$ immediately after bolus addition plotted on a log_{10}/log_{10} scale. Each point (hollow circle) represents an independent experiment. Solid lines: linear fits of Ca^{2+}-uptake rate vs. $[Ca^{2+}]_c$ to demonstrate cooperativity of MCU activation and highlight differences in Ca^{2+}-uptake rates at low (< 1 µM) $[Ca^{2+}]_c$. Slope of the best-fit line is related to the cooperativity of the transition of MCU from the closed to the open state, which is reduced in MCU+EMRE cells (slope = 1.6) relative to WT cells (slope = 2.8).

cells, suggesting reduced cooperativity (Figure 3.6B-C: green). However, this apparent loss of cooperative activation was due solely to constitutive channel activity at low (< 1-2 μM) $[Ca^{2+}]_c$, and not a loss of cooperative activation at higher $[Ca^{2+}]_c$ as seen in MICU1 KO cells. Thus, gatekeeping and cooperative activation of MCU were uncoupled in MCU+EMRE cells, a novel phenomenon not previously seen in cells lacking MICU1 and/or MICU2 expression (Csordás et al., 2013)(Payne et al., 2017).

Overexpression of MICU1 only partially restores gatekeeping in MCU+EMRE cells

Although MICU1/2-dimer expression in MCU+EMRE cells was similar to that in WT cells (Figure 3.1A&C), we considered that because of the low EMRE:MCU expression ratio in these cells, gatekeeping was disturbed because most channels lacked enough EMRE to tether sufficient MICU1/2 dimers to the channels. Because MICU1 can directly associate with MCU (Paillard et al., 2018)(Phillips et al., 2019), we reasoned that over-expression of MICU1 in MCU-EMRE cells could restore gatekeeping despite low EMRE expression by directly interacting with MCU. To test this, MICU1-Flag was stably expressed in MCU+EMRE cells (MCU+EMRE+MICU1 cells) and in WT cells (WT+MICU1 cells). The expression level of MCU (Figure 3.7A-B) and the EMRE:MCU expression ratio (Figure 3.7C-D) were similar in MCU+EMRE+MICU1 and MCU+EMRE cells. MICU1-Flag homodimers were present in the MICU1-overexpressing cells (Figure 3.7E), because of its high expression relative to MICU1 in WT cells (Figure 3.7F). Nevertheless, MICU1/2 dimer expression in MCU+EMRE+MICU1 cells (Figure 3.7G-H: purple) was not different from WT, although a small reduction was observed relative to MCU+EMRE cells (Figure 3.7G-H: green). In contrast, it was increased 2-3-fold in the WT+MICU1 cells compared to WT (Figure 3.7G-H: gray).

We measured MCU activity at low (100-600 nM) $[Ca^{2+}]_c$ as described above. As expected, acute CGP addition was without effect on $[Ca^{2+}]_c$ in WT+MICU1 cells (Figure 3.5A-B: gray) due to MICU1/2 gatekeeping. Whereas the MCU+EMRE cells exhibited significant constitutive Ca^{2+} uptake (Figure 3.5A-B: green), gatekeeping at low $[Ca^{2+}]_c$ was restored in

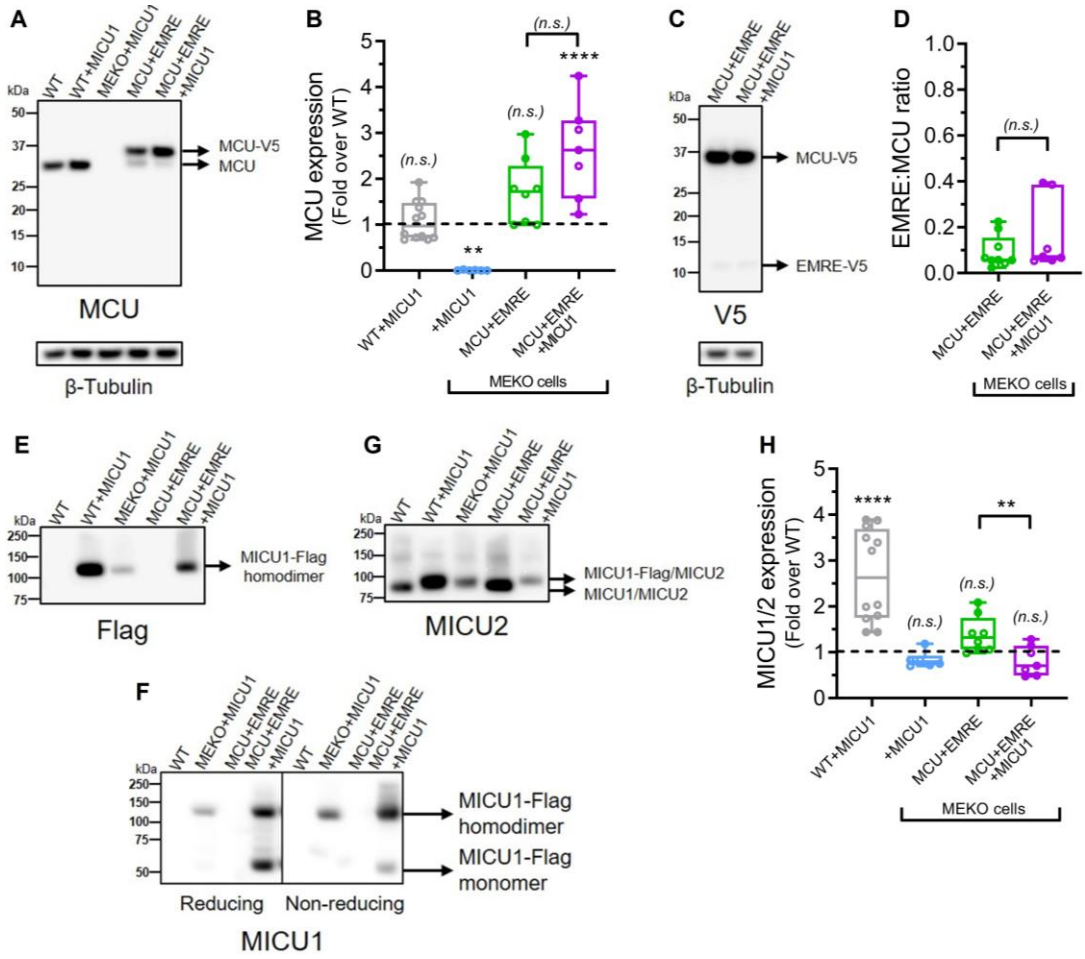

Figure 3.7. MCU, MICU1/2-heterodimer, and MICU1-Flag homodimer expression in stable cell lines

(**A**) Western blot for MCU and β-tubulin from whole-cell lysates of WT, WT+MICU1, MEKO+MICU1, MCU+EMRE and MCU+EMRE+MICU1 cells under reducing conditions. (**B**) Quantification of MCU western blot band intensity for cell lines in (A) ($n \geq 6$ independent experiments). Mean pixel density corrected for β-tubulin intensity and normalized to endogenous MCU band intensity in WT cells for each experiment. Replicate measurements shown as hollow circles, boxes: the 25th-75th percentile with line at median, error bars: range of all measurements. P-values above each box: pairwise comparisons of each cell line with WT cells (**P < 0.01; ****P < 0.0001; n.s., not different; Dunnett's multiple comparisons test) and p-value above green and purple bars: pairwise comparison of MCU+EMRE and MCU+EMRE+MICU1 cells (unpaired t test with Welch's correction). (**C**) Western blot for V5 and β-tubulin from whole-cell lysates of MCU+EMRE and MCU+EMRE+MICU1 cells under reducing conditions. EMRE-V5 is evident as a dim band at ~11 kDa while dark bands at ~35 kDa represent MCU-V5. (**D**) Quantification of the EMRE:MCU expression ratio for cells in (C) from V5 western blot band intensity ($n \geq 7$ independent experiments). Replicate measurements shown as hollow circles, boxes: 25th-75th percentile with line at median, error bars: range of all measurements. P-value: comparison of MCU+EMRE and MCU+EMRE+MICU1 cells (n.s., not different; unpaired t test with Welch's correction). (**E**) Western blot for Flag (MICU1) for cell lines in (B) under non-reducing conditions to preserve MICU1 homodimers (~110 kDa). (**F**) Western blot for MICU1 in mitochondria isolated from WT, MEKO+MICU1, MCU+EMRE and MCU+EMRE+MICU1 cells under reducing (left) and non-reducing conditions to preserve MICU1 homodimers (~110 kDa) (right). Expression of MICU1-Flag exceeds that of endogenous MICU1. (**G**) Western blot for MICU2 for cell lines in (A) under non-reducing conditions to preserve MICU1/2 heterodimers. The increase in molecular weight from 90 kDa to 100 kDa with MICU1-Flag expression is due to MICU1-Flag/MICU2 heterodimers. (**H**) Quantification of MICU2 western blot band intensity for cell lines in (A) ($n \geq 6$ independent experiments) as described in (B). Replicate measurements shown as hollow circles, boxes: 25th-75th percentile with line at median, error bars: range of all measurements. P-values above each box: pairwise comparisons of each cell line with WT cells (**P < 0.01; ****P < 0.0001; n.s., not different; Dunnett's multiple comparisons test) and p-value above green and purple bars: pairwise comparison of MCU+EMRE and MCU+EMRE+MICU1 cells (unpaired t test with Welch's correction).

MCU+EMRE+MICU1 cells (Figure 3.5A-B: purple). This result suggests that gatekeeping can be reconstituted by EMRE-independent association of MICU1 with MCU. Ca^{2+}-uptake rates in response to Ca^{2+} boluses that elevated $[Ca^{2+}]_c$ by ~5 µM were not different between WT (Figure 3.6A), WT+MICU1 (Figure 3.8A), MCU+EMRE (Figure 3.5B) and MCU+EMRE+MICU1 (Figure 3.8B) cells (Figure 3.8D). There was an apparent increase in cooperative channel activation in

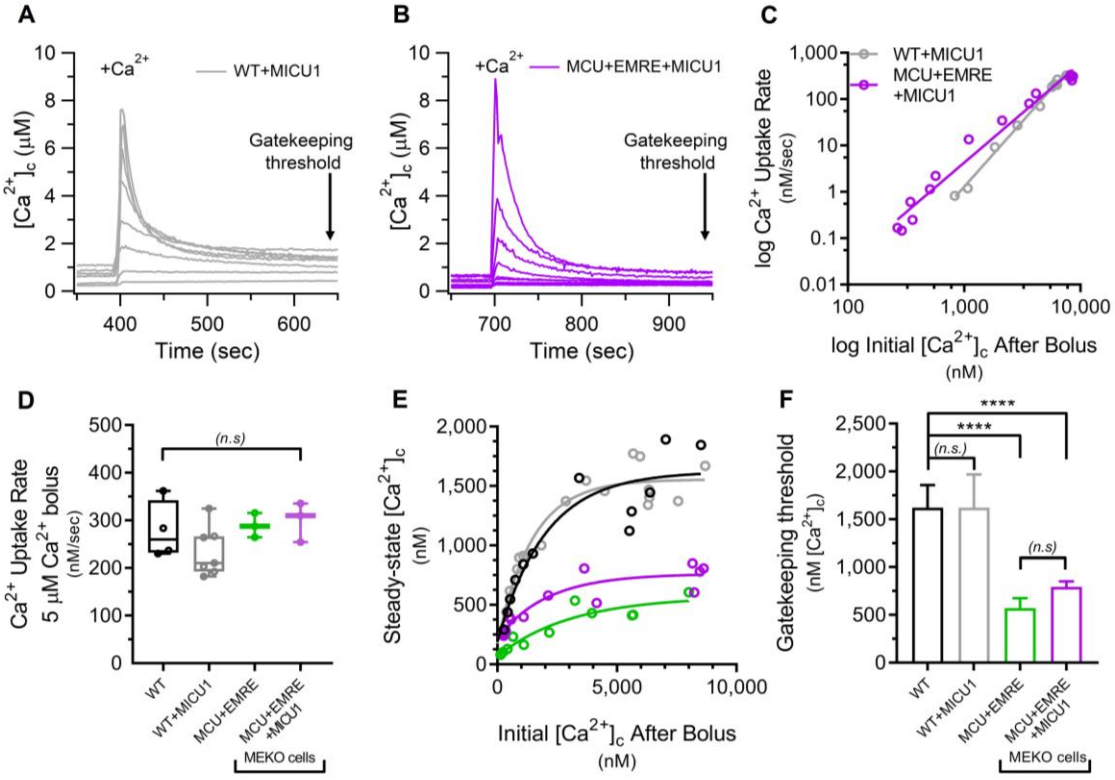

Figure 3.8. Gatekeeping is only partially restored in MCU+EMRE+MICU1 cells

(**A-B**) Mitochondrial Ca^{2+}-uptake in suspensions of permeabilized WT+MICU1 (A) and MCU+EMRE+MICU1 (B) cells in response to acute increases of $[Ca^{2+}]_c$ to between 0.1 - 10 µM. Individual representative traces from independent experiments with different bolus additions shown. (**C**) Ca^{2+}-uptake rates for WT+MICU1 and MCU+EMRE+MICU1 cells in response to acute challenge with $[Ca^{2+}]_c$ between 0.1 - 10 µM as a function of the $[Ca^{2+}]_c$ immediately after bolus addition plotted on log_{10}/log_{10} scale. Each point (hollow circle) represents an independent experiment. Solid lines: linear fits of Ca^{2+}-uptake rate vs. $[Ca^{2+}]_c$. Cooperativity of MCU activation is identical between WT and WT+MICU1 cells (slope = 2.8), while MCU+EMRE+MICU1 cells show increased cooperativity (slope = 2.1) relative to MCU+EMRE cells (slope = 1.6). (**D**) Ca^{2+}-uptake rates for WT, WT+MICU1, MCU+EMRE, and MCU+EMRE+MICU1 cells in response to bolus additions of $CaCl_2$ that increase $[Ca^{2+}]_c$ by ~5 µM ($n \geq 3$ independent experiments). Replicate measurements shown as hollow circles, boxes: the 25^{th}-75^{th} percentile with line at median, error bars: range of all measurements. P-values: pairwise comparison of each cell line with all other cell lines (*P < 0.05; **P < 0.01; ***P < 0.001; ****P < 0.0001; n.s., not different; Tukey's multiple comparisons test). Ca^2 -uptake rates were similar between all cell lines shown. (**E**) Steady-state $[Ca^{2+}]_c$ for cell lines in (D) measured 300 sec after bolus addition of 0.1 - 10 µM Ca^{2+} plotted as function of the initial peak $[Ca^{2+}]_c$ achieved immediately after addition. Each point (hollow circle) represents an independent experiment ($n \geq 12$ for each condition). Solid lines: one-phase association fits of steady-state $[Ca^{2+}]_c$ vs. the initial $[Ca^{2+}]_c$ after addition. (**F**) Comparison of gatekeeping-threshold $[Ca^{2+}]_c$ from non-linear fits in (E). Bars: mean of the plateau parameter for each fit +/- SEM. P-values: comparison of each cell line with all other cell lines (*P < 0.05; **P < 0.01; ***P < 0.001; ****P < 0.0001; n.s., not different; Tukey's multiple comparisons test).

MCU+EMRE+MICU1 cells (slope ~2.1) (Figure 3.8C: purple) relative to MCU+EMRE cells (slope ~1.6) (Figure 3.6C: green), but this could be attributed solely to the restoration of gatekeeping at low $[Ca^{2+}]_c$. Cooperativity of MCU activation was similar between the WT (Figure 3.6C: black) and WT+MICU1 (Figure 3.8C: gray) cells (slope ~2.8 for both). The normal threshold $[Ca^{2+}]_c$ for MCU activation was observed in WT and WT-MICU1 cells (~1.5 μM – Figure 3.8E-F), despite enhanced expression of MICU1 and 2. In contrast, the threshold in MCU+EMRE+MICU1 cells was ~800 nM (Figure 3.8E-F: purple), still below that observed in WT cells. Thus, whereas MICU1 overexpression restored gatekeeping at low $[Ca^{2+}]_c$ in MCU+EMRE cells, presumably by directly interacting with MCU, it was insufficient to fully restore normal gatekeeping. We hypothesized that the low EMRE:MCU ratio in MCU+EMRE+MICU1 cells resulted in sub-stoichiometric association of EMRE with MCU that enabled channel gating but was insufficient to tether enough MICU1/2 dimers to reconstitute fully-functional gatekeeping.

Increasing EMRE expression enhances MICU1/2-mediated gatekeeping

To test this hypothesis, we increased the EMRE:MCU ratio by enhancing steady-state EMRE expression. Under normal conditions, mitochondrial proteins AFG3L2 and SPG7 assemble in the matrix and comprise mAAA proteases that degrade EMRE in the IMM (Tsai et al., 2017)(König et al., 2016). Substitution of a proline (P) residue with isoleucine (I) at amino acid position 76 in EMRE inhibits its degradation, increasing its expression without affecting channel function or gatekeeping (Tsai et al., 2017) (Figure 3.9A-B). We stably overexpressed C-terminal V5-tagged P76I-EMRE and MCU along with MICU1-Flag (to ensure sufficient MICU1 expression to occupy all functional EMRE:MCU complexes) in the MEKO background (MCU+P76I-EMRE+MICU1 cells) and assessed expression levels of various components of the channel complex by western blot. EMRE expression was increased ~6-fold in MCU+P76I-EMRE+MICU1 cells compared with MCU+EMRE+MICU1 cells (Figure 3.10A-B), whereas expression of MCU (Figure 3.10C-D) and MICU1/2 (Figure 3.10E-F) were similar between the two lines. Assuming random assembly of MCU/EMRE complexes, > 95% of MCU tetramers are predicted to associate

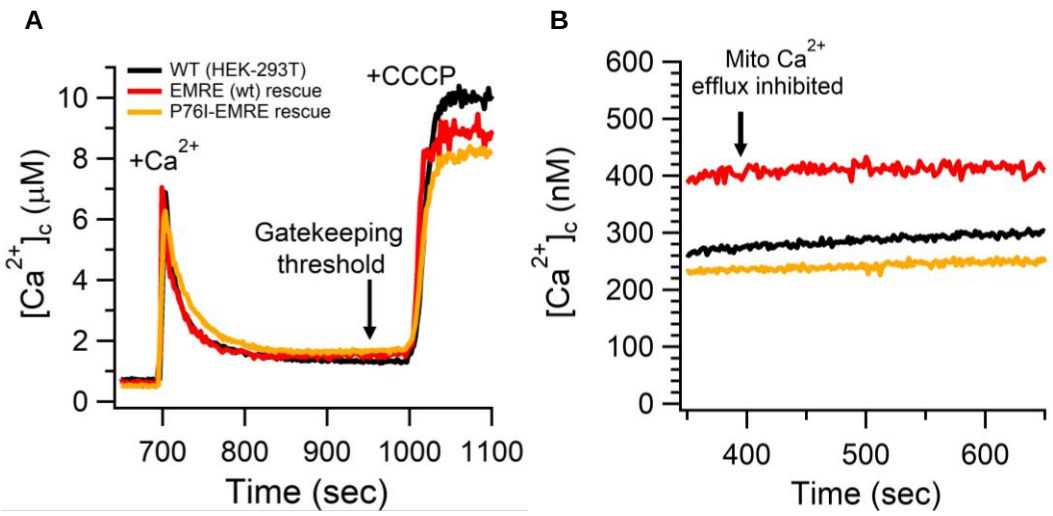

Figure 3.9. The EMRE [P76I] mutation does not affect MCU channel function or gatekeeping

(**A**) Mitochondrial Ca^{2+}-uptake in suspensions of permeabilized WT (black trace) or EMRE KO cells stably expressing either EMRE-V5 (red trace) or P76I-EMRE-V5 (orange trace) in response to acute 5 μM increases of $[Ca^{2+}]_c$. Traces are representative of n ≥ 3 independent experiments. (**B**) $[Ca^{2+}]_c$ response to acute addition of CGP37157 to inhibit NCLX-mediated Ca^{2+} efflux for cell lines in (A) measured with the high-affinity indicator Fura-2. No uptake below 500 nM $[Ca^{2+}]_c$ observed in any of the cell lines tested.

with three or four EMRE subunits in these cells (Figure 3.10G: orange), in contrast to the one or two in the cells expressing WT EMRE (MCU+EMRE+MICU1 cells – Figure 3.10G: purple).

In the low-$[Ca^{2+}]_c$ regime, no differences in Ca^{2+} uptake were observed between WT, WT+MICU1, MCU+EMRE+MICU1 and MCU+P76I-EMRE+MICU1 cells (Figure 3.11A), indicating that MICU1/2-mediated gatekeeping at low $[Ca^{2+}]_c$ was intact. In the higher-$[Ca^{2+}]_c$ regime (8-10 μM), the rate of Ca^{2+} uptake (Figure 3.11B-C) and cooperative activation (Figure 3.11B&D) were similar in MCU+EMRE+MICU1 and MCU+P76I-EMRE+MICU1 cells. Importantly, the steady-state $[Ca^{2+}]_c$ achieved after uptake was significantly higher (~1.8 μM) than in MCU+EMRE+MICU1 cells (~800 nM) (Figure 3.11E-F). These results indicate that increasing the EMRE:MCU ratio elevates the $[Ca^{2+}]_c$ threshold required for relief of MICU1/2-mediated gatekeeping. Together, the data imply that MCU can associate with fewer than 4 EMRE molecules per channel, which is sufficient to reconstitute channel activity and cooperative channel activation but insufficient to fully reconstitute MICU1/2-mediated channel gatekeeping. These results suggest that MCU activity can be differentially modulated by the number of EMRE subunits associated with the channel

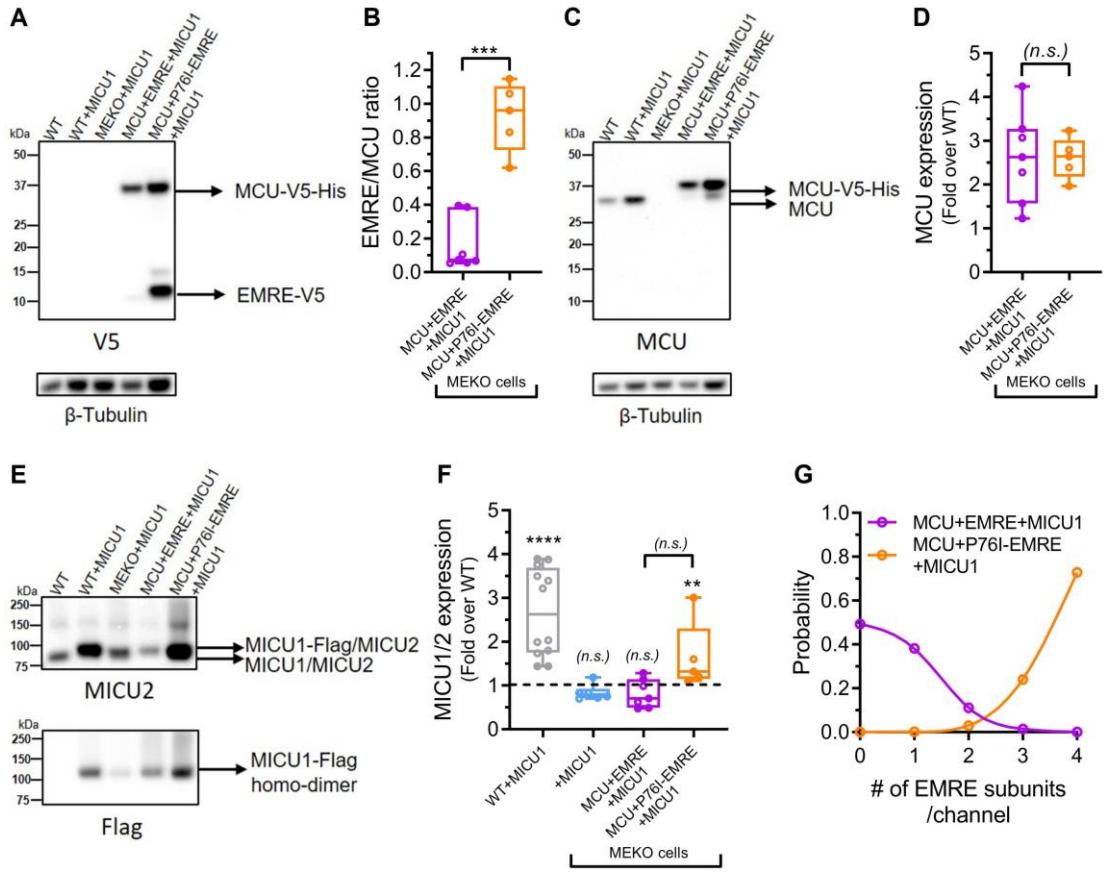

Figure 3.10. The EMRE mutation [P76I] stabilizes EMRE expression

(**A**) Western blot for V5 and β-tubulin from whole-cell lysates of WT, WT+MICU1, MEKO+MICU1, MCU+EMRE+MICU1 MCU+P76I-EMRE+MICU1 cells under reducing conditions. (**B**) Quantification of EMRE:MCU expression ratio from V5 western-blot band intensity for whole-cell lysates of MCU+EMRE+MICU1 and MCU+P76I-EMRE+MICU1 cells (n ≥ 5 independent experiments). Ratio calculated by dividing mean pixel density of EMRE-V5 band by mean pixel density of MCU-V5 band for each experiment. Replicate measurements shown as hollow circles, boxes: 25th-75th percentile with line at median, error bars: range of all measurements. P-value: comparison of MCU+EMRE+MICU1 cells with MCU+P76I-EMRE+MICU1 cells (*P < 0.05; **P < 0.01; ***P < 0.001; ****P < 0.0001; n.s., not different; unpaired t test with Welch's correction). The EMRE:MCU expression ratio in MCU+P76I-EMRE+MICU1 cells is 0.92 +/- 0.21 (Mean +/- SD). (**C**) Western blot for MCU and β-tubulin from whole-cell lysates of cell lines in (A) under reducing conditions. (**D**) Quantification of MCU western-blot band intensity for cells in (B) (n ≥ 5 independent experiments). Mean pixel density corrected for β-tubulin intensity and normalized to endogenous MCU band intensity in WT cells for each experiment. Replicate measurements shown as hollow circles, boxes: 25th-75th percentile with line at median, error bars: range of all measurements. P-value: comparison of MCU+EMRE+MICU1 cells with MCU+P76I-EMRE+MICU1 cells (*P < 0.05; **P < 0.01; ***P < 0.001; ****P < 0.0001; n.s., not different; unpaired t test with Welch's correction). (**E**) Western blot for MICU2 (top) and Flag (MICU1 - bottom) from whole-cell lysates of cell lines in (A) under non-reducing conditions. (**F**) Quantification of MICU2 western blot band intensity from (E) (n ≥ 5 independent experiments). Mean pixel density corrected for β-tubulin intensity and normalized to endogenous MICU2 band intensity in WT cells for each experiment. Replicate measurements shown as hollow circles, boxes: 25th-75th percentile with line at median, error bars: range of all measurements. P-values above each box: comparison of each cell line with WT cells (*P < 0.05; **P < 0.01; ***P < 0.001; ****P < 0.0001; n.s., not different; Dunnett's multiple comparisons test) and p-value above line spanning green and purple bars: pairwise comparison of MCU+EMRE+MICU1 and MCU+P76I-EMRE+MICU1 cells (unpaired t test with Welch's correction). (**G**) Probability-distribution histogram of the expected number of EMRE subunits per MCU channel in MCU+EMRE+MICU1 and MCU+P76I-EMRE+MICU1 cells based on mean EMRE:MCU expression ratios calculated in (B). Points represent mean probability of obtaining 0, 1, 2, 3, or 4 EMRE subunits per channel based on binomial distribution. Solid lines: spline fits of all data points. EMRE:MCU expression ratio in MCU+P76I-EMRE+MICU1 cells predicts that > 95% of MCU tetramers associate with 3 or 4 EMRE subunits.

complex, likely by determining the number of MICU1/2-dimers associated with it. Accordingly, a 4 EMRE:1 channel stoichiometry may not be fixed in cells.

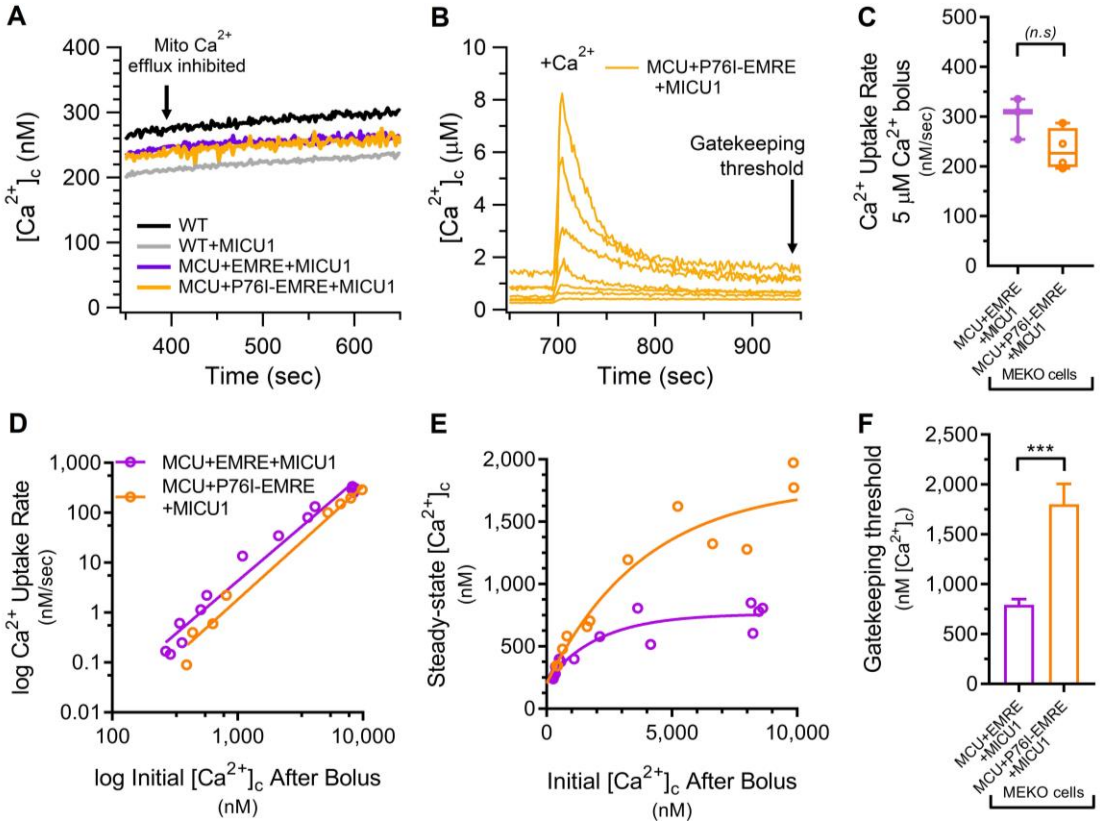

Figure 3.11. Increasing EMRE expression enhances MICU1/2-mediated gatekeeping

(**A**) $[Ca^{2+}]_c$ response to acute inhibition of NCLX-mediated Ca^{2+}-efflux for WT, WT+MICU1, MCU+EMRE+MICU1 and MCU+P76I-EMRE+MICU1 cells measured with the high-affinity indicator Fura-2. Representative traces from n $\geq$ 3 independent replicates for each cell line shown. (**B**) Mitochondrial Ca^{2+} uptake in suspensions of permeabilized MCU+P76I-EMRE+MICU1 cells in response to acute increases of $[Ca^{2+}]_c$ to between 0.1 - 10 µM. Individual traces from independent experiments with series of bolus additions shown. The gatekeeping threshold in MCU+P76I-EMRE+MICU1 cells was restored to WT levels. (**C**) Ca^{2+}-uptake rates for MCU+EMRE+MICU1 and MCU+P76I-EMRE+MICU1 cells in response to bolus additions of $CaCl_2$ that increase $[Ca^{2+}]_c$ by ~5 µM (n $\geq$ 3 independent experiments). Replicate measurements shown as hollow circles, boxes: 25th-75th percentile with line at median, error bars: range of all measurements. P-values: comparison of MCU+EMRE+MICU1 cells with MCU+P76I-EMRE+MICU1 cells (*P < 0.05; **P < 0.01; ***P < 0.001; ****P < 0.0001; n.s., not different; unpaired t test with Welch's correction). (**D**) Ca^{2+}-uptake rates between 0.1 - 10 µM $[Ca^{2+}]_c$ measured in (B and Figure 3.8B) plotted on log_{10}/log_{10} scale. Each point (hollow circle) represents an independent experiment. Solid lines: linear fits of (log_{10}) Ca^{2+}-uptake rate vs. (log_{10}) $[Ca^{2+}]_c$. Slope of the best-fit line is a measure of the cooperativity of the MCU transition from closed- to the open-state, which was similar between MCU+EMRE+MICU1 and MCU+P76I-EMRE+MICU1 cells. (**E**) Steady-state $[Ca^{2+}]_c$ for experiments in (D) measured 300 sec after bolus addition of 0.1 - 10 µM Ca^{2+} plotted as function of the initial peak $[Ca^{2+}]_c$ achieved immediately after addition. Each point (hollow circle) represents an independent experiment (n $\geq$ 12 for each condition). Solid lines: one-phase association fits of steady-state $[Ca^{2+}]_c$ vs. the initial $[Ca^{2+}]_c$ after addition. (**F**) Comparison of gatekeeping-threshold $[Ca^{2+}]_c$ from non-linear fits in (E). Bars: mean of plateau parameter for each fit +/- SEM. P-value: comparison of MCU+EMRE+MICU1 cells with MCU+P76I-EMRE+MICU1 cells (*P < 0.05; **P < 0.01; ***P < 0.001; ****P < 0.0001; n.s., not different; unpaired t test with Welch's correction). The gatekeeping threshold in MCU+P76I-EMRE+MICU1 was elevated relative to MCU+EMRE+MICU1 cells.

Creation of MCU-EMRE concatemers to form channels with fixed EMRE:MCU stoichiometries

Co-expression of MCU and EMRE at known ratios cannot determine the stoichiometries of the two proteins in the functional channel complex. To address this, we created a system in which we could establish fixed EMRE:MCU stoichiometries. We expressed a synthetic protein in which a truncated EMRE (ΔN30 a.a.) peptide containing a C-terminal V5 tag was fused to the C-terminus of MCU (Figure 3.12A). This construct was previously shown to reconstitute MCU channel activity in the absence of endogenous MCU and EMRE expression (Tsai et al., 2016). We stably transfected the MCU-EMRE fusion protein (hereafter referred to as ME) in MEKO cells. Western blotting for V5 demonstrated that the fusion protein was expressed at the expected size but probing with an α-MCU antibody revealed the presence of a smaller band at the approximate molecular weight of MCU (Figure 3.13A). We surmised that this was caused by proteolytic cleavage. To minimize this degradation, we introduced the P76I mutation into the ME concatemer (ME[P76I]). The degradation observed with the original construct was mitigated by expression of the mutant construct (Figure 3.13A).

Expression of ME[P76I] in MEKO cells is predicted to result in a 1:1 EMRE:MCU stoichiometry in all channel complexes (Figure 3.12B). We also created MCU-EMRE[P76I] fusion proteins with two, three or four concatenated MCU subunits fused to P76I-EMRE (hereafter referred to as MME, MMME and MMMME respectively). MME is predicted to dimerize, forming complexes with two EMRE subunits/MCU channel (Figure 3.12C), and MMMME is predicted to form complexes with one EMRE subunit/MCU tetramer. In contrast, MMME should be unable to form tetramers in MEKO cells, although alternate assemblies (e.g. hexamers) may form that still retain channel activity (Figure 3.12D). MEKO cells were stably transfected with each concatemer together with MICU1-Flag to ensure sufficient MICU1. Three clones were identified for each condition and whole-cell lysates were analyzed for MCU and MICU1/2-heterodimer expression by western blot (Figure 3.13B). Surprisingly, the MMMME construct failed to express (Figure 3.13E). Thus, to create channels with a single EMRE subunit/MCU tetramer, the MMME concatemer and MICU1-Flag were expressed in EMRE KO (HEK-293T) cells (Figure 3.12E) and three stable

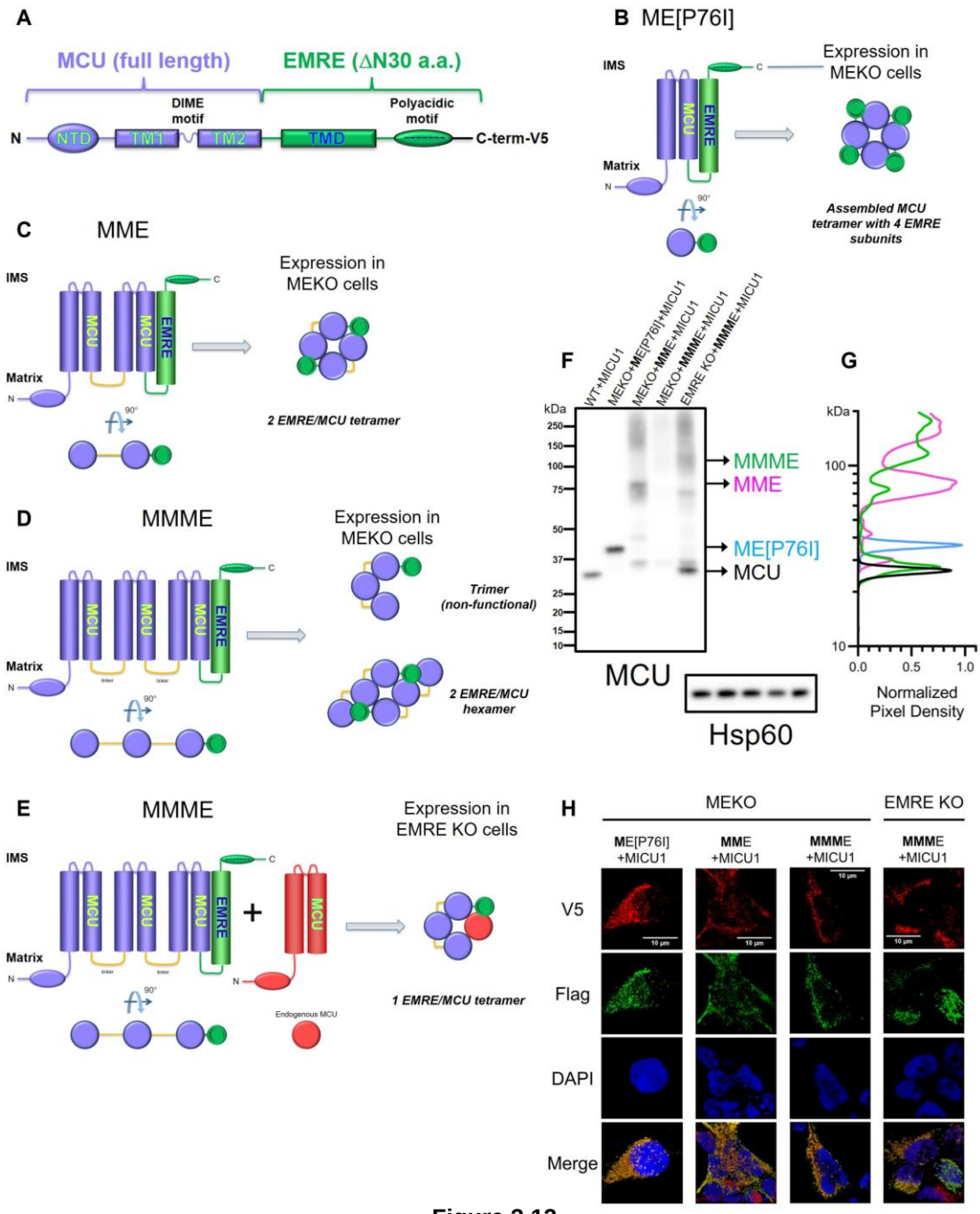

Figure 3.12

clones were isolated as described. The presence of endogenous MCU in these cells should allow a single MCU monomer to associate with the MMME concatemer to form tetrameric channel complexes containing only one EMRE subunit. To probe the integrity of each concatemer, mitochondria were isolated from selected clones and analyzed by western blot. The ME[P76I],

Figure 3.12. Creation of MCU-EMRE concatemers to form channels with fixed EMRE:MCU stoichiometries

(**A**) The MCU-EMRE fusion protein comprised of full-length MCU fused directly to an EMRE peptide with the 30-residue mitochondrial-targeting sequence truncated from its N-terminus, followed by C-terminal V5 tag. (**B**) Assembly of the ME concatemer (ME[P76I]) enforces a 1:1 EMRE:MCU stoichiometry in all channel complexes when expressed in MEKO cells. (**C**) The MME concatemer assembles as an MCU tetramer containing 2 EMRE subunits in MEKO cells. (**D**) The MMME concatemer cannot assemble as an MCU tetramer, but formation of hexamers or other higher-order oligomers may lead to assembly of functional channels in MEKO cells. (**E**) Expression of MMME in EMRE KO cells allows formation of channel complexes containing a single EMRE subunit due to the presence of endogenous MCU monomers. (**F**) Western blot for MCU and Hsp60 in isolated mitochondria from representative clones of WT+MICU1, MEKO+ME[P76I]+MICU1, MEKO+MME+MICU1, MEKO+MMME+MICU1 or EMRE KO+MMME+MICU1 cells under reducing conditions. (**G**) Quantification of molecular weight from normalized band intensity for α-MCU western blots in (F). Traces: mean of n = 3 replicate experiments. A single ~40 kDa band was observed in cells expressing ME[P76I]; MME exhibited bands at ~80 and 160 kDa; MMME ran at ~110 and 220 kDa. Band at ~35 kDa in EMRE KO+MMME+MICU1 cells represents endogenous MCU. (**H**) Immunofluorescence microscopy for V5 (MCU-EMRE concatemers), Flag (MICU1) and DAPI in representative clones of cell lines in (F). All cell lines tested showed strong colocalization of both tags in mitochondria.

MME, and MMME concatemers were all predominantly expressed as full-length proteins (ME~40kDa; MME~80 kDa, and MMME~110 kDa respectively - Figure 3.12F-G). Localization of each concatemer and MICU1-Flag to mitochondria was confirmed by confocal immunofluorescence microscopy (Figure 3.12H). It was possible to compare MCU expression levels in ME[P76I] clones with that in WT cells as this concatemer exhibited a single band in western blots and contained a single MCU epitope. ME[P76I] was ~2-fold overexpressed in one clone (#3), modestly (< 2-fold) overexpressed in a second clone (#1), and slightly lower (~2-fold) than WT cells in a third clone (#2) (Figure 3.13C). The presence of high molecular weight bands in cells expressing MME and MMME made it difficult to assess the relative MCU levels. This was further confounded by possible differences in MCU antibody binding to fusion proteins containing multiple MCU subunits. We therefore employed V5-epitope ELISA assays on each clonal cell line. Based on the relationship in ME[P76I] clone #2 between western blot expression and the relative number of V5-binding sites per cell, the MCU expression level was estimated to vary by only 2-fold in the different concatemeric clones (Figure 3.14A). MICU1/2 dimer expression in all clones was at least as high as in WT cells (Figure 3.13B&D).

We assessed mitochondrial Ca^{2+} uptake in each cell line at both high (5-8 μM) and low (< 600 nM) $[Ca^{2+}]_c$ to determine (i) whether each concatemer was sufficient to form functional channels in the absence of endogenous MCU or EMRE expression, and (ii) if the channels exhibited MICU1/2-mediated gatekeeping. Each concatemer reconstituted MCU activity, with

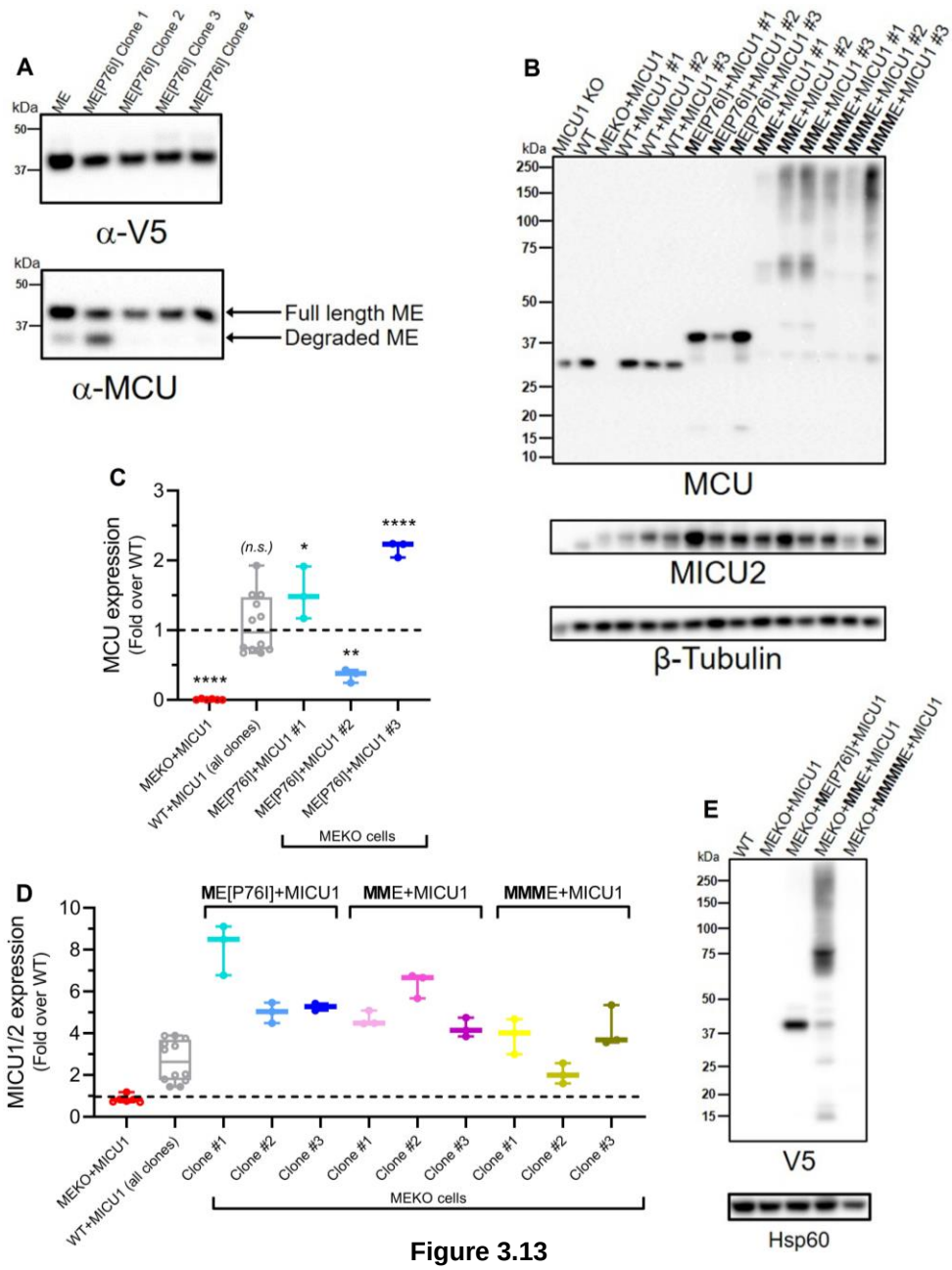

Figure 3.13

some variability among clones in the Ca^{2+}-uptake rates (ranging from ~100 to 400 nM/sec) in response to 5 µM Ca^{2+} boluses (Figure 3.14B). Six out of twelve clones displayed intact gatekeeping at low (< 600 nM) $[Ca^{2+}]_c$ (Figure 3.14C). For further analysis, we selected individual clones for each concatemeric construct that had mean Ca^{2+}-uptake rates at 5-8 µM $[Ca^{2+}]_c$ most similar to WT cells and intact gatekeeping in the low-$[Ca^{2+}]_c$ regime (Figure 3.14A-C – red arrows). For each, we measured both the Ca^{2+}-uptake rates in response to 0.1 - 10 µM $[Ca^{2+}]_c$

Figure 3.13. MCU and MICU1/2 expression in MCU-EMRE concatemer cell lines

(**A**) Western blot for V5 (top) and MCU (bottom) for whole-cell lysates of clonal MEKO cells stably-expressing ME (WT) (lane 1) or ME[P76I] (lanes 2-5). The EMRE [P76I] mutation prevents degradation of the ME concatemer in three of four clones. (**B**) Western blot for MCU, MICU2 (under non-reducing conditions) and β-tubulin from whole-cell lysates of WT, MEKO+MICU1, three clones of WT+MICU1, and three clones each of MEKO cells expressing ME[P76I]+MICU1, MME+MICU1, or MMME+MICU1. MICU1-Flag overexpression in each clone is evident from the increase in molecular weight of MICU1/2 dimers under non-reducing conditions. (**C**) Quantification of MCU western blot band intensity from whole-cell lysates of WT, MEKO+MICU1, WT+MICU1 and three clones of MEKO+ME[P76I]+MICU1 cells ($n \geq 3$ independent experiments). Mean pixel density corrected for β-tubulin intensity and normalized to endogenous MCU band intensity in WT+MICU1 cells for each experiment. Replicate measurements shown as hollow circles, boxes: 25^{th}-75^{th} percentile with line at median, error bars: range of all measurements. P-values: comparison of each cell line with WT cells (*P < 0.05; **P < 0.01; ***P < 0.001; ****P < 0.0001; n.s., not different; Dunnett's multiple comparisons test). (**D**) Quantification of MICU2 western blot band intensity for cells in (B) from $n \geq 3$ independent experiments quantified as described in (C). Replicate measurements shown as hollow circles, boxes: 25^{th}-75^{th} percentile with line at median, error bars: range of all measurements. Total MICU1/2 dimer expression is higher than WT in all cell lines expressing MICU1-Flag. (**E**) Western blot for V5 and Hsp60 of isolated mitochondria from representative clones of WT+MICU1, MEKO+MICU1, MEKO+ME[P76I]+MICU1, MEKO+MME+MICU1 and MEKO+MMMME+MICU1 cells under reducing conditions. No detectable MMMME expression observed.

and the subsequent steady-state $[Ca^{2+}]_c$ at which gatekeeping was re-established (Figure 3.15A-D). Plotting the uptake rate as a function of the peak $[Ca^{2+}]_c$ immediately after Ca^{2+} addition and fitting the data to a Hill equation revealed similar profiles for the different concatemers, with the rate for cells expressing ME[P76I] notably right-shifted to higher $[Ca^{2+}]_c$ (Figure 3.15E). Linear fits of the data on a log/log scale showed that cooperativity in the transition of MCU from the closed- to the open-state was the same for each concatemer (slope = 2.5), and similar to WT+MICU1 cells (Figure 3.15F), suggesting that MICU1/2 regulation was properly coupled to the channel in each concatemeric complex. However, the threshold at which gatekeeping was re-established for each concatemer (Figure 3.15G) was elevated uniquely in cells expressing ME[P76I] (Figure 3.15H). This result is consistent with the right-shifted Ca^{2+}-dependence of MCU activation observed in these cells and suggests that gatekeeping is particularly potent in MCU complexes containing 4 EMRE/channel. In contrast, the gatekeeping threshold in cells expressing concatemers predicted to form channels with fewer than 4 EMRE subunits were not different from WT (Figure 3.15H). These results strongly suggest that channels containing 4 EMRE subunits tether more MICU1/2 dimers to the channel complex than are normally present in WT cells, consistent with the analysis above that EMRE:MCU stoichiometry, and by analogy, the MICU1/2 dimer:MCU stoichiometry, may not be 4:4 or invariant in cells. This is also consistent with prior studies showing that the relative MICU1 and MCU stoichiometry in cells from different tissues

affects both the $[Ca^{2+}]_c$ gatekeeping threshold and cooperativity of gatekeeping (Paillard et al., 2017).

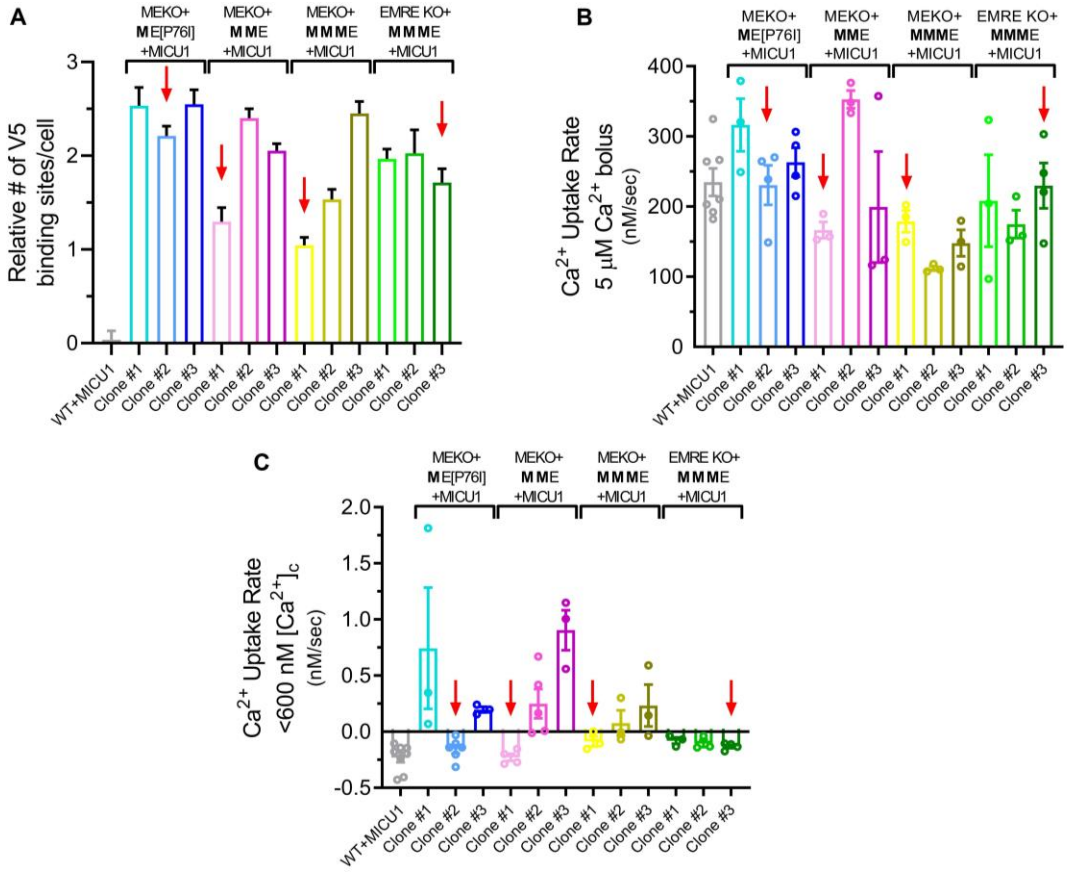

Figure 3.14. Biochemical and functional characterization of MCU-EMRE concatemers in clonal cell lines

(**A**) ELISA quantification of V5 expression for three clones each of WT+MICU1 (pooled), MEKO+ME[P76I]+MICU1, MEKO+MME+MICU1, MEKO+MMME+MICU1 and EMRE KO+MMME+MICU1. Bars: mean of B_{max} parameter for each fit +/- SEM (n = 3). Red arrows: lowest expressing clone for each condition. (**B**) Quantification of mitochondrial Ca^{2+}-uptake rates in response to bolus additions to raise $[Ca^{2+}]_c$ by 5 µM for cell lines in (A). Each point represents initial Ca^{2+}-uptake rate from an independent experiment ($n \geq 3$ for each condition) determined by single-exponential fit to reduction of $[Ca^{2+}]_c$. Replicate measurements shown as hollow circles, bars: mean +/- SEM. Clones with mean uptake rates most closely approximating WT for each condition shown by red arrows. (**C**) Quantification of mitochondrial Ca^{2+}-uptake rate below 600 nM $[Ca^{2+}]_c$ in response to inhibition of NCLX-mediated Ca^{2+} efflux for cell lines in (A). Each point represents initial Ca^{2+}-uptake rate from an independent experiment ($n \geq 3$ for each condition) determined by single-exponential fit to reduction of $[Ca^{2+}]_c$. Replicate measurements shown as hollow circles, bars: mean +/- SEM. Clones with uptake rates < 0 nM/sec (denoted by red arrows) exhibit intact gatekeeping at low $[Ca^{2+}]_c$.

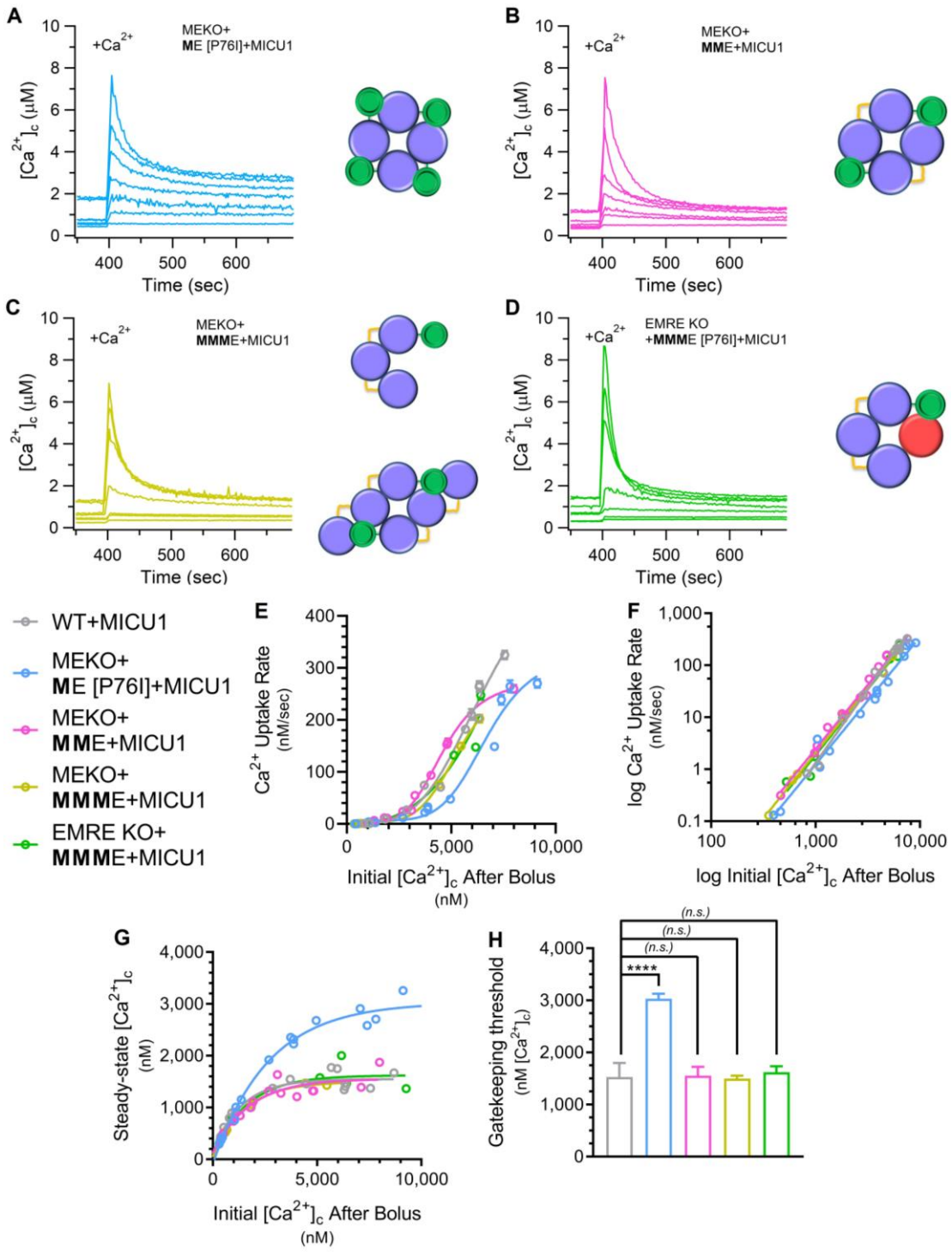
A
MEKO+
ME [P76I]+MICU1
+Ca2+
[Ca2+]c (μM)
Time (sec)
B
MEKO+
MME+MICU1
C
MEKO+
MMME+MICU1
D
EMRE KO
+MMME [P76I]+MICU1
WT+MICU1
MEKO+
ME [P76I]+MICU1
MEKO+
MME+MICU1
MEKO+
MMME+MICU1
EMRE KO+
MMME+MICU1
E
Ca2+ Uptake Rate
(nM/sec)
Initial [Ca2+]c After Bolus
(nM)
F
log Ca2+ Uptake Rate
(nM/sec)
log Initial [Ca2+]c After Bolus
G
Steady-state [Ca2+]c
(nM)
Initial [Ca2+]c After Bolus
(nM)
H
Gatekeeping threshold
(nM [Ca2+]c)
(n.s.)
(n.s.)
(n.s.)
****

Figure 3.15

Figure 3.15. Function of MCU-EMRE concatemers

(**A-D**) Mitochondrial Ca^{2+} uptake in suspensions of permeabilized MEKO+ME[P76I]+MICU1 (A), MEKO+MME+MICU1 (B), MEKO+MMME+MICU1 (C) and EMRE KO+MMME+MICU1 (D) cells in response to acute increases of $[Ca^{2+}]_c$ to between 0.1 - 10 μM. Individual traces from independent experiments with different bolus additions shown. (**E**) Ca^{2+}-uptake rates for cell lines in (A-D) in response to challenge with $[Ca^{2+}]_c$ between 0.1 - 10 μM. Each point (hollow circle) represents an independent experiment. Solid lines: Hill equation fits of Ca^{2+}-uptake rate vs. initial $[Ca^{2+}]_c$ after bolus addition. ME[P76I]+MICU1 cells exhibited a right-shift in the $[Ca^{2+}]_c$-dependence of MCU activation compared to all other cell lines. (**F**) Ca^{2+}-uptake rates between 0.1 - 10 μM $[Ca^{2+}]_c$ measured in (E) plotted on $\log_{10}/\log_{10}$ scale. Each point (hollow circle) represents an independent experiment. Solid lines: linear fits of ($\log_{10}$) Ca^{2+}-uptake rate vs. ($\log_{10}$) $[Ca^{2+}]_c$. Slope of the best-fit line is a measure of the cooperativity of the MCU transition from closed- to the open-state, which was similar among all cell lines. (**G**) Steady state $[Ca^{2+}]_c$ for cells in (E) measured 300 sec after bolus addition of 0.1 - 10 μM Ca^{2+} plotted as a function of initial peak $[Ca^{2+}]_c$ immediately after addition. Each point (hollow circle) represents independent experiment ($n \geq 6$ for each condition). Solid lines: one-phase association fits of steady-state gatekeeping-threshold $[Ca^{2+}]_c$ vs. initial $[Ca^{2+}]_c$ after addition. (**H**) Comparison of gatekeeping-threshold $[Ca^{2+}]_c$ 300 sec after bolus additions of Ca^{2+} from non-linear fits in (G). Bars: mean of plateau parameter for each fit +/- SEM. P-values: pairwise comparisons of each cell line with WT+MICU1 cells (*P < 0.05; **P < 0.01; ***P < 0.001; ****P < 0.0001; n.s., not different; Tukey's multiple comparisons test). The gatekeeping threshold $[Ca^{2+}]_c$ was elevated in ME[P76I]+MICU1 cells compared to all other cell lines.

Biochemical analyses of complexes formed by MCU-EMRE concatemers

To compare the relative sizes of channel complexes in cells expressing MCU-EMRE concatemers with endogenous complexes, we performed BN-PAGE western blotting of MCU from isolated mitochondria. The MCU complex in WT cells ran as a single band at ~440 kDa (Figure 3.16A,C-D&F: black), in line with previous reports (Sancak et al., 2013)(König et al., 2016). Overexpression of MICU1-Flag in WT cells had no effect on the size of the complex (Figure 3.16A,C-D&F: gray). In addition, MCU ran at approximately the same size in MICU1 KO mitochondria as in WT mitochondria (Figure 3.16A,C-D&F; red), with a minor band of lower molecular weight similar in size to that observed in EMRE KO mitochondria (~350 kDa) (Figure 3.16A,C-D&F: orange). This result is consistent with a previous report that MICU1 may stabilize interactions between MCU and EMRE, and that MCU-containing bands at ~440 kDa do not contain MICU proteins (König et al., 2016). Re-probing the same blots with an α-Flag antibody revealed that MICU1 assembled in complexes of ~250 and ~400 kDa in the absence of MCU and EMRE (Figure 3.16B) further indicating that complexes at ~440 kDa detected with the α-MCU antibody contained only MCU and EMRE subunits.

Importantly, complexes from mitochondria expressing ME[P76I] with an enforced 1:1 EMRE:MCU stoichiometry (Figure 3.16A,C,E-F: blue) were significantly larger (~490 kDa) than

those observed in WT or WT+MICU1 mitochondria, suggesting that endogenous MCU channels contain fewer than four EMRE subunits. A minor band at ~700 kDa was observed in ME[P76I] mitochondria, possibly corresponding to a dimer of MCU tetramers. Bands at ~440 and ~700 kDa were also seen in mitochondria from cells expressing MME and MMME, although higher molecular weight oligomers were evident (Figure 3.16A&C: pink, gold, and green). This could indicate a tendency for the concatemers to form complexes containing more than one MCU channel. Importantly, analysis of only the lowest molecular weight bands revealed that MME and

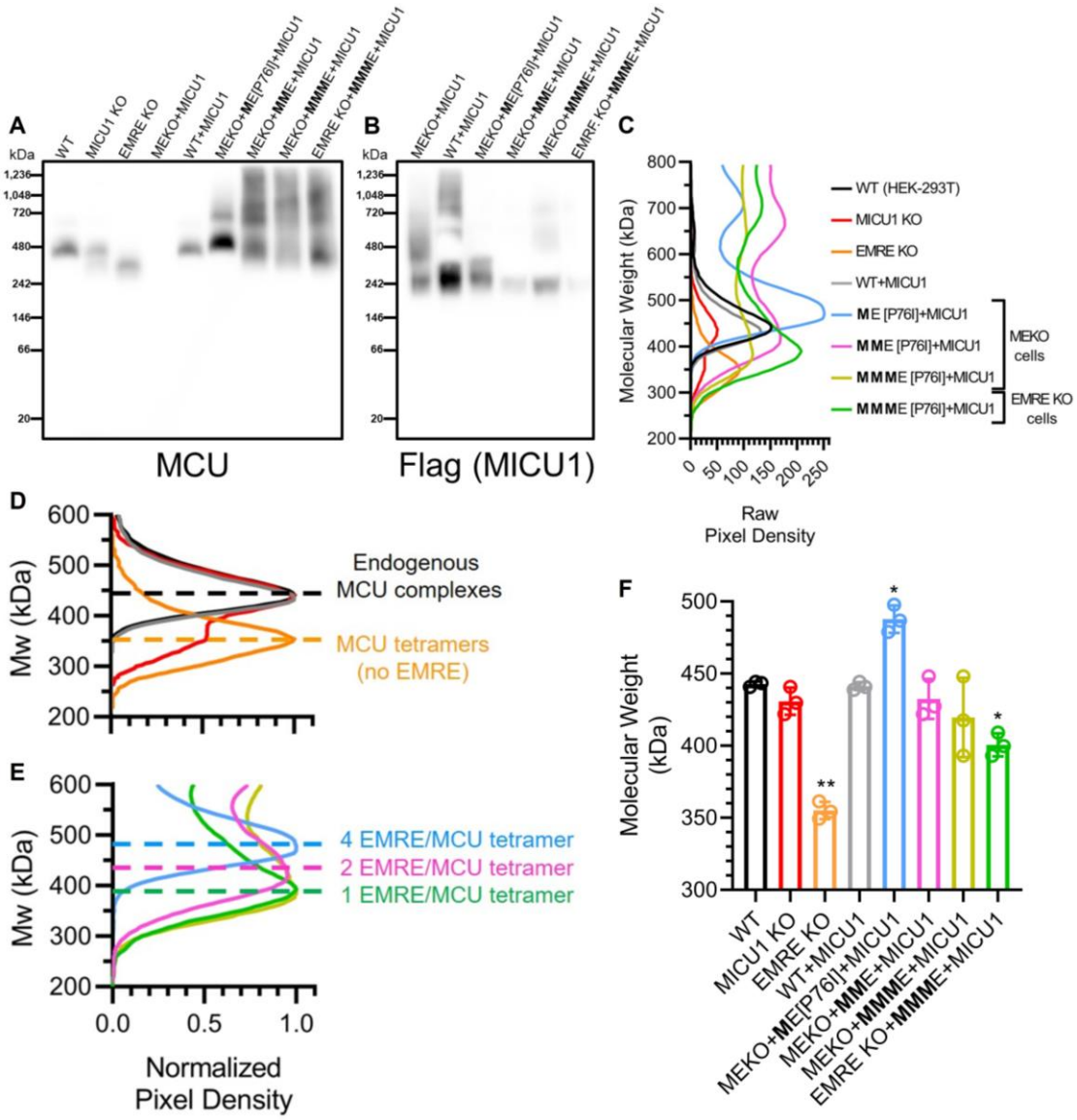

Figure 3.16

Figure 3.16. Biochemical analyses of channel complexes formed by MCU-EMRE concatemers

(**A**) BN-PAGE MCU western blot of mitochondria isolated from WT, MICU1 KO, EMRE KO, MEKO+MICU1 cells and representative clones of WT+MICU1, MEKO+ME[P76I]+MICU1, MEKO+MME+MICU1, MEKO+MMME+MICU1, and EMRE KO+MMME+MICU1 cells. Endogenous MCU channel complexes observed as single band at ~440 kDa. (**B**) BN-PAGE western blot for Flag (MICU1) in mitochondria isolated from representative clones of MEKO+MICU1, WT+MICU1, MEKO+ME[P76I]+MICU1, MEKO+MME+MICU1, MEKO+MMME+MICU1, and EMRE KO+MMME+MICU1 cells. MICU1 formed complexes at ~250 and ~400 kDa in cells lacking MCU and EMRE. (**C**) Quantification of raw intensity and molecular weight from α-MCU BN-PAGE western blots in (A). Traces: mean of n = 3 replicate experiments. All MCU-EMRE concatemers showed bands between 300-600 kDa (similar to WT cells), as well as bands at > 700 kDa that likely represent complexes containing > 4 MCU subunits. (**D-E**) Molecular-weight profile of the smallest band (200-600 kDa) from α-MCU BN-PAGE western blots of cell lines in (C). Traces: mean of n = 3 replicate experiments. Data are normalized to band with maximal intensity for each condition. (D) MCU complexes in MICU1 KO cells (red) were similar to WT (+/- MICU1 – black & gray), with a minor band similar in size to complexes formed in EMRE KO cells (orange). (E) Concatemers of MCU and EMRE exhibited molecular weights that varied in size proportionally to the predicted number of EMRE subunits per complex. (**F**) Statistical analysis of molecular weight profiles in (D-E). Replicate measurements shown as hollow circles (n = 3). Bars: mean calculated size of each complex derived from peak intensity of band between 200-600 kDa +/- SEM. P-values: pairwise comparisons of each cell line with WT cells (*P < 0.05; **P < 0.01; ***P < 0.001; ****P < 0.0001; n.s., not different; Dunnett's multiple comparisons test). Complexes with 4 EMRE subunits per channel (ME[P76I] – blue) were significantly larger than those in WT cells (black), while complexes containing only 1 EMRE subunit (EMRE KO+MMME – green) were smaller.

MMME complexes were not different in size from endogenous channels (Figure 3.16E-F: pink and gold). Interestingly, complexes in EMRE KO cells expressing MMME, which are predicted to contain a single EMRE subunit, were significantly smaller than those in WT cells (Figure 3.16A,C,E-F: green), suggesting that endogenous MCU channels associate with more than one EMRE.

CHAPTER 4: Conclusions and Future Directions

MICU2 restricts spatial crosstalk between $InsP_3R$ and MCU channels by regulating threshold and gain of MICU1-mediated inhibition and activation of MCU

In Chapter 2, I have quantitatively described the roles of MICU1 and MICU2 in regulating MCU activity *in situ* over a full range of $[Ca^{2+}]_c$ experienced by the channel under resting conditions and during agonist stimulation. We found that each protein plays important but distinct roles in both the inhibition of MCU-channel activity in the low-$[Ca^{2+}]_c$ regime and in the highly cooperative activation of the channel as $[Ca^{2+}]_c$ is elevated. Our studies clarify the specific functions of each MICU protein in MCU gatekeeping and highlight the requirement for Ca^{2+} binding to three or all four EF-hand domains in the MICU1/2 dimer to activate mitochondrial Ca^{2+} uptake.

MICU1 and MICU2 have distinct roles in MCU inhibition

In the low-$[Ca^{2+}]_c$ regime approximating resting-cytoplasmic conditions, MICU1, but not MICU2, plays a fundamental role in the suppression of MCU activity referred to as “gatekeeping”. In the absence of MICU1, MCU becomes constitutively active, in agreement with previous reports (Mallilankaraman et al., 2012b)(Csordás et al., 2013)(Patron et al., 2014)(Liu et al., 2016). Whereas some previous studies were confounded by reduced MICU2 expression in cells with MICU1 knocked-down or deleted, here we observed similar constitutive activity even when MICU2 was re-expressed to normal levels in MICU1 KO cells. Thus, MICU2 is not the dominant mechanism of gatekeeping as previously suggested (Patron et al., 2014). Constitutive MCU activity in MICU1 KO cells activates NCLX-mediated Ca^{2+} extrusion, but this is insufficient to defend normal resting $[Ca^{2+}]_m$. Thus, in the absence of MICU1, constitutive influx and efflux constitutes an ongoing Ca^{2+} cycling across the IMM that establishes a new, higher steady state $[Ca^{2+}]_m$. This could in part explain the disease phenotypes observed in patients with loss-of-function mutations in MICU1.

We found that MICU2 is not required for channel gatekeeping. Deciphering its role has been complicated by the fact that it requires MICU1 for its association with MCU. Here we demonstrated that MICU2 deletion leaves channel inhibition intact, indicating that MICU1 homodimers are capable of inhibiting MCU-channel activity in low $[Ca^{2+}]_c$. Although MICU2 is dispensable for inhibition of MCU in the low-$[Ca^{2+}]_c$ regime (50-500 nM), it nevertheless plays a role in regulating MICU1-mediated gatekeeping by tuning the normal threshold for relief of channel inhibition. Deletion of MICU2 lowered the $[Ca^{2+}]_c$ threshold for relief of inhibition from ~1.3 µM in WT cells to ~500 nM. Thus, in the range of $[Ca^{2+}]_c$ between 500 nM and ~1.5 µM, MICU2 plays a critical role by tuning the activity of MICU1 to inhibit MCU (Figure 4.1). Under normal conditions with both MICU proteins present in a heterodimeric complex, the Ca^{2+}-binding EF hands appear to play little or no role in MCU channel inhibition in the low-$[Ca^{2+}]_c$ regime. Since mutation of EF hands did not affect heterodimer formation or association with MCU, MICU2 tunes the MICU1-mediated threshold for activation through distinct Ca^{2+}-binding properties of MICU1 homo- vs. heterodimers. Previous studies have reported a loss of gatekeeping in cells with MICU2 deleted (Vais et al., 2016). However, those measurements used a low-affinity Ca^{2+} indicator (Fura-FF; K_D = 5.5 µM) that provided inaccurate measurements below 1 µM. By probing Ca^{2+} uptake using a high-affinity indicator (Fura-2, K_D = 140 nM), we determined that the MICU1 homodimer inhibits MCU below ~500 nM $[Ca^{2+}]_c$. Lack of appreciation of this role of MICU2 and of the need to study its function under rigorously controlled

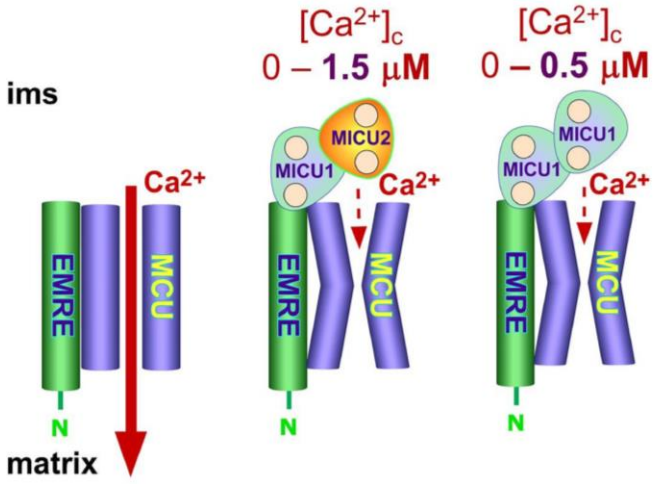

Figure 4.1. Model for MICU1-MICU2 regulation of MCU at resting $[Ca^{2+}]_c$

MICU2 tunes MCU activation by elevating the $[Ca^{2+}]_c$ threshold for relief of MICU1-mediated inhibition of MCU.

and quantified $[Ca^{2+}]_c$ probably accounts for previous discrepant results regarding its effects on gatekeeping (Patron et al., 2014)(Kamer and Mootha, 2014)(Vais et al., 2016).

MICU2 sets the gain of cooperative activation of MCU by MICU1

Activation of MCU is mediated by elevated $[Ca^{2+}]_c$ with high cooperativity. As for channel inhibition in low $[Ca^{2+}]_c$, MICU1 plays a dominant role in channel activation. First, channel activation at $[Ca^{2+}]_c$ > 5 µM is strongly reduced in cells lacking MICU1. This observation likely accounts for the initial (Perocchi et al., 2010) and subsequent (Csordás et al., 2013)(Patron et al., 2014) conclusion that MICU1 mediates channel activation rather than inhibition, since those studies employed high-$[Ca^{2+}]_c$ pulses where MICU1 is shown here to play an activating role. Second, cooperativity of channel activation is lost when MICU1 is absent. Third, $[Ca^{2+}]_c$ dependent MCU activation remains highly cooperative in cells with MICU2 deleted. Nevertheless, MICU2 profoundly influences Ca^{2+}-dependent MCU activation. In its absence, activation by MICU1 homodimers remains highly cooperative, but the $[Ca^{2+}]_c$ -dependence is shifted to much lower concentrations. Thus, a primary function of MICU2 is to set the gain of the cooperative mechanism of channel activation (Figure 4.2). Cooperative channel activation requires Ca^{2+} binding not only to each of the EF hands in MICU1, but also to those in MICU2. Mutation of EF1 in MICU2 had a more profound effect than mutation of EF2, which is interesting since MICU2 EF1 has been implicated in MICU2 dimerization *in vitro* (Li et al., 2016)(Kamer et al., 2019). Thus, cooperativity of $[Ca^{2+}]_c$ dependent MCU activation derives from Ca^{2+} binding to

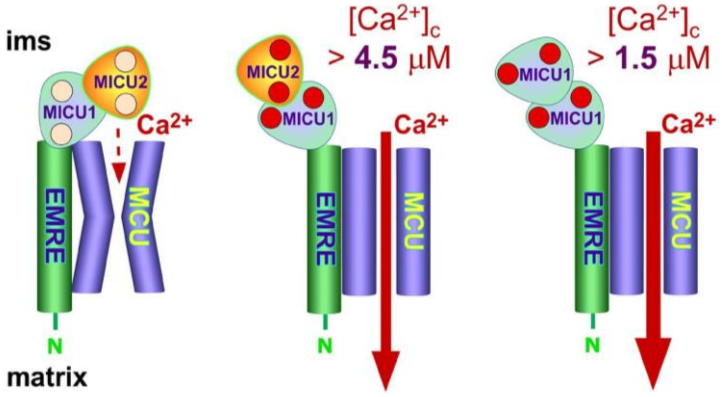

Figure 4.2. Model for MICU1-MICU2 regulation of MCU in response to elevations in $[Ca^{2+}]_c$

MICU2 tunes mitochondrial Ca^{2+} uptake by raising the $[Ca^{2+}]_c$ threshold and reducing the gain of MICU1 activation of MCU.

three or all four EF hands in the MICU1/2 heterodimer (Figure 4.3).

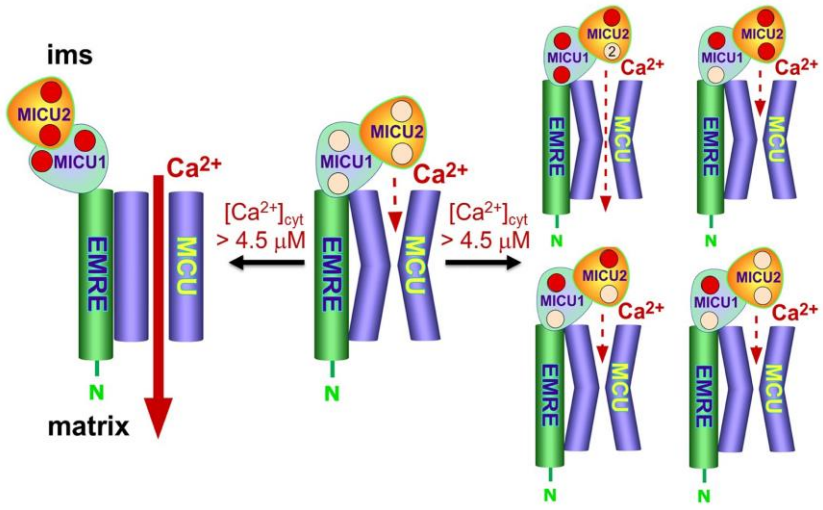

Figure 4.3. Ca^{2+} binding to the EF hands of MICU1 and MICU2 is necessary for cooperative activation MCU Ca^{2+} binding to 3-4 EF hands in the MICU1/2 heterodimer are required for MCU activation.

In support of these findings, Kamer et al. (2017) demonstrated that recombinant truncated-MICU1 and full-length MICU2 form a heterodimer with high Ca^{2+} affinity (~650 nM). The apparent Ca^{2+} affinity of MICU1 was ~300-400 nM, whereas MICU2 had a lower affinity (~1 µM). These results are in good agreement with the apparent affinities of the full-length proteins *in situ* observed here. A MICU1 apparent-affinity of 300-400 nM is in good agreement with the 500-nM threshold we determined in cells lacking MICU2, and the lower Ca^{2+} affinity of the MICU1/2 dimer is consistent with the role of MICU2 determined here to raise the $[Ca^{2+}]_c$ threshold and lower the apparent Ca^{2+} affinity of the MICU dimer.

The cell physiological significance of MICU2

It is interesting to note that MICU1 alone is able to accomplish the same things as a MICU1/2 heterodimer. MICU1 homodimers (and possibly monomers) associate with MCU and mediate channel inhibition in low $[Ca^{2+}]_c$ and highly-cooperative activation at elevated $[Ca^{2+}]_c$. MICU2 does not form a homodimer, nor does it associate with MCU in the absence of MICU1. Although ratios of MICU1 and MICU2 mRNA levels vary among tissues, it is unknown if MICU1

homodimers exist in vertebrate tissues. Paillard et al. (2017) observed different MICU1/MCU expression ratios between cardiac myocytes and hepatocytes, and attributed different mitochondrial Ca^{2+}-uptake properties between these tissues to altered MICU1/MCU ratios. However, the results, i.e. lower threshold and reduced gain in myocytes, could also be accounted for, at least in part, by different ratios of MICU1 homo- versus heterodimers, as shown here. It is interesting to consider the physiological implications of the evolution of the MICU1/2 heterodimer. Our studies suggest that the fundamental role of MICU2 is to reduce the apparent Ca^{2+} affinity of MICU1. In the low-$[Ca^{2+}]_c$ regime, MICU2 raises the $[Ca^{2+}]_c$ threshold for MCU activation from ~500 nM to ~1.3 µM. In the high-$[Ca^{2+}]_c$ regime, MICU2 reduces the $[Ca^{2+}]$ sensitivity without affecting the cooperativity of channel activation, enabling strong channel-activation at $[Ca^{2+}]_c$ > 4.5 µM compared with ~1.5 µM for MICU1 homodimers. Considering the requirement of Ca^{2+} binding to MICU2 EF hands for channel activation, it is notable that whereas the two MICU1 EF hands are canonical, those in MICU2 are not, with the normal glycines at position 6 replaced with glutamates. This may suggest that the MICU2 EF hands have a lower Ca^{2+}-binding affinity, in agreement with recent measurements (Kamer et al., 2017), that within the context of the MICU1/2 heterodimer confers reduced $[Ca^{2+}]_c$-sensitivity.

The cell physiological implication of these effects of MICU2 may be to enforce a more-proximal physical localization between MCU and Ca^{2+} sources required for mitochondria to sense and take up Ca^{2+}. Using the physiological Ca^{2+} current through a single open $InsP_3R$ Ca^{2+}-release channel, we can compute the spatial profile of $[Ca^{2+}]_c$ as a function of distance from the channel according to (Vais et al., 2010). Assuming moderate cytoplasmic buffering (between the values for high and low buffering in Vais et al.) and $[Ca^{2+}]_{ERlumen}$ = 300 µM, modeling predicts that with a MICU1/2 heterodimer as part of the MCU complex, an MCU channel needs to be located within ~120 nm from the axis of a single open $InsP_3R$ channel for the inhibition threshold to be breached, enabling MCU activation. In contrast, an MCU channel associated with a MICU1 homodimer could be twice as far away and become activated (Figure 4.4). Thus, the presence of MICU2 requires an MCU channel to be closer to an $InsP_3R$ to enable the gatekeeping threshold

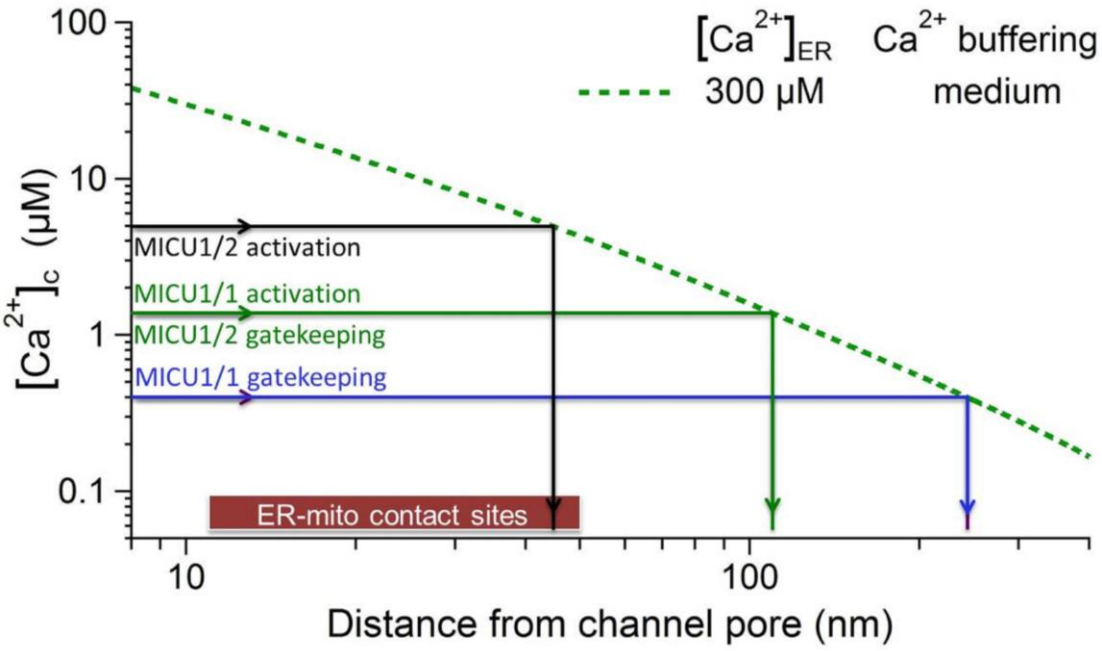

Figure 4.4. MICU2 enforces tighter localization of Ca^{2+} crosstalk between ER and mitochondria (adapted from Vais et al., 2010)

Assuming $[Ca^{2+}]_{ER}$ = 300 μM, MCU channels associated with a MICU1/2 heterodimer must be located within 60 nm of the axis of an open $InsP_3R$ channel for cooperative activation and within 120 nm for the gatekeeping threshold-$[Ca^{2+}]_c$ to be exceeded, whereas MCU associated with a MICU1 homodimer could be over 120 nm and 240 nm away, respectively.

to be overcome. A MICU1/2 heterodimer strongly activates MCU channel activity when $[Ca^{2+}]_c$ achieves ~4.5 μM, requiring that the MCU channel be within 60 nm of an $InsP_3R$, whereas a MICU1 homodimer-activated MCU channel can be over twice as far away (Figure 4.4). Again, the presence of MICU2 spatially restricts Ca^{2+} crosstalk between single $InsP_3R$ and MCU channels. It is predicted, therefore, that stimulation of $InsP_3$-mediated Ca^{2+} release in cells lacking MICU2 would be associated with a larger proportion of released Ca^{2+} entering mitochondria.

To test this, we stimulated intact cells with an $InsP_3$-mobilizing agonist and simultaneously measured $[Ca^{2+}]_c$ and $[Ca^{2+}]_m$. Notably, the magnitude of the transient increase in global $[Ca^{2+}]_c$ was suppressed in MICU2 KO cells compared with WT cells (Figure 4.5A) whereas the peak increase in $[Ca^{2+}]_m$ was similar between the two (Figure 4.5B). While the most reasonable explanation for the diminished cytoplasmic response in the MICU2 KO cells is enhanced mitochondrial buffering, as predicted by our model, it is possible that it was due to

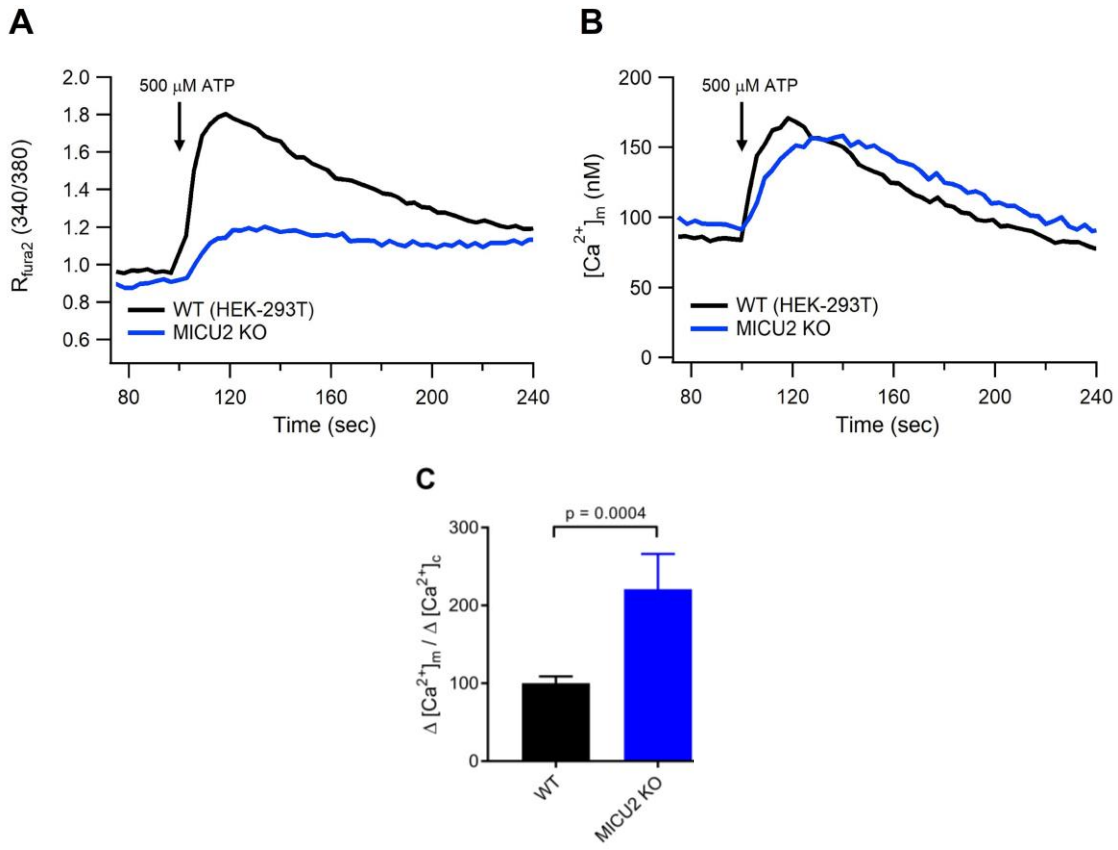

Figure 4.5. The cell physiological role of MICU2 in spatially restricting mitochondrial Ca^{2+} uptake

(see Chapter 2 Methods and Materials) (**A-B**) Simultaneous measurements of $[Ca^{2+}]_c$ (A) and $[Ca^{2+}]_m$ (B) in intact WT and MICU2 KO cells in response to 500 μM ATP. Traces representative of n = 5 independent experiments for each condition. MICU2 KO cells exhibit similar transient increase in $[Ca^{2+}]_m$ to WT cells despite reduced global $[Ca^{2+}]_c$ increase. (**C**) Quantification of increase in $[Ca^{2+}]_m$ at peak of the transient divided by mean increase in $[Ca^{2+}]_c$ ($\Delta[Ca^{2+}]_m/\Delta[Ca^{2+}]_c$). Bars: mean +/- SEM. (*P* = 0.0004; Student's t-test). A larger proportion of ER-released Ca^{2+} enters mitochondria in MICU2 KO cells.

clonal differences in, for example, expression of purinergic receptors. Nevertheless, similar mitochondrial Ca^{2+} uptake in WT and MICU2 KO cells despite much lower $[Ca^{2+}]_c$ in the MICU2 KO cells (Figure 4.5C) is consistent with our prediction that more Ca^{2+} can be taken up by mitochondria lacking MICU2 because of a less stringent requirement for close spatial proximity between ER Ca^{2+} release sites and mitochondrial Ca^{2+} uptake sites (Figure 4.4). Future studies are necessary to determine if indeed the evolutionary imperative for MICU2 is to promote a stricter spatial proximity or Ca^{2+} crosstalk between ER and mitochondria, and to determine its physiological rationale.

Variable assembly of EMRE and MCU creates functional channels with distinct gatekeeping profiles

Based on the work described in Chapter 3, we propose that the human uniporter complex largely exists in association with fewer than 4 and more than 1 EMRE subunit, but complexes with 1, 2, 3, or 4 EMRE exhibit channel activity and full or partial MICU1/2-mediated gatekeeping. Moreover, the more EMRE subunits that associate with each MCU channel, the higher the $[Ca^{2+}]_c$ threshold required for channel activation.

MCU complexes with fewer than four EMRE subunits can assemble as fully-functional channels.

Mitochondria from MCU+EMRE cells, which exhibit ~10-fold higher expression of MCU relative to EMRE, took up Ca^{2+} at rates similar to WT cells at $[Ca^{2+}]_c$ above 5 μM (Figures 3.1 & 3.4). Furthermore, MCU-EMRE concatemers that form channels with less than four EMRE subunits were functional (Figure 3.15). If only channels with four EMRE were functional, the gatekeeping profile in the MCU+P76I-EMRE+MICU1 cells would be the same as cells expressing ME[P76I], which was not observed. While BN-PAGE revealed that higher-order MCU oligomers (e.g. MCU hexamers or octamers containing excess MCU subunits that do not contribute to pore formation) were present in mitochondria expressing the MME or MMME concatemers (Figure 3.16), bands corresponding to MCU tetramers with one or two EMRE subunits (250-550 kDa) predominated. Thus, under circumstances where endogenous EMRE expression is insufficient to occupy all four binding sites in each channel, complexes with fewer than four EMREs retain full channel activity when the gatekeeping threshold is exceeded. Thus, we conclude that the MCU complex will form with a 1:1 EMRE:MCU stoichiometry if sufficient EMRE is present, but it is more likely that a range of possible stoichiometries is possible (Figure 4.6).

The endogenous MCU channel in HEK-293T cells likely contains two EMRE subunits. No differences in the $[Ca^{2+}]_c$-dependence of MCU activity or in the steady-state $[Ca^{2+}]_c$ gatekeeping threshold were observed between channels with two EMRE subunits (MEKO+MME+MICU1) and WT cells (Figure 3.15), suggesting that these channels recapitulate the stoichiometry of

endogenous channels. Of note however, the functional profile of cells expressing the MMME concatemer, which are predicted to form channels containing a single EMRE subunit, were functionally indistinguishable from MEKO+MME+MICU1 (or WT) cells. This could be attributed to formation of higher-order oligomers in the MMME-expressing cells (Figure 3.16) that created channels containing more than one EMRE, as depicted in Figure 3.12D. The $[Ca^{2+}]_c$ threshold for MCU activity in these cells likely arises from channels with one or two EMRE subunits.

BN-PAGE analyses also suggest that endogenous complexes in HEK-293T cells contain greater than one and less than four EMRE per channel (Figure 3.16). The size of complexes between 250-550 kDa depended on the number of EMRE subunits per channel, and not on incorporation of MICU proteins as they were not present in the complexes. Importantly, channels formed by expression of MME concatemers were not different in size from those in WT cells, while complexes containing a single EMRE were significantly smaller. Thus, the size of the native complex in WT cells is consistent with a channel complex containing two EMRE subunits bound to each MCU tetramer. The rapid degradation of unassociated EMRE subunits by mAAA proteases (König et al., 2016)(Tsai et al., 2017), along with our findings that the EMRE [P76I] mutation is required to prevent degradation of EMRE from the ME concatemer (Figure 3.13A), are consistent with the hypothesis that channels with four EMRE subunits may be rare *in vivo*.

The gatekeeping-threshold $[Ca^{2+}]_c$ increases with the number of EMRE subunits per channel

The second major conclusion of Chapter 3 is that MCU channels containing more EMRE subunits have enhanced gatekeeping (Figure 4.6). The EMRE [P76I] mutation increased the steady-state expression of EMRE without affecting MCU expression (Figures 3.10 & 3.11). Therefore, any differences in channel function and regulation between MCU+EMRE+MICU1 and MCU+P76I-EMRE+MICU1 cells were due solely to the elevated EMRE:MCU ratio in the P76I-EMRE cells. Both cell lines showed similar uptake rates and cooperativity of channel activation, but the right-shift in plots of initial-uptake rate vs. $[Ca^{2+}]_c$ and the elevated gatekeeping threshold in MCU+P76I-EMRE+MICU1 cells indicate that MICU1/2-mediated gatekeeping in channels with

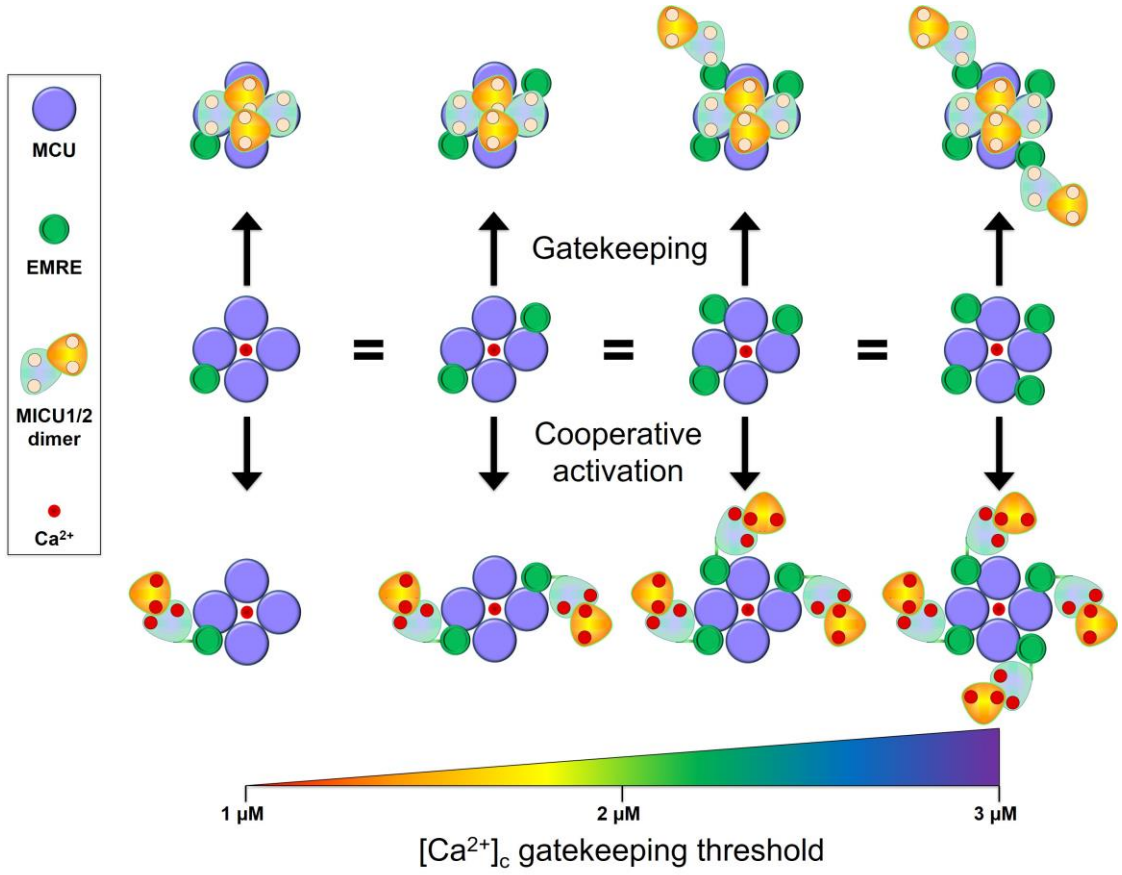

Figure 4.6. Proposed functional stoichiometry of the uniporter complex

MCU complexes with fewer than four EMRE subunits can assemble as fully-functional channels, but channels containing more EMRE subunits tether additional MICU1/2-dimers to the channel and enhance gatekeeping

three or four EMRE is enhanced compared with those associated with only one or two. These findings are reinforced by the functional profile of the ME[P76I] concatemer, in which all channels are predicted to contain 4 EMRE (Figures 3.14B & 3.15). Like MCU+P76I-EMRE+MICU1 cells, ME[P76I]+MICU1 cells showed a right-shift in the Ca^{2+}-uptake rate vs. initial $[Ca^{2+}]_c$ relationship and an elevated gatekeeping threshold compared with WT+MICU1 cells, with no difference in uptake rate and cooperative activation.

These findings are relevant in light of the recent structure of human MCU that revealed four EMRE subunits bound to the MCU tetramer. We confirmed here that such a channel is functional with intact MICU1/2-mediated gatekeeping. Our results provide further evidence that EMRE performs two independent roles in MCU-channel regulation. First, it allows MCU to adopt

an open channel conformation upon binding of only a single EMRE. In contrast, its role in tethering MICU1/2 to the complex to mediate channel gatekeeping is modulated by the number of EMRE subunits per channel. Such a phenomenon is not unique, as demonstrated by the functional modulation of BK channels by auxiliary subunits γ1 and β (Gonzalez-Perez et al., 2018). Similar to the role of EMRE in MCU activation, γ1 has been described as having an "all-or-none" effect of the voltage-dependence of BK channel gating, in which a single subunit associating with the pore forming subunits is sufficient to promote the full effect. On the other hand, each β-subunit that associates with the BK tetramer leads to an incremental shift in the voltage-dependence of channel gating such that the full shift is observed only when four β-subunits are present in the channel complex. This is also reminiscent of the functional stoichiometry of channel inactivation in the *Drosophila* voltage-gated potassium (K_v) channel Shaker, which assembles as a homotetramer (MacKinnon et al., 1993). The N-terminus of the channel contains a "ball and chain" domain that acts as a gate to mediate (N-type) channel inactivation (i.e. spontaneous closing following voltage-dependent activation). Incorporation of a single functional gate is necessary and sufficient to inhibit the channel, but the presence additional gates increases the rate at which inactivation occurs. This is analogous to our finding that a single EMRE subunit per MCU channel is sufficient to reconstitute gatekeeping (provided MICU1 expression is high enough to occupy all channels), while the presence of additional EMRE subunits enhances gatekeeping by elevating the $[Ca^{2+}]_c$ threshold required for channel activity. It is possible that this enhanced gatekeeping arises from an increase in the rate at which apo-MICU1 re-establishes its inhibitory interactions with the MCU pore in channels containing four EMRE subunits compared to those with fewer, but this conclusion requires detailed kinetic measurements of the relevant kinetic process beyond the scope of this work.

Our studies suggest that the endogenous MCU channel complex in HEK-293T cells likely contains four MCU monomers assembling as a tetramer that, on average, associates with two or three EMRE subunits. We predict therefore that under resting $[Ca^{2+}]_c$, two apo-MICU1/2 dimers associate with the complex through interactions with the C-terminus of EMRE and residues in two

MCU subunits (Figure 4.6), mediating inhibition of the channel (i.e. gatekeeping). When the local $[Ca^{2+}]_c$ becomes elevated, Ca^{2+}-binding to the EF hands of MICU1 and 2 promote dissociation of MICU1 from the pore and relieve MCU inhibition. Under these conditions, the role of EMRE in tethering MICU1/2 dimers to the complex is essential to ensure that gatekeeping is re-established quickly enough to ensure that channel activity ceases at the proper $[Ca^{2+}]_c$ threshold after uptake has occurred. Future work to address the structure of MCU channels with fewer than four EMRE subunits, and in the presence of MICU1/2 dimers is necessary to confirm this hypothesis. Nevertheless, it does help to explain the recent finding from our lab (Emily Fernandez Garcia - unpublished data) that ~80% knockdown of *EMRE* mRNA expression (EMRE KD) has no effect on Ca^{2+} uptake by mitochondria in HEK-293T cells (Figure 4.7). *EMRE* mRNA levels may not accurately reflect the steady-state protein expression due to the rapid turnover of EMRE by mAAA proteases. Thus, 80% KD of *EMRE* may not be sufficient to reduce the endogenous EMRE:MCU protein expression ratio to levels at which gatekeeping is affected (e.g. MCU+EMRE cells; EMRE:MCU ~1:10). To obtain direct evidence for this it would be necessary to accurately quantify the relative, steady-state protein expression of endogenous EMRE and MCU, a measurement which is difficult using standard biochemical approaches.

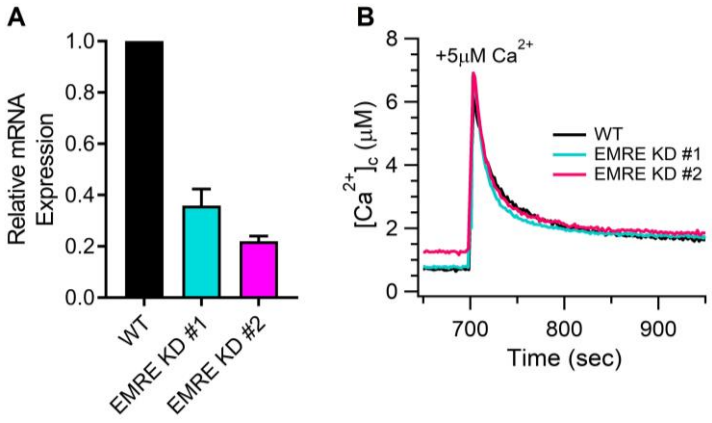

Figure 4.7. Ca^{2+} uptake in EMRE KD cells is no different from WT (adapted from Fernandez Garcia, E. – unpublished)

(A) Quantification of relative EMRE mRNA expression in WT +/- stable shRNA-mediated genetic KD of EMRE (qPCR performed by E.F.G.). Relative mRNA expression was calculated by normalizing ΔΔCT values for EMRE KD cells to ΔΔC values for WT cells. Bars: mean; error bars: SEM for n = 3 independent experiments. **(B)** Mitochondrial Ca^{2+}-uptake in suspensions of permeabilized WT (black trace) or two clones of stable EMRE KD cells in response to acute 5 μM increases of $[Ca^{2+}]_c$. Traces are representative of n = 3 independent experiments.

Outstanding questions and future directions

Despite the many recent advances regarding the structure and function of the uniporter and its role in mitochondrial physiology and disease, numerous outstanding questions remain. The work described here highlights gaps in in our understanding as to the molecular basis of MCU channel regulation, which present opportunities for future work regarding the role of mitochondrial Ca^{2+} transport in cell physiology.

Pathophysiology of loss-of-function mutations in MICU1

Here we have, for the first time, quantified the steady state $[Ca^{2+}]_m$ in cells lacking MICU1 as ~300-400 nM compared with ~100 nM in WT cells. These observations corroborate those in fibroblasts from patients with genetic defects in *MICU1* that result in absence of MICU1 expression (Bhosale et al., 2017). Perhaps surprisingly, the increase in $[Ca^{2+}]_m$ by 200-300 nM we observed is not excessively high, suggesting that mitochondria in MICU1 KO cells may not be as Ca^{2+} over-loaded as has been inferred (Mallilankaraman et al., 2012a)(Logan et al., 2013)(Antony et al., 2016)(Liu et al., 2016)(Bhosale et al., 2017). Several mechanisms could account for why $[Ca^{2+}]_m$ is not elevated to much higher levels. It is possible that NCLX-mediated Ca^{2+}-extrusion can compensate for uninhibited influx through MCU, or that MCU is inhibited by elevated $[Ca^{2+}]_m$, limiting Ca^{2+} uptake. Moreover, measurements of $[Ca^{2+}]_m$ may not reflect total matrix Ca^{2+} content. However, mitochondrial Ca^{2+} content in hepatocytes (Antony et al., 2016) and brains (Liu et al., 2016) of mice with MICU1 constitutively deleted were either not different or increased by only 50%, respectively, compared with normal cells. Nevertheless, pathogenesis in MICU1 KO animals has been attributed to mitochondrial Ca^{2+} overload (Liu et al., 2016). The relatively modest matrix free-Ca^{2+} elevation under resting conditions may not be the (sole) cause of disease pathogenesis in animal models (Antony et al., 2016)(Liu et al., 2016) and patients (Logan et al., 2013)(Lewis-Smith et al., 2016)(Bhosale et al., 2017). Rather, pathogenesis in neuronal tissue and striated muscle might be caused by sensitized gain-of-function responses to transient increases in $[Ca^{2+}]_c$ up to the normal threshold of ~1.3 µM, an inability of mitochondria to properly

buffer cytoplasmic Ca^{2+} signals due to a loss of cooperative channel activation, or reduced ATP production.

This raises the question of whether the phenotypes observed in humans and animals lacking MICU1 are consistent with those expected from mitochondrial Ca^{2+} overload. One might expect that elevated $[Ca^{2+}]_m$ could lead to opening of the mPTP, triggering mitochondrial depolarization that in turn leads to an increase in excessive mitophagy and/or Ca^{2+}-induced cell death. We have obtained conflicting results regarding the resting $\Delta\Psi_m$ in MICU1 KO (HEK293T) cells; there is a partial (25-40%) decrease compared to WT cells when measured with TMRE (Figure 2.6B), but no difference in measurements using JC-1 (Figure 2.7A-B insets). Moreover, fibroblasts from patients with loss-of-function mutations in *MICU1* (ΔMICU1) showed no differences in Ca^{2+}-induced cell death, mitochondrial ROS production, or mitophagic flux (Bhosale et al., 2017). Nevertheless, the mitochondrial network appears fragmented in ΔMICU1 fibroblasts, indicating an imbalance between fission and fusion (Logan et al., 2013). This led to the hypothesis that disease results from a bioenergetic deficiency arising from a futile cycling of Ca^{2+} across the IMM.

In this model, Bhosale et al. (2017) propose that constitutively elevated $[Ca^{2+}]_m$ (due to a lack of MCU gatekeeping) leads to excessive NCLX-mediated Ca^{2+} efflux, which in turn elevates resting matrix $[Na^+]$. To maintain ion homeostasis, Na^+ efflux is mediated through an electroneutral H^+-coupled antiport mechanism, which reduces the proton-motive force (but not necessarily $\Delta\Psi_m$ - see Chapter 1, P. 23) that drives ATP synthesis. This hypothesis is in line with the finding that NAD(P)H levels were elevated in mitochondria from ΔMICU1 fibroblasts (Logan et al., 2013), suggesting reduced activity of the entire respiratory chain (CI-CV) despite the likely increase in TCA-cycle flux due to elevated $[Ca^{2+}]_m$. However, Bhosale's model presumes the existence of an unknown mitochondrial Na^+/H^+ exchanger (mNHE) that mediates the antiport of Na^+ and H^+ ions across the IMM (for review see Brierley (1976)). The evidence for such a mechanism is summarized in an excerpt from a review by Crompton et al. (1978), as follows:

"There is considerable evidence for the existence of a carrier that catalyses an exchange between Na^+ and H^+ across the inner membrane of liver and heart mitochondria (sic). The existence of this system was investigated with mitochondria that exhibit Na^+-induced efflux of Ca^{2+}. In all cases, the mitochondria were observed to swell rapidly when introduced into iso-osmotic sodium acetate, and to swell little in potassium acetate... This behaviour is explicable in terms of Na^+ entry in exchange for H^+ and entry of acetate as the undissociated acid."

Crompton and Heid (1978), also showed that the mNHE is likely distinct from the mitochondrial Na^+/Ca^{2+} exchanger (NCLX). This is based on the observation that while addition of (2.5 mM) Na^+ to suspensions of isolated heart mitochondria induces an efflux of Ca^{2+} that reaches a steady state after ~15 minutes, a rapid (occurring within seconds) influx of H^+ is observed immediately after Na^+ addition, the latter attributed to the mNHE. A later review described the mNHE as responsible for "(a)n apparently unregulated Na^+/H^+ antiport (that) keeps matrix $[Na^+]$ low and the Na^+-gradient equal to the H^+-gradient." (Brierley et al., 1994). Despite the preponderance of physiological evidence for the mNHE, there remains a lack of genetic evidence for existence. Initially, the human mNHE was thought to be the protein NHE6 based on its abundance in "mitochondrion-rich tissues" and its apparent localization to mitochondria when fused to GFP and overexpressed in HeLa cells (Numata et al., 1998). These findings were later contradicted by Miyazaki et al. (2001), who showed that NHE6 localized to the ER and plasma membrane. NHE6 also contained an N-terminal signal peptide and endoglycosidase-H resistant carbohydrate moieties, leading to the conclusion that the protein was targeted to the ER membrane and transported to the plasma membrane by the canonical secretory pathway. Due to the conflicting evidence, the molecular identity of the human mNHE - or whether such an entity even exists - remains unclear. It is also possible that the bioenergetic deficiency in ΔMICU1 patients is not due to a reduction in mitochondrial ATP production *per se*, but rather to insufficient sequestration of cytoplasmic Ca^{2+} by mitochondria in response to transient elevations in $[Ca^{2+}]_c$ that normally induce cooperative activation of MCU (Perocchi et al., 2010). The need to compensate for this constitutive increase in $[Ca^{2+}]_c$ would require additional energy expenditure by SERCA or the plasma membrane CaATPase, ultimately resulting in a global ATP deficiency in cells.

The relationship between MICU1/2-mediated gatekeeping and cooperative channel activation

The dual role of MICU1 in both gatekeeping (i.e. inhibition at low $[Ca^{2+}]_c$) and cooperative activation of the channel has been the subject of much debate. Despite being widely accepted as the "fundamental gatekeeper" of MCU, MICU1 was originally identified in a screen for genes that were required for Ca^{2+} uptake (Perocchi et al., 2010). Moreover, we and others have confirmed that Ca^{2+} -flux into mitochondria is impaired in MICU1 KO cells at higher $[Ca^{2+}]_c$, suggesting that cooperative activation of the channel is not simply a 'relief of gatekeeping". Additionally, the apparent "uncoupling" of gatekeeping and cooperative activation in MCU+EMRE cells (see Chapter 3 – P. 65) suggests that they represent distinct mechanisms of channel regulation. In addition, it is unclear whether either mechanism involves a direct modulation of channel open probability (P_o) by MICU1 and or 2. The maximal MCU current densities in mitoplast patch-clamp experiments are no different in the presence or absence of MICU1 (Vais et al., 2016), despite the fact that these assays are performed under conditions where the cytoplasmic (bath) $[Ca^{2+}]$ (0.1 – 1 mM) far exceeds the level required for cooperative activation. Moreover, similar experiments in the presence of MICU1 or MICU2 EF-hand mutants show no constitutive suppression of MCU currents relative to those in the presence or absence of (WT) MICU1 (Horia Vais, Ph.D. - unpublished data), suggesting that gatekeeping itself may not be as simple as the "lid" mechanism mediated by direct binding of MICU1 to the channel pore (Paillard et al., 2018)(Phillips et al., 2019). That being said, $[Ca^{2+}]_m$ does appear to modulate the channel P_o under certain conditions, through a mechanism that requires the presence of both MICU1 and 2 (Vais et al., 2016 - see below).

These findings have important implications regarding the role of MICU1 (and 2) in regulating mitochondrial Ca^{2+}-uptake and suggest that gatekeeping and/or cooperative activation may represent indirect mechanisms that pertain only to Ca^{2+} -flux measurements across the IMM rather than to direct modulation of channel activity. This idea is supported by a number of findings: First, MICU1 has been shown to interact with the mitochondrial Mg-ATP/P_i transporter

(SLC25A23) (Hoffman et al., 2014) and thus could modulate MCU activity by affecting counter-ion (P_i) transport. Additionally, MICU1 has been implicated as a regulator of cristae structure and function (Gottschalk et al., 2019), which could indirectly affect MCU channel assembly or activity. Finally, a recent study found that in *Drosophila*, *MICU1* loss-of-function mutations were lethal, but that this phenotype was not rescued in the absence of MCU or EMRE (Tufi et al., 2019), suggesting that lethality was not due to excessive MCU activity. Future work is necessary to reconcile the discrepancies between Ca^{2+}-flux measurements and electrophysiological approaches, and ultimately elucidate the molecular mechanisms by which MICU proteins regulate mitochondrial Ca^{2+} uptake.

Other modes of uniporter regulation

In addition to regulation by Ca^{2+}-binding to MICU1/2 and variable assembly of EMRE and MCU, channel activity is modulated by post-translational modification of components of the uniporter complex. Akt-mediated phosphorylation of S124 in MICU1 has been shown to increase resting $[Ca^{2+}]_m$ in HeLa cells and enhance mitochondrial Ca^{2+} uptake in response to intracellular Ca^{2+} signals (Marchi et al., 2019). This phenotype, which resembles that of MICU1 KO (HEK-293T) cells, suggests that phosphorylation of S124 represents a mechanism to enhance MCU activity in response to Akt activation by relieving MICU1/2-mediated gatekeeping. In addition, MCU can be phosphorylated at S57 by AMP kinase, increasing mitochondrial Ca^{2+} uptake by in histamine-stimulated HeLa cells and promoting mitotic progression (Zhao et al., 2019). While it is unclear whether this enhancement in channel activity is due to an increase in open probability, number of functional complexes, or a relief of gatekeeping, it again suggests that phosphorylation is an important mechanism for regulating Ca^{2+} uptake in response to the dynamic energy requirements of cells. Other than phosphorylation, oxidation of MCU C97 in the presence of high ROS levels in the matrix has been to promote the formation of higher-order oligomers and enhance Ca^{2+} uptake in human pulmonary microvascular endothelial cells (Dong et al., 2017). Moreover, given the unique milieu of proteins, metabolites and ions in the matrix it is possible that

post-translational modifications to MCU or EMRE such as acetylation or succinylation represent additional modes of regulation.

Aside from post-translational modification of the uniporter complex, recent structures of the NTD of human MCU identified a putative divalent-ion binding site, which was proposed to modulate assembly and subsequently function of the channel complex (Lee et al., 2016). This is particularly interesting in light of work from our lab describing a novel phenomenon, $[Ca^{2+}]_m$-dependent regulation of MCU activity (Vais et al., 2016). We measured whole-mitoplast Ca^{2+} currents using patch-clamp electrophysiology and observed a distinct bi-phasic dependence on $[Ca^{2+}]_m$ (Figure 4.7), that required the presence of MICU1 and 2 on the opposite side of the inner membrane. Interestingly, peak-inhibition occurred at ~400 nM $[Ca^{2+}]_m$, similar to the resting $[Ca^{2+}]_m$ in MICU1 KO cells. Our discovery prompts a revision of the current model for MCU activity that includes $[Ca^{2+}]$ sensing on both sides of the IMM. How these signals are integrated to govern channel activity is still unknown. Originally, our results suggested that EMRE was a $[Ca^{2+}]_m$ sensor that mediated this novel form of regulation, but the now generally-accepted membrane topology of EMRE and its lack of putative Ca^{2+}-binding sites imply that additional sites may be involved, possibly in the MCU protein itself. We are currently working to verify the presence of divalent cation-binding sites in the NTD of MCU, as well as determine their role in

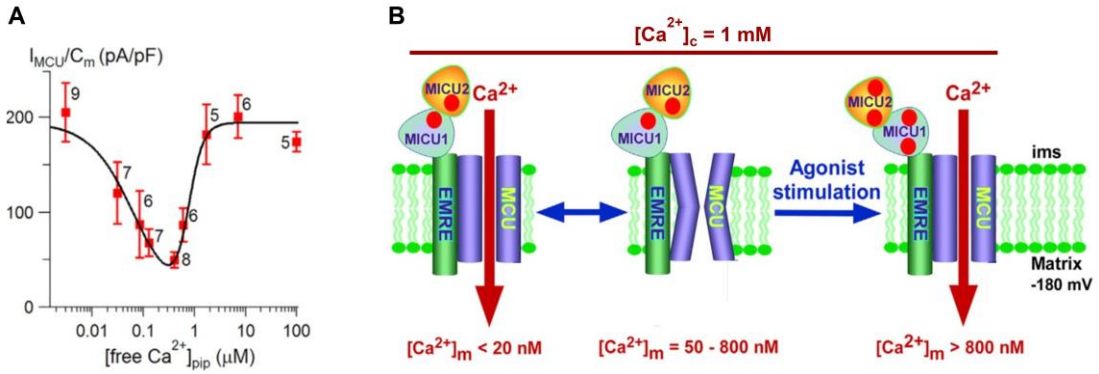

Figure 4.8. MCU channel activity is modulated by a mechanism dependent upon matrix $[Ca^{2+}]$ (adapted from Vais et al., 2016)

(A) Response of MCU Ca^{2+}-current density at V_m = -160 mV, with 1 mM Ca^{2+} in the bath, as function of free $[Ca^{2+}]$ in pipette (matrix) solution ($[Ca^{2+}]_m$). Data are fitted with a biphasic Hill equation (continuous line). **(B)** $[Ca^{2+}]_m$ between 50 – 800 nM inhibit channel activity even at $[Ca^{2+}]_c$ that promote MICU1/2-mediated cooperative activation.

$[Ca^{2+}]_m$-regulation of channel activity. It is also possible that Ca^{2+} binding to MCU directly is not involved in the $[Ca^{2+}]_m$ regulation of channel activity. In this case, additional Ca^{2+}-binding proteins in the mitochondrial matrix must be identified. Alternatively, this unidentified $[Ca^{2+}]_m$ sensor could not be a protein at all, but rather another molecule in the mitochondrial matrix that associates with MCU and modulates its function. Interestingly, cardiolipin, a lipid component of the IMM, is known to bind to Ca^{2+} with an apparent K_D similar to that of the half maximal effective concentration (~800 nM) for MCU activation by $[Ca^{2+}]_m$ (Kamer et al., 2017). Hopefully, in the near future, these approaches will identify the mechanisms by which coupled $[Ca^{2+}]_m$- and $[Ca^{2+}]_c$ -mediated regulatory mechanisms control MCU channel activity.

If mitochondria are a cell within a cell, then the processes I've described in this work constitute its action potential. The resting membrane potential is set by activity of the respiratory complex rather than channel-mediated diffusion of K^+. External stimuli trigger depolarization through voltage-gated Na+-channels in the plasma membrane and MCU in the IMM, which is followed by a repolarization phase due to increased K+ permeability in cells and increased electron flux through CI-CV in mitochondria. These events culminate in the rapid transmission of signals, both electrical and chemical, that ultimately bestow humans with the ability to rapidly respond to dynamic changes in our environment. I hope that this work will inform future discoveries that build our understanding of the myriad roles of mitochondria in sustaining cellular energetics and homeostasis, as well as provide insight into new therapies targeting dysregulated mitochondrial Ca^{2+} uptake in human disease.

APPENDICES

Appendix A: Amino acid sequences encoded by cDNAs used in all studies

1. Human EMRE (C-terminal V5 tag):
MASGAARWLVLAPVRSGALRSGPSLRKDGDVSAAWSGSGRSLVPSRSVIVTRSGAILPKPVKM
SFGLLRVFSIVIPFLYVGTLISKNFAALLEEHDIFVPEDDDDDDGKPIPNPLLGLDST

2. Human EMRE [P76I] (C-terminal V5 tag):
MASGAARWLVLAPVRSGALRSGPSLRKDGDVSAAWSGSGRSLVPSRSVIVTRSGAILPKPVKM
SFGLLRVFSIVIIFLYVGTLISKNFAALLEEHDIFVPEDDDDDDGKPIPNPLLGLDST

3. Human MCU (C-terminal V5-(6x)His tag):
MAAAAGRSLLLLLSSRGGGGGGAGGCGALTAGCFPGLGVSRHRQQQHHRTVHQRIASWQNLG
AVYCSTVVPSDDVTVVYQNGLPVISVRLPSRRERCQFTLKPISDSVGVFLRQLQEEDRGIDRVAI
YSPDGVRVAASTGIDLLLLDDFKLVINDLTYHVRPPKRDLLSHENAATLNDVKTLVQQLYTTLCIE
QHQLNKERELIERLEDLKEQLAPLEKVRIEISRKAEKRTTLVLWGGLAYMATQFGILARLTWWEY
SWDIMEPVTYFITYGSAMAMYAYFVMTRQEYVYPEARDRQYLLFFHKGAKKSRFDLEKYNQLKD
AIAQAEMDLKRLRDPLQVHLPLRQIGEKDCPTFLYKVVDLEGPRFEGKPIPNPLLGLDSTRTGHH
HHHH

4. Human MICU1 (C-terminal Myc-Flag tag):
MFRLNSLSALAELAVGSRWYHGGSQPIQIRRRLMMVAFLGASAVTASTGLLWKRAHAESPPCV
DNLKSDIGDKGKNKDEGDVCNHEKKTADLAPHPEEKKKKRSGFRDRKVMEYENRIRAYSTPDKI
FRYFATLKVISEPGEAEVFMTPEDFVRSITPNEKQPEHLGLDQYIIKRFDGKKISQEREKFADEGSI
FYTLGECGLISFSDYIFLTTVLSTPQRNFEIAFKMFDLNGDGEVDMEEFEQVQSIIRSQTSMGMRH
RDRPTTGNTLKSGLCSALTTYFFGADLKGKLTIKNFLEFQRKLQHDVLKLEFERHDPVDGRITER
QFGGMLLAYSGVQSKKLTAMQRQLKKHFKEGKGLTFQEVENFFTFLKNINDVDTALSFYHMAGA
SLDKVTMQQVARTVAKVELSDHVCDVVFALFDCDGNGELSNKEFVSIMKQRLMRGLEKPKDMG
FTRLMQAMWKCAQETAWDFALPKQTRTRPLEQKLISEEDLAANDILDYKDDDDK

5. Human MICU2 (no tag):
MAAAAGSCARVAAWGGKLRRGLAVSRQAVRSPGPLAAAVAGAALAGAGAAWHHSRVSVAAR
DGSFTVSAQKNVEHGIIYIGKPSLRKQRFMQFSSLEHEGEYYMTPRDFLFSVMFEQMERKTSVK
KLTKKDIEDTLSGIQTAGCGSTFFRDLGDKGLISYTEYLFLLTILTKPHSGFHVAFKMLDTDGNEMI
EKREFFKLQKIISKQDDLMTVKTNETGYQEAIVKEPEINTTLQMRFFGKRGQRKLHYKEFRRFME
NLQTEIQEMEFLQFSKGLSFMRKEDFAEWLLFFTNTENKDIYWKNVREKLSAGESISLDEFKSFC
HFTTHLEDFAIAMQMFSLAHRPVRLAEFKRAVKVATGQELSNNILDTVFKIFDLDGDECLSHEEFL
GVLKNRMHRGLWVPQHQSIQEYWKCVKKESIKGVKEVWKQAGKGLFTRTRPLEV

6. Human MICU2 (C-terminal Myc-Flag tag):
MAAAAGSCARVAAWGGKLRRGLAVSRQAVRSPGPLAAAVAGAALAGAGAAWHHSRVSVAAR
DGSFTVSAQKNVEHGIIYIGKPSLRKQRFMQFSSLEHEGEYYMTPRDFLFSVMFEQMERKTSVK
KLTKKDIEDTLSGIQTAGCGSTFFRDLGDKGLISYTEYLFLLTILTKPHSGFHVAFKMLDTDGNEMI
EKREFFKLQKIISKQDDLMTVKTNETGYQEAIVKEPEINTTLQMRFFGKRGQRKLHYKEFRRFME
NLQTEIQEMEFLQFSKGLSFMRKEDFAEWLLFFTNTENKDIYWKNVREKLSAGESISLDEFKSFC
HFTTHLEDFAIAMQMFSLAHRPVRLAEFKRAVKVATGQELSNNILDTVFKIFDLDGDECLSHEEFL
GVLKNRMHRGLWVPQHQSIQEYWKCVKKESIKGVKEVWKQAGKGLFTRTRPLEQKLISEEDLA
ANDILDYKDDDDK

7. MCU-EMRE concatemer (C-terminal V5 tag):
MAAAAGRSLLLLLSSRGGGGGGAGGCGALTAGCFPGLGVSRHRQQQHHRTVHQRIASWQNLG
AVYCSTVVPSDDVTVVYQNGLPVISVRLPSRRERCQFTLKPISDSVGVFLRQLQEEDRGIDRVAI
YSPDGVRVAASTGIDLLLLDDFKLVINDLTYHVRPPKRDLLSHENAATLNDVKTLVQQLYTTLCIE
QHQLNKERELIERLEDLKEQLAPLEKVRIEISRKAEKRTTLVLWGGLAYMATQFGILARLTWWEY
SWDIMEPVTYFITYGSAMAMYAYFVMTRQEYVYPEARDRQYLLFFHKGAKKSRFDLEKYNQLKD
AIAQAEMDLKRLRDPLQVHLPLRQIGEKDVSAAWSGSGRSLVPSRSVIVTRSGAILPKPVKMSFG
LLRVFSIVIPFLYVGTLISKNFAALLEEHDIFVPEDDDDDDGKPIPNPLLGLDST

8. MCU-EMRE [P76I] concatemer (C-terminal V5 tag):
MAAAAGRSLLLLLSSRGGGGGGAGGCGALTAGCFPGLGVSRHRQQQHHRTVHQRIASWQNLG
AVYCSTVVPSDDVTVVYQNGLPVISVRLPSRRERCQFTLKPISDSVGVFLRQLQEEDRGIDRVAI
YSPDGVRVAASTGIDLLLLDDFKLVINDLTYHVRPPKRDLLSHENAATLNDVKTLVQQLYTTLCIE
QHQLNKERELIERLEDLKEQLAPLEKVRIEISRKAEKRTTLVLWGGLAYMATQFGILARLTWWEY
SWDIMEPVTYFITYGSAMAMYAYFVMTRQEYVYPEARDRQYLLFFHKGAKKSRFDLEKYNQLKD
AIAQAEMDLKRLRDPLQVHLPLRQIGEKDVSAAWSGSGRSLVPSRSVIVTRSGAILPKPVKMSFG
LLRVFSIVIIFLYVGTLISKNFAALLEEHDIFVPEDDDDDDGKPIPNPLLGLDST

9. MCU-MCU-EMRE [P76I] concatemer (C-terminal V5-tag):
MAAAAGRSLLLLLSSRGGGGGGAGGCGALTAGCFPGLGVSRHRQQQHHRTVHQRIASWQNLG
AVYCSTVVPSDDVTVVYQNGLPVISVRLPSRRERCQFTLKPISDSVGVFLRQLQEEDRGIDRVAI
YSPDGVRVAASTGIDLLLLDDFKLVINDLTYHVRPPKRDLLSHENAATLNDVKTLVQQLYTTLCIE
QHQLNKERELIERLEDLKEQLAPLEKVRIEISRKAEKRTTLVLWGGLAYMATQFGILARLTWWEY
SWDIMEPVTYFITYGSAMAMYAYFVMTRQEYVYPEARDRQYLLFFHKGAKKSRFDLEKYNQLKD
AIAQAEMDLKRLRDPLQVHLPLRQIGEKDASGGSGGGSGGGSGVHQRIASWQNLGAVYCSTVV
PSDDVTVVYQNGLPVISVRLPSRRERCQFTLKPISDSVGVFLRQLQEEDRGIDRVAIYSPDGVRV
AASTGIDLLLLDDFKLVINDLTYHVRPPKRDLLSHENAATLNDVKTLVQQLYTTLCIEQHQLNKERE
LIERLEDLKEQLAPLEKVRIEISRKAEKRTTLVLWGGLAYMATQFGILARLTWWEYSWDIMEPVTY
FITYGSAMAMYAYFVMTRQEYVYPEARDRQYLLFFHKGAKKSRFDLEKYNQLKDAIAQAEMDLK
RLRDPLQVHLPLRQIGEKDVSAAWSGSGRSLVPSRSVIVTRSGAILPKPVKMSFGLLRVFSIVIIFL
YVGTLISKNFAALLEEHDIFVPEDDDDDDGKPIPNPLLGLDST

10. MCU-MCU-MCU-EMRE [P76I] concatemer (C-terminal V5-tag):
MAAAAGRSLLLLLSSRGGGGGGAGGCGALTAGCFPGLGVSRHRQQQHHRTVHQRIASWQNLG
AVYCSTVVPSDDVTVVYQNGLPVISVRLPSRRERCQFTLKPISDSVGVFLRQLQEEDRGIDRVAI
YSPDGVRVAASTGIDLLLLDDFKLVINDLTYHVRPPKRDLLSHENAATLNDVKTLVQQLYTTLCIE
QHQLNKERELIERLEDLKEQLAPLEKVRIEISRKAEKRTTLVLWGGLAYMATQFGILARLTWWEY
SWDIMEPVTYFITYGSAMAMYAYFVMTRQEYVYPEARDRQYLLFFHKGAKKSRFDLEKYNQLKD
AIAQAEMDLKRLRDPLQVHLPLRQIGEKDASGGSGGGSGGGSGVHQRIASWQNLGAVYCSTVVPS
DDVTVVYQNGLPVISVRLPSRRERCQFTLKPISDSVGVFLRQLQEEDRGIDRVAIYSPDGVRVAA
STGIDLLLLDDFKLVINDLTYHVRPPKRDLLSHENAATLNDVKTLVQQLYTTLCIEQHQLNKERELI
ERLEDLKEQLAPLEKVRIEISRKAEKRTTLVLWGGLAYMATQFGILARLTWWEYSWDIMEPVTYFI
TYGSAMAMYAYFVMTRQEYVYPEARDRQYLLFFHKGAKKSRFDLEKYNQLKDAIAQAEMDLKR
LRDPLQVHLPLRQIGEKDASGGSGGGSGGGSGVHQRIASWQNLGAVYCSTVVPSDDVTVVYQ
NGLPVISVRLPSRRERCQFTLKPISDSVGVFLRQLQEEDRGIDRVAIYSPDGVRVAASTGIDLLLL
DDFKLVINDLTYHVRPPKRDLLSHENAATLNDVKTLVQQLYTTLCIEQHQLNKERELIERLEDLKE
QLAPLEKVRIEISRKAEKRTTLVLWGGLAYMATQFGILARLTWWEYSWDIMEPVTYFITYGSAMA
MYAYFVMTRQEYVYPEARDRQYLLFFHKGAKKSRFDLEKYNQLKDAIAQAEMDLKRLRDPLQVH
LPLRQIGEKDVSAAWSGSGRSLVPSRSVIVTRSGAILPKPVKMSFGLLRVFSIVIIFLYVGTLISKNF
AALLEEHDIFVPEDDDDDDGKPIPNPLLGLDST

11. MCU-MCU-MCU-MCU-EMRE [P76I] concatemer (C-terminal V5-tag):
MAAAAGRSLLLLLSSRGGGGGGAGGCGALTAGCFPGLGVSRHRQQQHHRTVHQRIASWQNLG
AVYCSTVVPSDDVTVVYQNGLPVISVRLPSRRERCQFTLKPISDSVGVFLRQLQEEDRGIDRVAI

YSPDGVRVAASTGIDLLLLDDFKLVINDLTYHVRPPKRDLLSHENAATLNDVKTLVQQLYTTLCIE
QHQLNKERELIERLEDLKEQLAPLEKVRIEISRKAEKRTTLVLWGGLAYMATQFGILARLTWWEY
SWDIMEPVTYFITYGSAMAMYAYFVMTRQEYVYPEARDRQYLLFFHKGAKKSRFDLEKYNQLKD
AIAQAEMDLKRLRDPLQVHLPLRQIGEKDASGGSGGGSGGGVHQRIASWQNLGAVYCSTVVPS
DDVTVVYQNGLPVISVRLPSRRERCQFTLKPISDSVGVFLRQLQEEDRGIDRVAIYSPDGVRVAA
STGIDLLLLDDFKLVINDLTYHVRPPKRDLLSHENAATLNDVKTLVQQLYTTLCIEQHQLNKERELI
ERLEDLKEQLAPLEKVRIEISRKAEKRTTLVLWGGLAYMATQFGILARLTWWEYSWDIMEPVTYFI
TYGSAMAMYAYFVMTRQEYVYPEARDRQYLLFFHKGAKKSRFDLEKYNQLKDAIAQAEMDLKR
LRDPLQVHLPLRQIGEKDASGGSGGGSGGGVHQRIASWQNLGAVYCSTVVPSDDVTVVYQNGL
PVISVRLPSRRERCQFTLKPISDSVGVFLRQLQEEDRGIDRVAIYSPDGVRVAASTGIDLLLLDDF
KLVINDLTYHVRPPKRDLLSHENAATLNDVKTLVQQLYTTLCIEQHQLNKERELIERLEDLKEQLA
PLEKVRIEISRKAEKRTTLVLWGGLAYMATQFGILARLTWWEYSWDIMEPVTYFITYGSAMAMYA
YFVMTRQEYVYPEARDRQYLLFFHKGAKKSRFDLEKYNQLKDAIAQAEMDLKRLRDPLQVHLPL
RQIGEKDASGGSGGGSGGGSGVHQRIASWQNLGAVYCSTVVPSDDVTVVYQNGLPVISVRLPS
RRERCQFTLKPISDSVGVFLRQLQEEDRGIDRVAIYSPDGVRVAASTGIDLLLLDDFKLVINDLTYH
VRPPKRDLLSHENAATLNDVKTLVQQLYTTLCIEQHQLNKERELIERLEDLKEQLAPLEKVRIEISR
KAEKRTTLVLWGGLAYMATQFGILARLTWWEYSWDIMEPVTYFITYGSAMAMYAYFVMTRQEY
VYPEARDRQYLLFFHKGAKKSRFDLEKYNQLKDAIAQAEMDLKRLRDPLQVHLPLRQIGEKDVSA
AWSGSGRSLVPSRSVIVTRSGAILPKPVKMSFGLLRVFSIVIIFLYVGTLISKNFAALLEEHDIFVPE
DDDDDDGKPIPNPLLGLDST

Appendix B: R-script syntax for generating unique nucleotide sequences for a given protein sequence (Pagès et al., 2017)

```
library(Biostrings)
cds<- DNAString("<PASTE FASTA AMINO ACID SEQUENCE HERE>")
cds
c<-codons(cds)

#Shuffle 1
#Valine
c1a<-gsub("GTA", "GTG", c, perl=TRUE)
c2a<-gsub("GTC", "GTA", c1a, perl=TRUE)
c3a<-gsub("GTT", "GTC", c2a, perl=TRUE)
        #Histidine
c4a<-gsub("CAC", "CAT", c3a, perl=TRUE)
        #Glutamine
c5a<-gsub("CAG", "CAA", c4a, perl=TRUE)
        #Arginine
c6a<-gsub("AGA", "CGG", c5a, perl=TRUE)
c7a<-gsub("AGG", "AGA", c6a, perl=TRUE)
c8a<-gsub("CGT", "AGG", c7a, perl=TRUE)
c9a<-gsub("CGC", "CGT", c8a, perl=TRUE)
c10a<-gsub("CGA", "CGC", c9a, perl=TRUE)
        #Isoleucine
c11a<-gsub("ATC", "ATA", c10a, perl=TRUE)
c12a<-gsub("ATT", "ATC", c11a, perl=TRUE)
        #Alanine
c13a<-gsub("GCT", "GCA", c12a, perl=TRUE)
c14a<-gsub("GCC", "GCT", c13a, perl=TRUE)
c15a<-gsub("GCG", "GCC", c14a, perl=TRUE)
        #Asparagine
c16a<-gsub("AAT", "AAC", c15a, perl=TRUE)
        #Leucine
c17a<-gsub("TTG", "CTT", c16a, perl=TRUE)
c18a<-gsub("CTA", "TTG", c17a, perl=TRUE)
c19a<-gsub("CTG", "CTA", c18a, perl=TRUE)
c20a<-gsub("CTC", "CTG", c19a, perl=TRUE)
c21a<-gsub("TTA", "CTC", c20a, perl=TRUE)
        #Glycine
c22a<-gsub("GGA", "GGT", c21a, perl=TRUE)
c23a<-gsub("GGG", "GGA", c22a, perl=TRUE)
c24a<-gsub("GGC", "GGG", c23a, perl=TRUE)
        #Tyrosine
c25a<-gsub("TAT", "TAC", c24a, perl=TRUE)
        #Cysteine
c26a<-gsub("TGC", "TGT", c25a, perl=TRUE)
        #Serine
c27a<-gsub("AGC", "TCG", c26a, perl=TRUE)
c28a<-gsub("AGT", "AGC", c27a, perl=TRUE)
c29a<-gsub("TCC", "AGT", c28a, perl=TRUE)
c30a<-gsub("TCT", "TCC", c29a, perl=TRUE)
c31a<-gsub("TCA", "TCT", c30a, perl=TRUE)
        #Threonine
c32a<-gsub("ACT", "ACA", c31a, perl=TRUE)
c33a<-gsub("ACC", "ACT", c32a, perl=TRUE)
c34a<-gsub("ACG", "ACC", c33a, perl=TRUE)
        #Proline
c35a<-gsub("CCT", "CCA", c34a, perl=TRUE)
c36a<-gsub("CCC", "CCT", c35a, perl=TRUE)
c37a<-gsub("CCG", "CCC", c36a, perl=TRUE)
        #Aspartate
c38a<-gsub("GAT", "GAC", c37a, perl=TRUE)
        #Glutamate
c39a<-gsub("GAA", "GAG", c38a, perl=TRUE)
        #Phenylalanine
c40a<-gsub("TTC", "TTT", c39a, perl=TRUE)
```

```
            #Lysine
c41a<-gsub("AAG", "AAA", c40a, perl=TRUE)

#Switch 1
            #Valine
c0b<-gsub("GTA", "GTC", c41a, perl=TRUE)
c1b<-gsub("GTG", "GTT", c0b, perl=TRUE)
            #Histidine
c2b<-gsub("CAT", "CAC", c1b, perl=TRUE)
            #Glutamine
c3b<-gsub("CAA", "CAG", c2b, perl=TRUE)
            #Arginine
c4b<-gsub("CGG", "CGA", c3b, perl=TRUE)
            #Isoleucine
c5b<-gsub("ATA", "ATT", c4b, perl=TRUE)
            #Alanine
c6b<-gsub("GCA", "GCG", c5b, perl=TRUE)
            #Asparagine
c7b<-gsub("AAC", "AAT", c6b, perl=TRUE)
            #Leucine
c8b<-gsub("CTT", "TTA", c7b, perl=TRUE)
            #Glycine
c9b<-gsub("GGT", "GGC", c8b, perl=TRUE)
            #Tyrosine
c10b<-gsub("TAC", "TAT", c9b, perl=TRUE)
            #Cysteine
c11b<-gsub("TGT", "TGC", c10b, perl=TRUE)
            #Serine
c12b<-gsub("TCG", "TCA", c11b, perl=TRUE)
            #Threonine
c13b<-gsub("ACA", "ACG", c12b, perl=TRUE)
            #Proline
c14b<-gsub("CCA", "CCG", c13b, perl=TRUE)
            #Aspartate
c15b<-gsub("GAC", "GAT", c14b, perl=TRUE)
            #Glutamate
c16b<-gsub("GAG", "GAA", c15b, perl=TRUE)
            #Phenylalanine
c17b<-gsub("TTT", "TTC", c16b, perl=TRUE)
            #Lysine
c18b<-gsub("AAA", "AAG", c17b, perl=TRUE)
#Shuffle 2
#Valine
c1c<-gsub("GTA", "GTG", c41a, perl=TRUE)
c2c<-gsub("GTC", "GTA", c1c, perl=TRUE)
c3c<-gsub("GTT", "GTC", c2c, perl=TRUE)
            #Histidine
c4c<-gsub("CAC", "CAT", c3c, perl=TRUE)
            #Glutamine
c5c<-gsub("CAG", "CAA", c4c, perl=TRUE)
            #Arginine
c6c<-gsub("AGA", "CGG", c5c, perl=TRUE)
c7c<-gsub("AGG", "AGA", c6c, perl=TRUE)
c8c<-gsub("CGT", "AGG", c7c, perl=TRUE)
c9c<-gsub("CGC", "CGT", c8c, perl=TRUE)
c10c<-gsub("CGA", "CGC", c9c, perl=TRUE)
            #Isoleucine
c11c<-gsub("ATC", "ATA", c10c, perl=TRUE)
c12c<-gsub("ATT", "ATC", c11c, perl=TRUE)
            #Alanine
c13c<-gsub("GCT", "GCA", c12c, perl=TRUE)
c14c<-gsub("GCC", "GCT", c13c, perl=TRUE)
c15c<-gsub("GCG", "GCC", c14c, perl=TRUE)
            #Asparagine
c16c<-gsub("AAT", "AAC", c15c, perl=TRUE)
            #Leucine
c17c<-gsub("TTG", "CTT", c16c, perl=TRUE)
```

```
c18c<-gsub("CTA", "TTG", c17c, perl=TRUE)
c19c<-gsub("CTG", "CTA", c18c, perl=TRUE)
c20c<-gsub("CTC", "CTG", c19c, perl=TRUE)
c21c<-gsub("TTA", "CTC", c20c, perl=TRUE)
        #Glycine
c22c<-gsub("GGA", "GGT", c21c, perl=TRUE)
c23c<-gsub("GGG", "GGA", c22c, perl=TRUE)
c24c<-gsub("GGC", "GGG", c23c, perl=TRUE)
        #Tyrosine
c25c<-gsub("TAT", "TAC", c24c, perl=TRUE)
        #Cysteine
c26c<-gsub("TGC", "TGT", c25c, perl=TRUE)
        #Serine
c27c<-gsub("AGC", "TCG", c26c, perl=TRUE)
c28c<-gsub("AGT", "AGC", c27c, perl=TRUE)
c29c<-gsub("TCC", "AGT", c28c, perl=TRUE)
c30c<-gsub("TCT", "TCC", c29c, perl=TRUE)
c31c<-gsub("TCA", "TCT", c30c, perl=TRUE)
        #Threonine
c32c<-gsub("ACT", "ACA", c31c, perl=TRUE)
c33c<-gsub("ACC", "ACT", c32c, perl=TRUE)
c34c<-gsub("ACG", "ACC", c33c, perl=TRUE)
        #Proline
c35c<-gsub("CCT", "CCA", c34c, perl=TRUE)
c36c<-gsub("CCC", "CCT", c35c, perl=TRUE)
c37c<-gsub("CCG", "CCC", c36c, perl=TRUE)
        #Aspartate
c38c<-gsub("GAT", "GAC", c37c, perl=TRUE)
        #Glutamate
c39c<-gsub("GAA", "GAG", c38c, perl=TRUE)
        #Phenylalanine
c40c<-gsub("TTC", "TTT", c39c, perl=TRUE)
        #Lysine
c41c<-gsub("AAG", "AAA", c40c, perl=TRUE)

#Switch 2
        #Valine
c0d<-gsub("GTA", "GTC", c41c, perl=TRUE)
c1d<-gsub("GTG", "GTT", c0d, perl=TRUE)
        #Histidine
c2d<-gsub("CAT", "CAC", c1d, perl=TRUE)
        #Glutamine
c3d<-gsub("CAA", "CAG", c2d, perl=TRUE)
        #Arginine
c4d<-gsub("CGG", "CGA", c3d, perl=TRUE)
        #Isoleucine
c5d<-gsub("ATA", "ATT", c4d, perl=TRUE)
        #Alanine
c6d<-gsub("GCA", "GCG", c5d, perl=TRUE)
        #Asparagine
c7d<-gsub("AAC", "AAT", c6d, perl=TRUE)
        #Leucine
c8d<-gsub("CTT", "TTA", c7d, perl=TRUE)
        #Glycine
c9d<-gsub("GGT", "GGC", c8d, perl=TRUE)
        #Tyrosine
c10d<-gsub("TAC", "TAT", c9d, perl=TRUE)
        #Cysteine
c11d<-gsub("TGT", "TGC", c10d, perl=TRUE)
        #Serine
c12d<-gsub("TCG", "TCA", c11d, perl=TRUE)
        #Threonine
c13d<-gsub("ACA", "ACG", c12d, perl=TRUE)
        #Proline
c14d<-gsub("CCA", "CCG", c13d, perl=TRUE)
        #Aspartate
c15d<-gsub("GAC", "GAT", c14d, perl=TRUE)
```

```
            #Glutamate
c16d<-gsub("GAG", "GAA", c15d, perl=TRUE)
            #Phenylalanine
c17d<-gsub("TTT", "TTC", c16d, perl=TRUE)
            #Lysine
c18d<-gsub("AAA", "AAG", c17d, perl=TRUE)


Code1<-c41a
Code2<-c18b
Code3<-c41c
Code4<-c18d

Code1
Code2
Code3
Code4
```

BIBLIOGRAPHY

Acehan, D., Jiang, X., Morgan, D.G., Heuser, J.E., Wang, X., and Akey, C.W. (2002). Three-dimensional structure of the apoptosome: implications for assembly, procaspase-9 binding, and activation. Mol. Cell *9*, 423–432.

Antony, A.N., Paillard, M., Moffat, C., Juskeviciute, E., Correnti, J., Bolon, B., Rubin, E., Csordás, G., Seifert, E.L., Hoek, J.B., et al. (2016). MICU1 regulation of mitochondrial Ca(2+) uptake dictates survival and tissue regeneration. Nat. Commun. *7*, 10955.

Austin, S., Tavakoli, M., Pfeiffer, C., Seifert, J., Mattarei, A., De Stefani, D., Zoratti, M., and Nowikovsky, K. (2017). LETM1-mediated K+ and Na+ homeostasis regulates mitochondrial Ca2+ efflux. Front. Physiol. *8*, 839.

Baradaran, R., Wang, C., Siliciano, A.F., and Long, S.B. (2018). Cryo-EM structures of fungal and metazoan mitochondrial calcium uniporters. Nature *559*, 580–584.

Basso, E., Fante, L., Fowlkes, J., Petronilli, V., Forte, M.A., and Bernardi, P. (2005). Properties of the permeability transition pore in mitochondria devoid of Cyclophilin D. J. Biol. Chem. *280*, 18558–18561.

Baughman, J.M., Perocchi, F., Girgis, H.S., Plovanich, M., Belcher-Timme, C.A., Sancak, Y., Bao, X.R., Strittmatter, L., Goldberger, O., Bogorad, R.L., et al. (2011). Integrative genomics identifies MCU as an essential component of the mitochondrial calcium uniporter. Nature *476*, 341–345.

Bhosale, G., Sharpe, J.A., Sundier, S.Y., and Duchen, M.R. (2015). Calcium signaling as a mediator of cell energy demand and a trigger to cell death. Ann. N. Y. Acad. Sci. *1350*, 107–116.

Bhosale, G., Sharpe, J.A., Koh, A., Kouli, A., Szabadkai, G., and Duchen, M.R. (2017). Pathological consequences of MICU1 mutations on mitochondrial calcium signalling and bioenergetics. Biochim. Biophys. Acta. Mol. Cell Res. *1864*, 1009–1017.

Bondarenko, A.I., Jean-Quartier, C., Malli, R., and Graier, W.F. (2013). Characterization of distinct single-channel properties of Ca^{2+} inward currents in mitochondria. Pflugers Arch. *465*, 997–1010.

Bondarenko, A.I., Jean-Quartier, C., Parichatikanond, W., Alam, M.R., Waldeck-Weiermair, M., Malli, R., and Graier, W.F. (2014). Mitochondrial Ca(2+) uniporter (MCU)-dependent and MCU-independent Ca(2+) channels coexist in the inner mitochondrial membrane. Pflugers Arch. *466*, 1411–1420.

Boyman, L., Williams, G.S.B., Khananshvili, D., Sekler, I., and Lederer, W.J. (2013). NCLX: the mitochondrial sodium calcium exchanger. J. Mol. Cell. Cardiol. *59*, 205–213.

Brierley, J.B. (1976). Cerebral hypoxia. In Greenfiled's Neuropathology, F.H. McDowell, and R.W. Brennan, eds. (London: Edward Arnold), pp. 43–85.

Brierley, G.P., Baysal, K., and Jung, D.W. (1994). Cation transport systems in mitochondria: Na+ and K+ uniports and exchangers. J. Bioenerg. Biomembr. *26*, 519–526.

Cain, K., Bratton, S.B., and Cohen, G.M. (2002). The Apaf-1 apoptosome: a large caspase-activating complex. Biochimie *84*, 203–214.

Chance, B. (1965). The energy-linked reaction of calcium with mitochondria. J. Biol. Chem. *240*,

2729–2748.

Cox, D.A., Conforti, L., Sperelakis, N., and Matlib, M.A. (1993). Selectivity of inhibition of Na(+)-Ca2+ exchange of heart mitochondria by benzothiazepine CGP-37157. J. Cardiovasc. Pharmacol. *21*, 595–599.

Crompton, M., and Heid, I. (1978). The cycling of calcium, sodium, and protons across the inner membrane of cardiac mitochondria. Eur. J. Biochem. *91*, 599–608.

Crompton, M., Hediger, M., and Carafoli, E. (1978). The effect of inorganic phosphate on calcium influx into rat heart mitochondria. Biochem. Biophys. Res. Commun. *80*, 540–546.

Csordás, G., Golenár, T., Seifert, E.L., Kamer, K.J., Sancak, Y., Perocchi, F., Moffat, C., Weaver, D., de la Fuente Perez, S., Bogorad, R., et al. (2013). MICU1 controls both the threshold and cooperative activation of the mitochondrial Ca^{2+} uniporter. Cell Metab. *17*, 976–987.

D'Arcy, M.S. (2019). Cell death: a review of the major forms of apoptosis, necrosis and autophagy. Cell Biol. Int. *43*, 582–592.

DeLuca, H.F., and Engstrom, G.W. (1961). Calcium uptake by rat kidney mitochondria. Proc. Natl. Acad. Sci. U. S. A. *47*, 1744–1750.

Denton, R.M. (2009). Regulation of mitochondrial dehydrogenases by calcium ions. Biochim. Biophys. Acta *1787*, 1309–1316.

Dimmer, K.S., Navoni, F., Casarin, A., Trevisson, E., Endele, S., Winterpacht, A., Salviati, L., and Scorrano, L. (2008). LETM1, deleted in Wolf-Hirschhorn syndrome is required for normal mitochondrial morphology and cellular viability. Hum. Mol. Genet. *17*, 201–214.

Dong, Z., Shanmughapriya, S., Tomar, D., Siddiqui, N., Lynch, S., Nemani, N., Breves, S.L., Zhang, X., Tripathi, A., Palaniappan, P., et al. (2017). Mitochondrial Ca2+ uniporter is a mitochondrial luminal redox sensor that augments MCU channel activity. Mol. Cell *65*, 1014-1028.e7.

Doonan, P.J., Chandramoorthy, H.C., Hoffman, N.E., Zhang, X., Cárdenas, C., Shanmughapriya, S., Rajan, S., Vallem, S., Chen, X., Foskett, J.K., et al. (2014). LETM1-dependent mitochondrial Ca2+ flux modulates cellular bioenergetics and proliferation. FASEB J. *28*, 4936–4949.

Fan, C., Fan, M., Orlando, B.J., Fastman, N.M., Zhang, J., Xu, Y., Chambers, M.G., Xu, X., Perry, K., Liao, M., et al. (2018). X-ray and cryo-EM structures of the mitochondrial calcium uniporter. Nature *559*, 575–579.

Fieni, F., Lee, S.B., Jan, Y.N., and Kirichok, Y. (2012). Activity of the mitochondrial calcium uniporter varies greatly between tissues. Nat. Commun. *3*, 1317.

Galluzzi, L., Baehrecke, E.H., Ballabio, A., Boya, P., Bravo-San Pedro, J.M., Cecconi, F., Choi, A.M., Chu, C.T., Codogno, P., Colombo, M.I., et al. (2017). Molecular definitions of autophagy and related processes. EMBO J. *36*, 1811–1836.

Gonzalez-Perez, V., Ben Johny, M., Xia, X.-M., and Lingle, C.J. (2018). Regulatory γ1 subunits defy symmetry in functional modulation of BK channels. Proc. Natl. Acad. Sci. U. S. A. *115*, 9923–9928.

Gottschalk, B., Klec, C., Leitinger, G., Bernhart, E., Rost, R., Bischof, H., Madreiter-Sokolowski, C.T., Radulović, S., Eroglu, E., Sattler, W., et al. (2019). MICU1 controls cristae junction and spatially anchors mitochondrial Ca2+ uniporter complex. Nat. Commun. *10*, 3732.

Gunter, K.K., and Gunter, T.E. (1994). Transport of calcium by mitochondria. J. Bioenerg. Biomembr. *26*, 471–485.

Hajnóczky, G., Csordás, G., Das, S., Garcia-Perez, C., Saotome, M., Sinha Roy, S., and Yi, M. (2009). Mitochondrial calcium signalling and cell death: approaches for assessing the role of mitochondrial Ca2+ uptake in apoptosis. Cell Calcium *40*, 553–560.

Han, G., Casson, R.J., Chidlow, G., and Wood, J.P.M. (2014). The mitochondrial complex I inhibitor rotenone induces endoplasmic reticulum stress and activation of GSK-3β in cultured rat retinal cells. Invest. Ophthalmol. Vis. Sci. *55*, 5616–5628.

Hoffman, N.E., Chandramoorthy, H.C., Shamugapriya, S., Zhang, X., Rajan, S., Mallilankaraman, K., Gandhirajan, R.K., Vagnozzi, R.J., Ferrer, L.M., Sreekrishnanilayam, K., et al. (2013). MICU1 motifs define mitochondrial calcium uniporter binding and activity. Cell Rep. *5*, 1576–1588.

Hoffman, N.E., Chandramoorthy, H.C., Shanmughapriya, S., Zhang, X.Q., Vallem, S., Doonan, P.J., Malliankaraman, K., Guo, S., Rajan, S., Elrod, J.W., et al. (2014). SLC25A23 augments mitochondrial Ca^{2+} uptake, interacts with MCU, and induces oxidative stress-mediated cell death. Mol. Biol. Cell *25*, 936–947.

Holmström, K.M., Pan, X., Liu, J.C., Menazza, S., Liu, J., Nguyen, T.T., Pan, H., Parks, R.J., Anderson, S., Noguchi, A., et al. (2015). Assessment of cardiac function in mice lacking the mitochondrial calcium uniporter. J. Mol. Cell. Cardiol. *85*, 178–182.

Jiang, D., Zhao, L., and Clapham, D.E. (2009). Genome-wide RNAi screen identifies Letm1 as a mitochondrial Ca2+/H+ antiporter. Science *326*, 144–147.

Jonckheere, A.I., Smeitink, J.A.M., and Rodenburg, R.J.T. (2012). Mitochondrial ATP synthase: architecture, function and pathology. J. Inherit. Metab. Dis. *35*, 211–225.

Kamer, K.J., and Mootha, V.K. (2014). MICU1 and MICU2 play nonredundant roles in the regulation of the mitochondrial calcium uniporter. EMBO Rep. *15*, 299–307.

Kamer, K.J., Grabarek, Z., and Mootha, V.K. (2017). High-affinity cooperative Ca2+ binding by MICU1-MICU2 serves as an on-off switch for the uniporter. EMBO Rep. *18*, 1397–1411.

Kamer, K.J., Jiang, W., Kaushik, V.K., Mootha, V.K., and Grabarek, Z. (2019). Crystal structure of MICU2 and comparison with MICU1 reveal insights into the uniporter gating mechanism. Proc. Natl. Acad. Sci. U. S. A. *116*, 3546–3555.

Kirichok, Y., Krapivinsky, G., and Clapham, D.E. (2004). The mitochondrial calcium uniporter is a highly selective ion channel. Nature *427*, 360–364.

Kolobova, E., Tuganova, A., Boulatnikov, I., and Popov, K.M. (2001). Regulation of pyruvate dehydrogenase activity through phosphorylation at multiple sites. Biochem. J. *358*, 69–77.

König, T., Tröder, S.E., Bakka, K., Korwitz, A., Richter-Dennerlein, R., Lampe, P.A., Patron, M., Mühlmeister, M., Guerrero-Castillo, S., Brandt, U., et al. (2016). The m-AAA protease associated with neurodegeneration limits MCU activity in mitochondria. Mol. Cell *64*, 148–162.

Kovács-Bogdán, E., Sancak, Y., Kamer, K.J., Plovanich, M., Jambhekar, A., Huber, R.J., Myre, M.A., Blower, M.D., and Mootha, V.K. (2014). Reconstitution of the mitochondrial calcium uniporter in yeast. Proc. Natl. Acad. Sci. U. S. A. *111*, 8985–8990.

Kwong, J.Q., Lu, X., Correll, R.N., Schwanekamp, J.A., Vagnozzi, R.J., Sargent, M.A., York, A.J., Zhang, J., Bers, D.M., and Molkentin, J.D. (2015). The mitochondrial calcium uniporter selectively

matches metabolic output to acute contractile stress in the heart. Cell Rep. *12*, 15–22.

Lazarou, M., Sliter, D.A., Kane, L.A., Sarraf, S.A., Wang, C., Burman, J.L., Sideris, D.P., Fogel, A.I., and Youle, R.J. (2015). The ubiquitin kinase PINK1 recruits autophagy receptors to induce mitophagy. Nature *524*, 309–314.

Lee, S.K., Shanmughapriya, S., Mok, M.C.Y., Dong, Z., Tomar, D., Carvalho, E., Rajan, S., Junop, M.S., Madesh, M., and Stathopulos, P.B. (2016). Structural insights into mitochondrial calcium uniporter regulation by divalent cations. Cell Chem. Biol. *23*, 1157–1169.

Lemasters, J.J. (2014). Variants of mitochondrial autophagy: Types 1 and 2 mitophagy and micromitophagy (Type 3). Redox Biol. *2*, 749–754.

Lewis-Smith, D., Kamer, K.J., Griffin, H., Childs, A.-M., Pysden, K., Titov, D., Duff, J., Pyle, A., Taylor, R.W., Yu-Wai-Man, P., et al. (2016). Homozygous deletion in MICU1 presenting with fatigue and lethargy in childhood. Neurol. Genet. *2*, e59.

Li, W., and Ye, Y. (2008). Polyubiquitin chains: functions, structures, and mechanisms. Cell. Mol. Life Sci. *65*, 2397–2406.

Li, D., Wu, W., Pei, H., Wei, Q., Yang, Q., Zheng, J., and Jia, Z. (2016). Expression and preliminary characterization of human MICU2. Biol. Open *5*, 962–969.

Liu, J.C., Liu, J., Holmström, K.M., Menazza, S., Parks, R.J., Fergusson, M.M., Yu, Z.-X., Springer, D.A., Halsey, C., Liu, C., et al. (2016). MICU1 serves as a molecular gatekeeper to prevent in vivo mitochondrial calcium overload. Cell Rep. *16*, 1561–1573.

Logan, C. V, Szabadkai, G., Sharpe, J.A., Parry, D.A., Torelli, S., Childs, A.-M., Kriek, M., Phadke, R., Johnson, C.A., Roberts, N.Y., et al. (2013). Loss-of-function mutations in MICU1 cause a brain and muscle disorder linked to primary alterations in mitochondrial calcium signaling. Nat. Genet. *46*, 188–193.

Luongo, T.S., Lambert, J.P., Yuan, A., Zhang, X., Gross, P., Song, J., Shanmughapriya, S., Gao, E., Jain, M., Houser, S.R., et al. (2015). The mitochondrial calcium uniporter matches energetic supply with cardiac workload during stress and modulates permeability transition. Cell Rep. *12*, 23–34.

Luongo, T.S., Lambert, J.P., Gross, P., Nwokedi, M., Lombardi, A.A., Shanmughapriya, S., Carpenter, A.C., Kolmetzky, D., Gao, E., van Berlo, J.H., et al. (2017). The mitochondrial Na+/Ca2+ exchanger is essential for Ca2+ homeostasis and viability. Nature *545*, 93–97.

MacKinnon, R., Aldrich, R.W., and Lee, a W. (1993). Functional stoichiometry of Shaker potassium channel inactivation. Science *262*, 757–759.

Mallilankaraman, K., Cárdenas, C., Doonan, P.J., Chandramoorthy, H.C., Irrinki, K.M., Golenár, T., Csordás, G., Madireddi, P., Yang, J., Müller, M., et al. (2012a). MCUR1 is an essential component of mitochondrial Ca2+ uptake that regulates cellular metabolism. Nat. Cell Biol. *14*, 1336–1343.

Mallilankaraman, K., Doonan, P., Cárdenas, C., Chandramoorthy, H.C., Müller, M., Miller, R., Hoffman, N.E., Gandhirajan, R.K., Molgó, J., Birnbaum, M.J., et al. (2012b). MICU1 is an essential gatekeeper for MCU-mediated mitochondrial Ca(2+) uptake that regulates cell survival. Cell *151*, 630–644.

Marchi, S., Corricelli, M., Branchini, A., Vitto, V.A.M., Missiroli, S., Morciano, G., Perrone, M., Ferrarese, M., Giorgi, C., Pinotti, M., et al. (2019). Akt-mediated phosphorylation of MICU1

regulates mitochondrial Ca2+ levels and tumor growth. EMBO J. *38*, 1–20.

De Marchi, U., Santo-Domingo, J., Castelbou, C., Sekler, I., Wiederkehr, A., and Demaurex, N. (2014). NCLX protein, but not LETM1, mediates mitochondrial Ca2+ extrusion, thereby limiting Ca2+-induced NAD(P)H production and modulating matrix redox state. J. Biol. Chem. *289*, 20377–20385.

Matesanz-Isabel, J., Arias-del-Val, J., Alvarez-Illera, P., Fonteriz, R.I., Montero, M., and Alvarez, J. (2016). Functional roles of MICU1 and MICU2 in mitochondrial Ca(2+) uptake. Biochim. Biophys. Acta *1858*, 1110–1117.

Matsuda, N., Sato, S., Shiba, K., Okatsu, K., Saisho, K., Gautier, C.A., Sou, Y.-S., Saiki, S., Kawajiri, S., Sato, F., et al. (2010). PINK1 stabilized by mitochondrial depolarization recruits Parkin to damaged mitochondria and activates latent Parkin for mitophagy. J. Cell Biol. *189*, 211–221.

Miyazaki, E., Sakaguchi, M., Wakabayashi, S., Shigekawa, M., and Mihara, K. (2001). NHE6 protein possesses a signal peptide destined for endoplasmic reticulum membrane and localizes in secretory organelles of the cell. J. Biol. Chem. *276*, 49221–49227.

Moore, A.S., and Holzbaur, E.L.F. (2016). Dynamic recruitment and activation of ALS-associated TBK1 with its target optineurin are required for efficient mitophagy. Proc. Natl. Acad. Sci. U. S. A. *113*, E3349-58.

Murphy, E., Pan, X., Nguyen, T., Liu, J., Holmström, K.M., and Finkel, T. (2014). Unresolved questions from the analysis of mice lacking MCU expression. Biochem. Biophys. Res. Commun. *449*, 384–385.

Nguyen, N.X., Armache, J.-P., Lee, C., Yang, Y., Zeng, W., Mootha, V.K., Cheng, Y., Bai, X.-C., and Jiang, Y. (2018). Cryo-EM structure of a fungal mitochondrial calcium uniporter. Nature *559*, 570–574.

Nguyen, T.N., Padman, B.S., and Lazarou, M. (2016). Deciphering the molecular signals of PINK1/Parkin mitophagy. Trends Cell Biol. *26*, 733–744.

Nichols, M., Elustondo, P.A., Warford, J., Thirumaran, A., Pavlov, E. V, and Robertson, G.S. (2017). Global ablation of the mitochondrial calcium uniporter increases glycolysis in cortical neurons subjected to energetic stressors. J. Cereb. Blood Flow Metab. *37*, 3027–3041.

Nowikovsky, K., Froschauer, E.M., Zsurka, G., Samaj, J., Reipert, S., Kolisek, M., Wiesenberger, G., and Schweyen, R.J. (2004). The LETM1/YOL027 gene family encodes a factor of the mitochondrial K+ homeostasis with a potential role in the Wolf-Hirschhorn syndrome. J. Biol. Chem. *279*, 30307–30315.

Numata, M., Petrecca, K., Lake, N., and Orlowski, J. (1998). Identification of a mitochondrial Na+/H+ exchanger. J. Biol. Chem. *273*, 6951–6959.

O'Rourke, B. (2007). Mitochondrial ion channels. Annu. Rev. Physiol. *69*, 19–49.

Oxenoid, K., Dong, Y., Cao, C., Cui, T., Sancak, Y., Markhard, A.L., Grabarek, Z., Kong, L., Liu, Z., Ouyang, B., et al. (2016). Architecture of the mitochondrial calcium uniporter. Nature *533*, 269–273.

Pagès, H., Aboyoun, P., Gentleman, R., and DebRoy, S. (2017). Biostrings: Efficient manipulation of biological strings.

Paillard, M., Csordás, G., Szanda, G., Golenár, T., Debattisti, V., Bartok, A., Wang, N., Moffat, C., Seifert, E.L., Spät, A., et al. (2017). Tissue-specific mitochondrial decoding of cytoplasmic Ca2+ signals is controlled by the stoichiometry of MICU1/2 and MCU. Cell Rep. *18*, 2291–2300.

Paillard, M., Csordás, G., Huang, K.-T., Várnai, P., Joseph, S.K., and Hajnóczky, G. (2018). MICU1 interacts with the D-Ring of the MCU pore to control its Ca2+ flux and sensitivity to Ru360. Mol. Cell *72*, 778-785.e3.

Palty, R., Silverman, W.F., Hershfinkel, M., Caporale, T., Sensi, S.L., Parnis, J., Nolte, C., Fishman, D., Shoshan-Barmatz, V., Herrmann, S., et al. (2010). NCLX is an essential component of mitochondrial Na+/Ca2+ exchange. Proc. Natl. Acad. Sci. U. S. A. *107*, 436–441.

Pan, X., Liu, J., Nguyen, T., Liu, C., Sun, J., Teng, Y., Fergusson, M.M., Rovira, I.I., Allen, M., Springer, D.A., et al. (2013). The physiological role of mitochondrial calcium revealed by mice lacking the mitochondrial calcium uniporter. Nat. Cell Biol. *15*, 1464–1472.

Passmore, J.B., Pinho, S., Gomez-Lazaro, M., and Schrader, M. (2017). The respiratory chain inhibitor rotenone affects peroxisomal dynamics via its microtubule-destabilising activity. Histochem. Cell Biol. *148*, 331–341.

Patron, M., Checchetto, V., Raffaello, A., Teardo, E., Vecellio Reane, D., Mantoan, M., Granatiero, V., Szabò, I., De Stefani, D., and Rizzuto, R. (2014). MICU1 and MICU2 finely tune the mitochondrial Ca2+ uniporter by exerting opposite effects on MCU activity. Mol. Cell *53*, 726–737.

Patron, M., Granatiero, V., Espino, J., Rizzuto, R., and De Stefani, D. (2019). MICU3 is a tissue-specific enhancer of mitochondrial calcium uptake. Cell Death Differ. *26*, 179–195.

Paupe, V., Prudent, J., Dassa, E.P., Rendon, O.Z., and Shoubridge, E.A. (2015). CCDC90A (MCUR1) is a cytochrome c oxidase assembly factor and not a regulator of the mitochondrial calcium uniporter. Cell Metab. *21*, 109–116.

Payne, R., Hoff, H., Roskowski, A., and Foskett, J.K. (2017). MICU2 restricts spatial crosstalk between InsP3R and MCU Channels by regulating threshold and gain of MICU1-mediated inhibition and activation of MCU. Cell Rep. *21*, 3141–3154.

Perocchi, F., Gohil, V.M., Girgis, H.S., Bao, X.R., McCombs, J.E., Palmer, A.E., and Mootha, V.K. (2010). MICU1 encodes a mitochondrial EF hand protein required for Ca(2+) uptake. Nature *467*, 291–296.

Petrungaro, C., Zimmermann, K.M., Küttner, V., Fischer, M., Dengjel, J., Bogeski, I., and Riemer, J. (2015). The Ca(2+)-dependent release of the Mia40-induced MICU1-MICU2 dimer from MCU regulates mitochondrial Ca(2+) uptake. Cell Metab. *22*, 721–733.

Phillips, C.B., Tsai, C.-W., and Tsai, M.-F. (2019). The conserved aspartate ring of MCU mediates MICU1 binding and regulation in the mitochondrial calcium uniporter complex. Elife *8*.

Plovanich, M., Bogorad, R.L., Sancak, Y., Kamer, K.J., Strittmatter, L., Li, A.A., Girgis, H.S., Kuchimanchi, S., De Groot, J., Speciner, L., et al. (2013). MICU2, a paralog of MICU1, resides within the mitochondrial uniporter complex to regulate calcium handling. PLoS One *8*, e55785.

Raffaello, A., De Stefani, D., Sabbadin, D., Teardo, E., Merli, G., Picard, A., Checchetto, V., Moro, S., Szabò, I., and Rizzuto, R. (2013). The mitochondrial calcium uniporter is a multimer that can include a dominant-negative pore-forming subunit. EMBO J. *32*, 2362–2376.

Rizzuto, R., Simpson, A.W., Brini, M., and Pozzan, T. (1992). Rapid changes of mitochondrial

Ca2+ revealed by specifically targeted recombinant aequorin. Nature *358*, 325–327.

Ruiz, A., Alberdi, E., and Matute, C. (2014). CGP37157, an inhibitor of the mitochondrial Na+/Ca2+ exchanger, protects neurons from excitotoxicity by blocking voltage-gated Ca2+ channels. Cell Death Dis. *5*, e1156.

Ryu, S.-Y., Beutner, G., Dirksen, R.T., Kinnally, K.W., and Sheu, S.-S. (2010). Mitochondrial ryanodine receptors and other mitochondrial Ca2+ permeable channels. FEBS Lett. *584*, 1948–1955.

Samanta, K., Mirams, G.R., and Parekh, A.B. (2018). Sequential forward and reverse transport of the Na+ Ca2+ exchanger generates Ca2+ oscillations within mitochondria. Nat. Commun. *9*, 156.

Sancak, Y., Markhard, A.L., Kitami, T., Kovács-Bogdán, E., Kamer, K.J., Udeshi, N.D., Carr, S.A., Chaudhuri, D., Clapham, D.E., Li, A.A., et al. (2013). EMRE is an essential component of the mitochondrial calcium uniporter complex. Science *342*, 1379–1382.

Scorrano, L., Penzo, D., Petronilli, V., Pagano, F., and Bernardi, P. (2001). Arachidonic acid causes cell death through the mitochondrial permeability transition. Implications for tumor necrosis factor-alpha aopototic signaling. J. Biol. Chem. *276*, 12035–12040.

Shamseldin, H.E., Alasmari, A., Salih, M.A., Samman, M.M., Mian, S.A., Alshidi, T., Ibrahim, N., Hashem, M., Faqeih, E., Al-Mohanna, F., et al. (2017). A null mutation in MICU2 causes abnormal mitochondrial calcium homeostasis and a severe neurodevelopmental disorder. Brain *140*, 2806–2813.

Sparagna, G.C., Gunter, K.K., Sheu, S.S., and Gunter, T.E. (1995). Mitochondrial calcium uptake from physiological-type pulses of calcium. A description of the rapid uptake mode. J. Biol. Chem. *270*, 27510–27515.

Starkov, A.A., Chinopoulos, C., and Fiskum, G. (2004). Mitochondrial calcium and oxidative stress as mediators of ischemic brain injury. Cell Calcium *36*, 257–264.

De Stefani, D., Raffaello, A., Teardo, E., Szabò, I., and Rizzuto, R. (2011). A forty-kilodalton protein of the inner membrane is the mitochondrial calcium uniporter. Nature *476*, 336–340.

Streb, H., Irvine, R.F., Berridge, M.J., and Schulz, I. (1983). Release of Ca2+ from a nonmitochondrial intracellular store in pancreatic acinar cells by inositol-1,4,5-trisphosphate. Nature *306*, 67–69.

Stueland, C.S., Gorden, K., and LaPorte, D.C. (1988). The isocitrate dehydrogenase phosphorylation cycle. Identification of the primary rate-limiting step. J. Biol. Chem. *263*, 19475–19479.

Tomar, D., Dong, Z., Shanmughapriya, S., Koch, D.A., Thomas, T., Hoffman, N.E., Timbalia, S.A., Goldman, S.J., Breves, S.L., Corbally, D.P., et al. (2016). MCUR1 is a scaffold factor for the MCU complex function and promotes mitochondrial bioenergetics. Cell Rep. *15*, 1673–1685.

Tsai, C.-W., Wu, Y., Pao, P.-C., Phillips, C.B., Williams, C., Miller, C., Ranaghan, M., and Tsai, M.-F. (2017). Proteolytic control of the mitochondrial calcium uniporter complex. Proc. Natl. Acad. Sci. U. S. A. *114*, 4388–4393.

Tsai, M.-F., Jiang, D., Zhao, L., Clapham, D., and Miller, C. (2014). Functional reconstitution of the mitochondrial Ca2+/H+ antiporter Letm1. J. Gen. Physiol. *143*, 67–73.

Tsai, M.-F., Phillips, C.B., Ranaghan, M., Tsai, C.-W., Wu, Y., Willliams, C., and Miller, C. (2016).

Dual functions of a small regulatory subunit in the mitochondrial calcium uniporter complex. Elife *5*, 1–17.

Tufi, R., Gleeson, T.P., von Stockum, S., Hewitt, V.L., Lee, J.J., Terriente-Felix, A., Sanchez-Martinez, A., Ziviani, E., and Whitworth, A.J. (2019). Comprehensive genetic characterization of mitochondrial Ca2+ uniporter components reveals their different physiological requirements in vivo. Cell Rep. *27*, 1541-1550.e5.

Vais, H., Foskett, J.K., and Mak, D.O.D. (2010). Unitary Ca2+ current through recombinant type 3 InsP3 receptor channels under physiological ionic conditions. J. Gen. Physiol. *136*, 687–700.

Vais, H., Tanis, J.E., Müller, M., Payne, R., Mallilankaraman, K., and Foskett, J.K. (2015). MCUR1, CCDC90A, is a regulator of the mitochondrial calcium uniporter. Cell Metab. *22*, 533–535.

Vais, H., Mallilankaraman, K., Mak, D.-O.D., Hoff, H., Payne, R., Tanis, J.E., and Foskett, J.K. (2016). EMRE is a matrix Ca(2+) sensor that governs gatekeeping of the mitochondrial Ca(2+) uniporter. Cell Rep. *14*, 403–410.

Vasington, F.D., and Murphy, J. V (1962). Ca ion uptake by rat kidney mitochondria and its dependence on respiration and phosphorylation. J. Biol. Chem. *237*, 2670–2677.

Waldeck-Weiermair, M., Jean-Quartier, C., Rost, R., Khan, M.J., Vishnu, N., Bondarenko, A.I., Imamura, H., Malli, R., and Graier, W.F. (2011). Leucine zipper EF hand-containing transmembrane protein 1 (Letm1) and uncoupling proteins 2 and 3 (UCP2/3) contribute to two distinct mitochondrial Ca2+ uptake pathways. J. Biol. Chem. *286*, 28444–28455.

Wan, B., LaNoue, K.F., Cheung, J.Y., and Scaduto, R.C. (1989). Regulation of citric acid cycle by calcium. J. Biol. Chem. *264*, 13430–13439.

Wang, L., Yang, X., Li, S., Wang, Z., Liu, Y., Feng, J., Zhu, Y., and Shen, Y. (2014). Structural and mechanistic insights into MICU1 regulation of mitochondrial calcium uptake. EMBO J. *33*, 594–604.

Wang, L., Duan, Q., Wang, T., Ahmed, M., Zhang, N., Li, Y., Li, L., and Yao, X. (2015). Mitochondrial respiratory chain inhibitors involved in ROS production induced by acute high concentrations of iodide and the effects of SOD as a protective factor. Oxid. Med. Cell. Longev. *2015*, 217670.

Wang, Y., Nguyen, N.X., She, J., Zeng, W., Yang, Y., Bai, X., and Jiang, Y. (2019). Structural mechanism of EMRE-dependent gating of the human mitochondrial calcium uniporter. Cell *177*, 1252-1261.e13.

Wu, J., Liu, L., Matsuda, T., Zhao, Y., Rebane, A., Drobizhev, M., Chang, Y.-F., Araki, S., Arai, Y., March, K., et al. (2013). Improved orange and red Ca^{2}± indicators and photophysical considerations for optogenetic applications. ACS Chem. Neurosci. *4*, 963–972.

Wu, W., Shen, Q., Lei, Z., Qiu, Z., Li, D., Pei, H., Zheng, J., and Jia, Z. (2019). The crystal structure of MICU2 provides insight into Ca2+ binding and MICU1-MICU2 heterodimer formation. EMBO Rep. *20*, e47488.

Xing, Y., Wang, M., Wang, J., Nie, Z., Wu, G., Yang, X., and Shen, Y. (2019). Dimerization of MICU proteins controls Ca2+ influx through the mitochondrial Ca2+ uniporter. Cell Rep. *26*, 1203-1212.e4.

Yamamoto, T., Yamagoshi, R., Harada, K., Kawano, M., Minami, N., Ido, Y., Kuwahara, K., Fujita,

A., Ozono, M., Watanabe, A., et al. (2016). Analysis of the structure and function of EMRE in a yeast expression system. Biochim. Biophys. Acta *1857*, 831–839.

Yoo, S.-M., and Jung, Y.-K. (2018). A molecular approach to mitophagy and mitochondrial dynamics. Mol. Cells *41*, 18–26.

Yoo, J., Wu, M., Yin, Y., Herzik, M.A., Lander, G.C., and Lee, S.-Y. (2018). Cryo-EM structure of a mitochondrial calcium uniporter. Science *361*, 506–511.

Zhao, H., Li, T., Wang, K., Zhao, F., Chen, J., Xu, G., Zhao, J., Li, T., Chen, L., Li, L., et al. (2019). AMPK-mediated activation of MCU stimulates mitochondrial Ca2+ entry to promote mitotic progression. Nat. Cell Biol. *21*, 476–486.